Intracellular dynamics of superparamagnetic iron oxide nanoparticles for magnetic particle imaging

Eric Teeman

A dissertation
submitted in partial fulfillment of the
requirements for the degree of

Doctor of Philosophy

University of Washington

2019

Reading Committee:

Kannan Krishnan, Chair

Christine Luscombe

Fumio Ohuchi

Lucien Brush

Program Authorized to Offer Degree:
Materials Science & Engineering

University of Washington

Abstract

Intracellular dynamics of superparamagnetic iron oxide nanoparticles for magnetic particle imaging

Eric Teeman

Chair of the Supervisory Committee:
Professor Kannan Krishnan
Materials Science & Engineering

Superparamagnetic iron oxide nanoparticles (SPIONs) are a foundational platform for a variety of biomedical applications. Of particular interest is Magnetic Particle Imaging (MPI), which is a growing area of research and development due to its advantages including high resolution and sensitivity with positive contrast and without ionizing radiation. Significant work has been previously accomplished in the area of in vivo optimization of SPIONs for MPI as well as their biodistribution in and clearance from the body. However, little is known about the dynamics of SPIONs on the sub-cellular level. It is important to understand how the magnetic signal from SPIONs in MPI is affected by internalization within cells as physical and magnetic properties of SPIONs may be subject to changes. Here considerations must be made for the complex and close-packed nature of organelles and cellular material inside of the cell membrane.

This work shows a clear decrease in magnetic performance of SPIONs after internalization and a systematic consideration of applicable factors that affect SPION signal generation, including microstructure, environment, and interparticle interactions. It is observed that microstructure is unchanged after internalization and surrounding environment plays little to no role in magnetic response for the SPIONs studied here. Interparticle interactions described by magnetostatic coupling of SPIONs held in close proximity to one another after

internalization are shown to be the dominant cause of decreased magnetic performance in cells. These conclusions have been drawn from transmission electron microscopy (TEM) image analysis at relevant length scales, experimentally prepared and characterized SPIONs in varied environmental conditions, and theoretical modeling with Monte Carlo simulations. The addition of steric bulk to SPIONs is explored as an approach to recovering magnetic performance after internalization in cells. These results are promising for *in vivo* targeting, diagnostic, and cell tracking applications in MPI.

TABLE OF CONTENTS

LIST OF FIGURES

LIST OF TABLES

GLOSSARY

A_5/A_3: fifth-over-third harmonic ratio - for harmonic amplitudes in MPS

DLS: dynamic light scalltering

DMEM: Dulbeccos modified eagles medium - cell-culturing medium for RAW 264.7 cells

EMEM: Eagle's minimum essential medium - cell-culturing medium for HT-1080 cells

FWHM: full width at half maximum

ICP-OES: inductively couple plasma - optical emission spectrometry

MPI: magnetic particle imaging

MPS: magnetic particle spectrometer

PBS: phosphate buffered saline

PDI: polydispersity index - a distribution parameter of hydrodynamic size

PEG: polyethylene glycol - a hydrophilic and biocompatible polymer

PMAO: poly(maleic anhydride-alt-1-octadecene) - an amphiphilic polymer containing anhydride and octadecene functional groups

PMAO-PEG: an amphiphilic copolymer of PMAO and PEG

PSF: point spread function

SPION: superparamagnetic iron oxide nanoparticle

TEM: transmission electron microscopy

VSM: vibration sample magnetometry

XRD: x-ray diffractometry

ACKNOWLEDGMENTS

I wish to thank my family who have supported me throughout my academic pursuits, especially my parents, Wayne and Lora, sister, Alex, and partner, Kayla. Their constant support and encouragement has been invaluable and I wouldn't be who I am today without them.

I next would like to thank my advisor, Prof. Kannan M. Krishnan, for his guidance throughout this thesis and in my development as a scientist. His dedication to the education of his advisees and the students in his classroom sets a high standard to which I aspire. I also want to thank my current and past committee members, Prof. Christine Luscombe (UW MSE), Prof. Fumio Ohuchi (UW MSE), Prof. Lucien Brush (UW MSE), and Prof. Xiaohu Gao (UW BioE) for their time and insight.

I would further like to thank Dr. James Evans for welcoming me into his research group during my time at Pacific Northwest National Lab and actively teaching me a series of skills crucial to the success of my research. His support and that of his group members, Dr. Chuck Smallwood, Dr. Irina Novikova, and Dr. Trevor Moser, was irreplaceable.

I would also like to thank all those within and involved with the Krishnan Research Group who have helped me in the development and execution of my PhD work. In particular, Carolyn Shasha, Ryan Hufschmid, Dr. Ulrich Engelmann, Dr. Hamed Arami, Dr. Amit Khandhar, Dr. Scott Kemp, Dr. Matt Ferguson, Dr. Asahi Tomitaka, Dr. Olivia Lenz, Mark Brunson, Zandra Rojo, Alyssa Troksa, and Matthew Kouthong.

Lastly, none of this would have been possible without the financial support of the

Achievement Rewards for College Scientists (ARCS) Foundation, Washington Research Foundation (WRF), Department of Energy (DoE), National Institutes of Health (NIH), National Science Foundation (NSF), University of Washington Materials Science & Engineering and Physics Departments.

DEDICATION

To my family.

Chapter 1

INTRODUCTION

In the clinical environment, there is little of more importance than accurate and early detection and treatment of disease. In the United States, there was a decrease in the percentage of deaths attributed to cardiovascular disease of 30.3% in 1999 to 23.4% in 2015. Over this same period, the percentage of deaths attributed to malignant neoplasms, or more commonly referred to as cancerous tumors, only marginally decreased from 23.0% to 22.0% [1, 2]. This highlights the variable difficulty in diagnosing and treating cardiovascular and cancer-related disease. Cancer does not often have straightforward observable markers and may not show symptoms until far too late in the tumor's progression and spread throughout the body. To combat this ongoing struggle, there has been significant research into the early diagnosis and imaging of cancer through the use of novel nanoscale materials that can be tuned to a variety of different functions.

The past several decades have seen significant advances nanomaterials in medical applications through biomedical imaging [3, 4, 5] and treatment [6, 7, 8]. In particular, direct imaging of the body and distressed regions such as tumors drives the diagnosis, treatment, and continued monitoring of disease. Without continued advancement in the quality and rate of acquisition of biomedical imaging techniques, there is going to be an upper limit to what can be observed and how early disease can be caught.

Magnetic Particle Imaging [9] (MPI), a fundamentally novel imaging technique developing over recent years, shows significant promise over many of the imaging techniques currently available such as positron emission tomography, computed tomography, x-ray angiography, and magnetic resonance imaging; each of which is lacking in one key aspect or another.

Despite its short history, the MPI research field has already demonstrated preclinical success in a variety of applications including blood-pool imaging of cardiovasculature [10, 11, 12], color imaging of coated catheters [13, 14], gut-bleed detection [15], real-time perfusion imaging in acute stroke [16], imaging of traumatic brain injury [17], diagnosis of aneurysm [18], cancer detection [19, 20], and stem-cell tracking [21, 22].

MPI is a tracer-based modality that directly images superparamagnetic iron oxide nanoparticles (SPIONs), [23] with signal intensity and resolution critically dependent on their *in vivo* relaxation dynamics. [24] As such, MPI offers high image contrast (with negligible background signal from diamagnetic tissue), a signal linear with tracer concentration [25] and zero depth attenuation, and is safe as it uses no ionizing radiation, as compared with many other biomedical imaging methods. Additionally, a demonstrated high sensitivity (200 nM Fe) [26] and high temporal resolution [27] is achieved when optimized SPIONs of tailored size and size dispersity are used [28, 29].

Overall MPI promises a biomedical imaging modality that combines the speed of X-ray computed tomography (CT), the safety of magnetic resonance imaging (MRI), and the sensitivity of positron-emission tomography (PET). Almost all these recent advances in MPI, especially in the context of clinical translations, are critically dependent on the *in vivo* magnetic relaxation behavior and pharmacokinetics [30] of the SPION tracers. SPIONs flowing in the body have a set clearance rate determined by their colloidal properties, either through common mechanisms in the liver and spleen or through capture by other cells capable of internalizing nanomaterials, including tumors [31].

After internalization in cells, SPIONs encounter conditions different to that of nanoparticles dispersed freely in an aqueous solution such as increased acidity (decreased pH) [32], increased viscosity [33], and decreased interparticle separation. Each of these conditions has the potential to affect the performance of SPIONs by limiting the motion of the physical objects and their internal magnetic moment. Previous studies have illustrated the potential for increased viscosity and magnetostatic interactions to degrade the magnetic performance of SPIONs for magnetic fluid hyperthermia [34, 35, 36] and quantification of SPIONs in

tissue [37, 38]. While these studies are informative for the MPI field, the nanoparticle sizes vary significantly from those optimized for MPI, and a direct comparison is insufficient.

The following sections include a subset of the necessary information to continue through the remainder of this thesis including an introduction to magnetism, background on iron oxide materials, magnetic relaxation dynamics, and further details about MPI and a zero-dimensional variant of magnetic performance utilized here.

1.1 Magnetism

To understand how SPIONs react to the variable environment within a cell, one must first have a foundational knowledge of how magnetism arises and the types of magnetic materials that arise due to this phenomena. This section is a brief introduction to magnetism and the characteristic behavior that defines the superparamagnetic aspect of SPIONs. A significantly more complete description of the content of this section is available from [23].

Magnetic materials can be broadly differentiated by their characteristic response to an applied magnetic field. There are five types of notables responses including diamagnetism, paramagnetism, ferromagnetism, ferrimagnetism, and antiferromagnetism. The typical equilibrium responses and relative magnetizations of each type are illustrated in Fig. 1.1. Diamagnetism occurs when an applied magnetic field induces a net magnetic moment in a material with a direction opposite that of the applied field. Paramagnetism is the result of unpaired electrons freely, but weakly, aligning with an applied magnetic field and generating a net magnetic moment in the same direction of the applied field.

Ferromagnetism is a variation on paramagnetism in which unpaired electrons align with the applied field, but additional magnetization is generated from the spontaneous parallel alignment of magnetic moments throughout the material to reach a lower energy state. This spontaneous alignment results in permanent magnetization that is only removed through increased temperature causing random thermal energy to destabilize the low energy aligned state. To discuss ferrimagnetism and antiferromagnetism, the concept of magnetic domains must first be introduced.

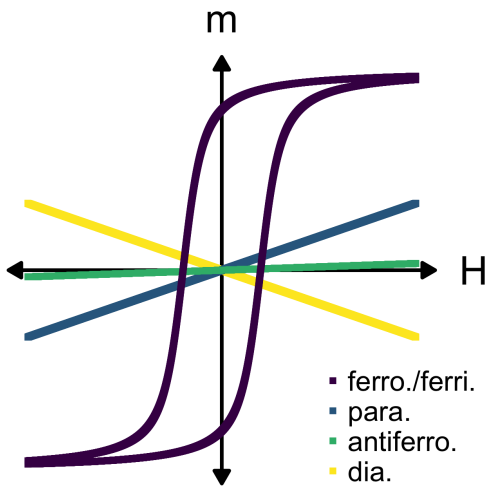

Figure 1.1: Comparison of magnetization behavior for different types of magnetic materials from positive to negative to positive applied field. Ferro- and ferrimagnetic materials show similar behavior where the saturation magnetization, remanence, and coercivity are all material dependent.

Ferromagnetic materials have a net magnetic moment through spontaneous parallel alignment of magnetic moments, but this is a size-dependent process where a large material is not in its lowest energy state if all of its magnetic moments are entirely parallel. Instead, alignment occurs in smaller fractions, or magnetic domains, where the lowest energy state is achieved through magnetic moment alignment within and between each domain. Ferrimagnetism and antiferromagnetism occur when there are two or more sub-lattices within a magnetic material. Antiferromagnetic materials exist with zero net magnetic moment as a result of the antiparallel alignment of adjacent magnetic sub-lattices. Ferrimagnetic materials behave similarly, but exist with a net magnetic moment due to unequal amounts of opposing magnetic moments in different sublattices.

1.1.1 Superparamagnetism and magnetic nanoparticles

As size decreases, the number of magnetic domains within a material decreases until there is only one present. This single domain particle has a magnetic moment that is reversible under

the influence of an applied magnetic field but also retains magnetization at zero applied field. As the size of the particle is further decreased, the influence of random thermal energy begins to affect its lowest energy configuration. In particular, as ferrimagnetic and ferromagnetic materials approach and cross a size-dependent threshold, their magnetic moments become reversible with the thermal energy alone. This is defined as superparamagnetism and is observed as hysteresis without remanent magnetization at zero applied field. In this definition, it is assumed that the measurement time is significantly large ($\sim 100\,\mathrm{s}$). The difference between ferromagnetic and superparamagnetic magnetization is shown in Fig. 1.2.

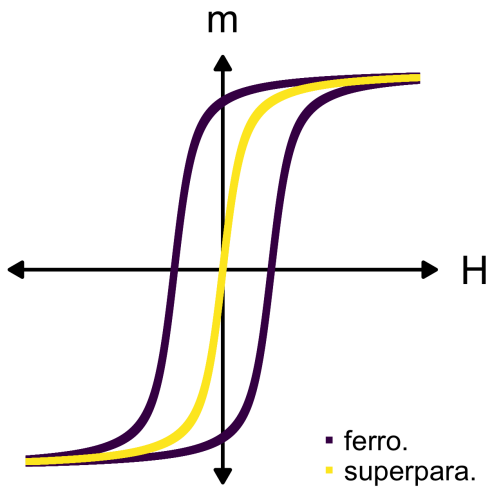

Figure 1.2: Comparison of ferromagnetic and superparamagnetic magnetization.

In addition to being a size-dependent phenomenon, superparamagnetism is also material dependent where the size at which single domains form and superparamagnetism manifests varies. A series of commonly considered magnetic materials, most of which can be synthesized as magnetic nanoparticles, is shown in Fig. 1.3. Here it is observed that there is a significant range of single domain and superparamagnetic size limits for these materials. From this group of materials, a selection is generated from those most viable for biomedical applications. Of particular consideration are those that are biocompatible and retain suitable magnetic properties and sizes for use in various imaging and therapy applications.

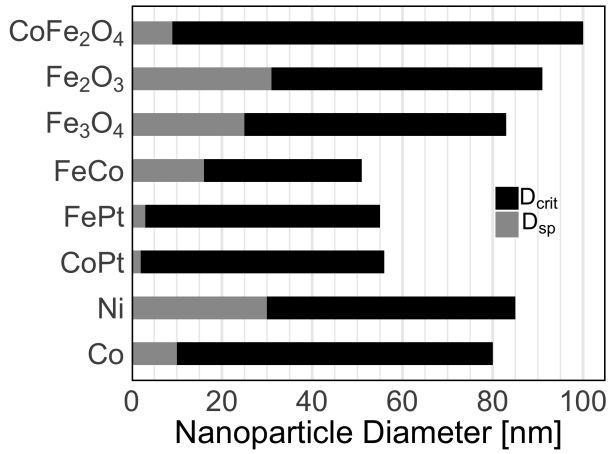

Figure 1.3: Superparamagnetic, D_{sp}, and single domain, D_{crit}, sizes for various metallic and metal-oxide materials when measurement times are $\sim 100\,s$. Adopted from [39].

1.2 Iron oxides

While a wide variety of materials can be made into magnetic nanoparticles, there is only a subset that is suitable for use in biomedical applications. The primary characteristic necessary is biocompatibility including limited toxicity, both acute and chronic, as well as a desired natural biological process for handling the material.

Of the magnetic nanoparticle candidates discussed in the previous section, only iron oxides, or more specifically SPIONs, have historically been chosen for use in many applications as they meet the criteria for biocompatibility and have no remanent magnetization in the absence of an applied field [40, 31]. This is exemplified by previous FDA approval of iron oxide nanoparticles for use in iron deficiency treatment [41]. Additionally, they can serve as a versatile platform to which a wide variety of different coatings [42, 43, 44, 45, 46, 47], targeting ligands [48, 49], and imaging moieties [20] can be applied.

Iron oxides are the class of materials that are considered throughout the remainder of this work, but it is important to denote the specific desired properties and associated relevant crystal phases of iron oxide that must be prepared to achieve those properties.

1.2.1 Phases

Magnetic response in imaging and therapy related applications generally relies on the rate and scale of magnetization reversal in SPIONs suggesting that materials with higher saturation magnetizations would be better suited for these applications. There are four phases of iron oxide that SPIONs can take including wüstite (FeO), maghemite (γ-Fe_2O_3), magnetite (Fe_3O_4), and hematite (α-Fe_2O_3). A list of the iron oxide phases and their properties is shown in Table 1.1. Both wüstite and hematite are antiferromagnetic at room, and biological, temperatures and thus are not useful in many applications including MPI. Maghemite and magnetite, however; are both ferrimagnetic and superparamagnetic under characteristic size limits meaning they have magnetic response curves that can be utilized in MPI.

Table 1.1: Iron oxide crystal phases.[50]

Phase	Chemical Formula	Structure	Lattice Parameters [Å]	Magnetic Classification
Wüstite	$Fe^{2+}O$	Non-stoichiometric NaCl	a: 4.332	Antiferromagnetic
Magnetite	$Fe^{2+}Fe_2^{3+}O_4$	Inverse-spinel	a: 8.397	Ferrimagnetic
Maghemite	γ-$Fe_2^{3+}O_3$	Inverse-spinel	a: 8.33	Ferrimagnetic
Hematite	α-$Fe_2^{3+}O_3$	Corundum	a: 5.038, c: 13.772	Antiferromagnetic

If either magnetite or maghemite can be synthesized reproducibly and uniformly through controllable bottom-up and scalable methods, then a strongly performing therapeutic or imaging tracer is possible. Due to magnetite's higher possible saturation magnetization, it is the more desirable crystal phase of the two options. As tracer performance is crucial to the advancement of MPI as a viable commercial technique, significant work has gone into optimizing the synthesis and oxidation method employed in this work and it has been shown to reproducibly generate magnetite instead of maghemite. [51, 52]

SPIONs prepared to be an appropriate size and crystalline structure for imaging and therapeutics respond in multiple ways to an applied magnetic field that depends on the rate of change and strength of the field as well as the most energetically favorable conditions. The

next section is an introduction to those mechanisms.

1.3 Magnetic relaxation mechanisms

SPIONs are known to rotate with an applied alternating magnetic field defined by Eq. 1.1 with field amplitude, H_0, frequency, f, and exposure time, t.

$$H_{app}(t) = H_0 sin\,(2\pi f t) \tag{1.1}$$

The probability that a particle's magnetic moment aligns with the applied magnetic field depends on an energetic comparison between thermal energy, $k_B T$, and the anisotropy energy, KV_c, a particle with anisotropy constant, K, and volume, V_c. The energetics are incorporated into two mechanisms through which SPIONs dispersed in a solution are able to react to an applied magnetic field dynamically. To describe this phenomenon, we start by defining the easy axis, $\hat{\mathbf{n}}$, and a vector representing the magnetic moment, $\boldsymbol{\mu}$. As the direction of an applied magnetic field is changed, a higher energy state is generated in which the magnetic moment and applied field are not aligned. The magnetic moment of the particle can move to align with the applied field through either Brownian or Néel relaxation.

In the case of Brownian relaxation, the easy axis and magnetic moment vector are aligned initially, and the whole particle rotates to allow the arbitrary axis, magnetic moment, and applied field to be aligned.

$$\tau_B = \frac{3\eta V_h}{k_B T} \tag{1.2}$$

Brownian relaxation depends most heavily on the viscosity, η, of the solution and the hydrodynamic volume, V_h, of the particle. The relationship between these factors and random thermal motion is given by Eq. 1.2 [53].

Under Néel relaxation, however; the magnetic moment rotates within the particle to align

with the applied field without a change in the orientation of the arbitrary axis.

$$\tau_N = \frac{\pi}{2}\tau_0\frac{e^{\sigma}}{\sqrt{\sigma}} \tag{1.3}$$

Here σ is equal to $\frac{KV_c}{k_BT}$ and it is assumed that $\sigma \gg 1$. The factors that have the most apparent contribution to Néel relaxation are the anisotropy constant, K, and the particle core volume, V_c. These factors are again concerning random thermal motion and the relaxation time can be represented by Eq. 1.3 [54].

It is typically assumed that for ultra-small particles ($< 15\,\text{nm}$), Néel relaxation dominates. Conversely, for large particles ($> 30\,\text{nm}$), Brownian relaxation dominates. In reality, the amount of time it takes for a particle to relax is a combination of the Brownian and Néel relaxation. The SPIONs in this work are typically between 20 to 30 nm and the exact contribution of each relaxation mechanism requires sophisticated computational modeling. This work is currently ongoing in the Krishnan Research Group [55] and the magnetic nanoparticle community.

Depending on the state in which the SPIONs are found, each of these relaxation mechanisms contributes more or less to the overall effective relaxation time. One such state is when nanoparticles are trapped in a cellular environment. It is expected that within the cell membrane there is a close-packed grouping of organelles, proteins, enzymes, and a large number of other cell components that result in a two to three-fold increase in viscosity compared to deionized water [33]. Knowing that in MPI the SPION response is dependent on the relaxation time, it is critical to determine if a change occurs in the factors dominating either or both relaxation mechanisms. Also, it is likely that SPIONs that are uptaken into a cell have more than one potential final destination before exocytosis or degradation. If there is a preferential path for the SPIONs to take once inside the cell, that would be an important consideration in determining the source of, if any, change in MPI response.

1.4 Magnetic particle imaging and spectroscopy

MPI is a tracer-dependent technique recently developed and currently under substantial study due to the inherent advantages it can provide to the medical imaging community [9, 10]. Some of these advantages include several orders of magnitude greater signal than water or protons used in other magnetic imaging techniques, quantitative and linear signal as a function of concentration, and positive contrast due to the nature of signal generation. One of the significant limitations of existing medical imaging techniques is their reliance on potentially harmful agents such as ionizing, iodinated, and gadolinium species as are required in positron emission tomography (PET), computed tomography (CT), and MRI, respectively. These agents are used to bring improved imaging through positive-contrast, or the generation of higher intensity areas of an image, contrasting the use of negative-contrast agents, or the diminishment of the base signal of surrounding tissue.

The ease of use and interpretation of positive-contrast imaging warrants its use in many instances even with the consideration that contrast is generated through potentially harmful means. Here, the first advantage of MPI is highlighted considering it does not require the use of harmful contrast agents. Instead, the contrast in MPI is generated through the magnetic response of metallic-oxide nanoparticles. These nanoparticles are most often SPIONs that can be easily conjugated with a variety of different surface coatings and targeting-ligands. Also, there are previous examples of FDA approved SPIONs [41] paving the way for less complicated and expedited future approval of MPI tracers.

Signal generation in MPI is dependent on the non-linear magnetization response of SPIONs to an applied alternating magnetic field. As the applied field changes, a magnetic nanoparticle attempts to align with the field, a process which can be observed through the implementation of a separate detection coil. Depending on the saturation magnetization, field amplitude, frequency, and several other factors, the ability and rate at which the nanoparticle can align with the applied field varies.

MPI serves as the final implementation of this technology, but it is possible to observe

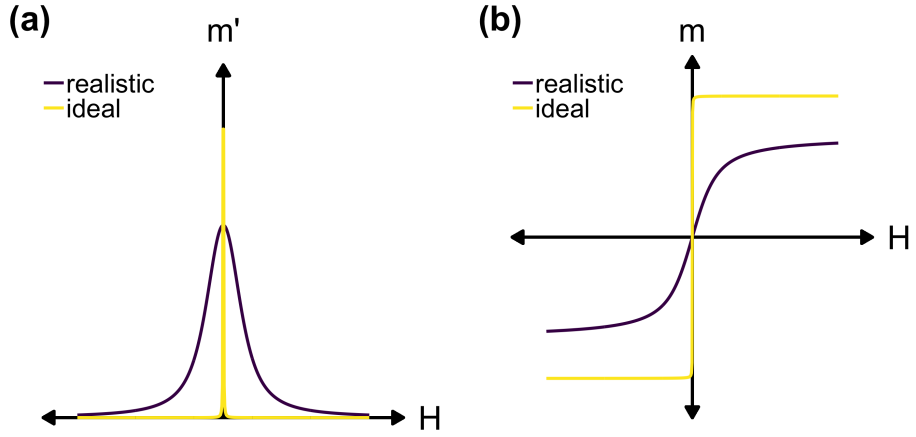

Figure 1.4: Idealized and realistic first derivative of ac magnetization (a) and ac magnetization (b).

the magnetic response of these tracers through other means, including magnetic particle spectroscopy (MPS). In MPS, the observed signal is equivalent to the first derivative of the particle magnetization. A perfect MPS signal would act as a step function where the magnetic moment reverses instantly, but limitations in the fundamental physics of SPION relaxation, the energy required to reverse the magnetic moment, and innate size distributions of real world synthetic SPIONs cause them to reverse at different applied fields. The difference between ideal and realistic MPS signal is illustrated in Fig 1.4.

At the applied field amplitudes and frequencies utilized in MPI and MPS, SPIONs increasing in size larger than approximately 15 nm will begin to show open loop hysteresis rather than superparamagnetic magnetization. This appears in the MPS signal as two peaks instead of one, as shown in Fig. 1.5a, and increasing loop size with increasing core size, as shown in Fig. 1.5b. The peak height and full width at half maximum (FWHM) of this observed MPS signal can be directly related to sensitivity and resolution, respectively, in MPI. Fig. 1.5a illustrates the trend of improving performance in MPS and can be seen through increasing peak height and decreasing FWHM.

Also, the performance can be characterized by taking a Fourier Transform for the magnetization and observing the amplitude and ratios of the harmonics generated. Example

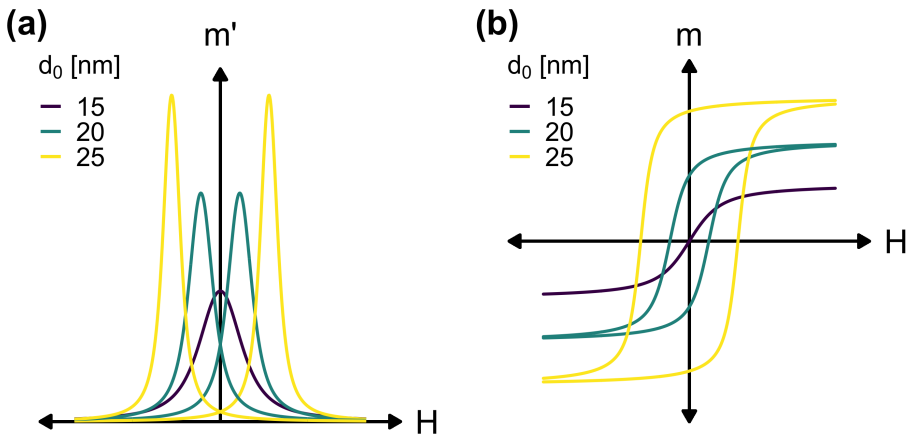

Figure 1.5: Expected shape of the first derivative of ac magnetization (a) and ac magnetization (b) for core sizes increasing from poor to approaching optimal for use for MPI.

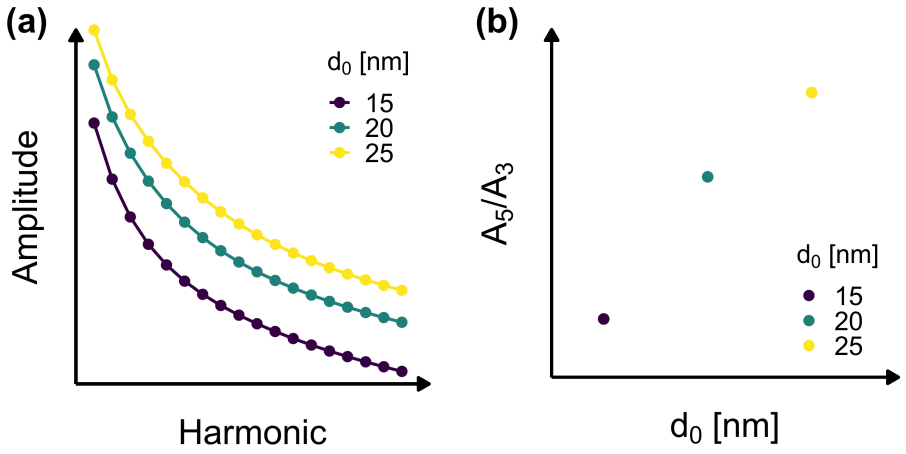

Figure 1.6: Exampl e harmonic spectra (a) and corresponding A_5/A_3 (b) obtained by taking the Fourier transform of the magnetization where increasing intensity and flatter spectra across the harmonics is associated with increasing core size and overall better performance.

harmonics for increasing core sizes are shown in Fig. 1.6a. Here, higher amplitude and slower decrease in amplitude with increasing harmonic number is desired. An idealized MPS signal would be reflected in the harmonic spectra as a flat horizontal line with an equal contribution from all harmonics to the total signal.

A common ratio extracted from the harmonic spectra is the firth-over-third harmonic ratio, A_5/A_3, which increases with the over quality of MPS signal or total performance. This value is mass independent and can thus be used to compare samples without quantification of iron content. A general trend of increasing core size and the corresponding A_5/A_3 is shown in Fig. 1.6b. In experimental data collection, the first harmonic is dominated by the signal from the applied magnetic field rather than from SPIONs. Its amplitude is typically one to two orders of magnitude greater than that of the third harmonic. Due to this factor, the first harmonic is left out of the discussion of magnetic performance.

1.5 Context and thesis scope

The Krishnan Research Group has made a concerted effort in recent years to generate magnetic nanoparticles for biomedical imaging and treatment. This task has been carried out with a systematic approach through multiple researchers. Initially, it was believed that cobalt nanoparticles would be the optimal candidate for these tasks based on their high saturation magnetization, but it was determined that the toxicity of cobalt was unacceptable in biomedical applications [56]. A transition to lower saturation magnetization, but biocompatible iron oxide was made, and relatively small SPIONs were synthesized for magnetic fluid hyperthermia treatment purposes [57]. With the emergence of the MPI field, a parallel optimization of different size ranges was carried out to both generate ideal MPI tracers [58] as well as bifunctional SPIONs that can both satisfy imaging and treatment applications [59]. Later, enhanced phase optimization and experimentally optimized MPI tracers were generated in a commercialization setting and for the good of the MPI field [52].

While optimization of the core is a crucial component of SPIONs for the intended applications, it was not lost on the Krishnan Group that the coating is equally important.

The earliest attempts at coating SPIONs were for colloidal stability and biocompatibility purposes [57]. These coatings worked but were not biocompatible to the standard required in clinical applications of SPIONs. New formulations were optimized for low toxicity and long circulation times *in vivo* [59]. These SPIONs were ideal for cardiovascular applications, but it was necessary to vary the coatings for more specialized targeting capabilities *in vitro* [49] and *in vivo* [60] and in a diagnostic platform [61].

At this stage, multiple questions and applications remain in the magnetic nanoparticle research field. Two of which are foundational to the scope of this thesis include: Is it possible to vary the coatings on SPIONs such that cell loading and tracking applications are possible without a significant loss of previous tracer optimization? Also, once SPIONs reach their final *in vivo* locations and potentially are internalized in cells, what happens to their physical characteristics and magnetic performance as tracers?

With these questions in mind, a general outline of this thesis is presented here: Chapters 2 and 3 address the preparation, coating, and characterization of SPIONs. Chapter 4 includes an introduction to internalization mechanisms and an examination of SPION-cell interactions during and after internalization. Chapter 5 addresses the variable nature of SPION magnetic performance after internalization in cells and how that performance can be controlled.

Chapter 2

SYNTHESIS AND COATING OF SPIONS FOR BIOMEDICAL APPLICATIONS

To utilize SPIONs in any given biomedical application, they must first be synthesized and made dispersible in an aqueous medium. This chapter is an introduction to the methods available for the preparation and coating of SPIONs with the focus being those used in this work.

2.1 Synthesis of SPIONs

In recent years, a variety of synthetic approaches have been developed to produce superparamagnetic iron oxide nanoparticles (SPIONs) with desirable properties for an equally varied number of applications. Each synthetic route produces SPIONs with different sizes, size distributions, shapes, crystal structures, and surface coatings. As a result, there are many options for researchers to choose from when using SPIONs, but the appropriate method must fit the specific application, and often further optimization is required to tailor *in vivo* SPION performance.

SPION synthesis methods are commonly categorized by the solvent employed including aqueous coprecipitation and non-polar solvent based thermolysis, both of which have their advantages and disadvantages. Coprecipitation of iron (II) and iron (III) salts in the presence of alkaline solution, first described by Bee [62] and Kang [63], has shown to be effective at producing primarily ultrasmall (<10 nm) SPIONs, but with relatively limited control of size distribution and phase. More recent studies have shown that variation of the type of salt solution, pH, and other reaction parameters can improve the control of the SPION properties, but still with limited reproducibility from batch to batch.

One of the strongest determining factors of SPION usefulness in applications is its crystal structure and resulting saturation magnetization (M_s). Control of crystal structure through coprecipitation of iron salts is also limited due to the presence of water and dissolved oxygen in solution. This method produces magnetite nanoparticles, though they oxidize to maghemite and hematite without careful control of reaction and storage conditions. The primary concern comes when SPIONs oxidize fully to hematite, which is antiferromagnetic and above 283 K has a weak spontaneous magnetization due to its canted spin moments. Both magnetite and maghemite are viable for most applications but relatively unstable at room temperature.

In coprecipitation syntheses with control of oxidation, colloidal stability in aqueous solution remains a concern. Through the inclusion of surfactants in the coprecipitation synthesis or through additional coating reactions after core synthesis, colloidal stability can be reached. This is often accomplished through the inclusion of sugars or polymeric molecules that can covalently adhere to the SPION surface or form micelle-like structures around the particle.

These reactions can produce SPIONs that have modest performance in MPI such as the most commonly used tracer Resovist©. Resovist©, however, is not optimized for MPI and only a small fraction of its particle size distribution is large enough to contribute to MPI signal [64]. This means that getting enough detectable signal *in vivo* can only come from injection doses with relatively high iron mass. Additionally, coprecipitation reactions commonly are not capable of producing SPIONs with narrow size distributions and core sizes larger than 10 to 15 nm resulting in non-optimal nanoparticle phase. Even when adding oxidizing agents to these reactions, most produce maghemite as the final phase [62] or, in the case of Resovist©, [42] a mixture of maghemite and magnetite. By taking each of the preceding factors into consideration, it can be surmised coprecipitation based SPIONs are not promising for MPI applications at a commercial scale.

Thermolysis reactions show greater promise in the preparation of larger (core size, d_0, greater than 20 nm), monodisperse (log-normal size distribution parameter, σ, less than 0.1), and phase controlled (single-crystal magnetite) SPIONs that can thus be optimized for MPI. Thermolysis reactions involve the decomposition of an iron-containing precursor in the

presence of a high-boiling solvent and surfactant. Iron precursors that have been shown to produce monodisperse SPIONs include iron pentacarbonyl [65], iron acetylacetonate [66], iron oxyhydroxide [67], and iron oleate [68]. Of these, the most promising for commercial viability for MPI tracer preparation is iron oleate as shown by Park [69] and further optimized by Kemp [52].

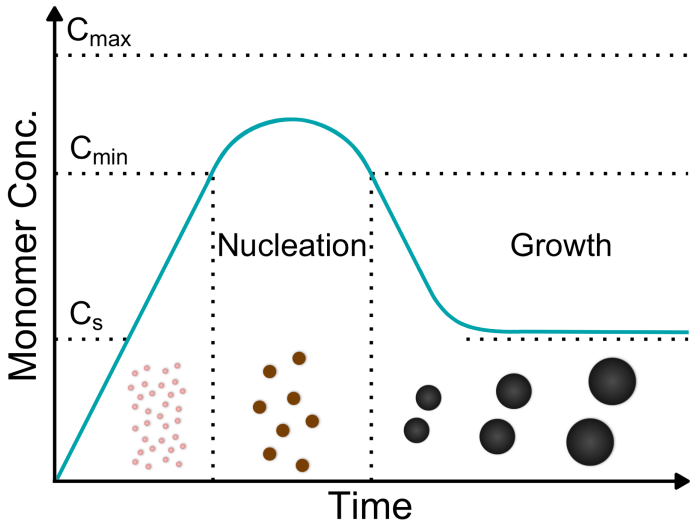

Figure 2.1: LaMer supersaturation curve illustrating the initial decomposition of precursor, nucleation, and growth of SPIONs given an initial concentration of precursor with none added during the growth phase.

Traditionally, the decomposition of organometallic iron precursors, nucleation, and growth has been described by the LaMer supersaturation theory [70]. This theory, as shown in Fig. 2.1, describes the decomposition of iron precursor increases the monomer concentration in solution until a minimum concentration is reached. At this point, nucleation occurs in a "burst" that rapidly decreases the monomer concentration below the minimum nucleation concentration. The nucleated nanoparticles subsequently consume the remaining monomer in solution in the growth phase. This theory predicts that the mean size and distribution of sizes depends on the number of nuclei that formed during nucleation. There have been attempts to force deviation from LaMer's supersaturation theory through continual addition

of organometallic precursor to the solution throughout the growth phase to prevent depletion of available monomer [71]. This method, however, does not appear to be scalable and sufficient control of size and size distribution is possible through thermolysis starting with total reactant quantities.

SPION size control in the thermolysis of organometallic iron precursors is dependent on manipulating the phases of the LaMer supersaturation theory through control of reaction temperature, surfactant, and surfactant-to-iron precursor ratio. Control of size is accomplished through variation of the molar ratio of surfactant-to-precursor where increasing the ratio leads to increased core size. For example, sizes from 5-30 nm have been grown by Yu [67] using iron oxyhydroxide as a precursor and varying only the surfactant-to-precursor ratio. It is also possible to vary the size by varying the initial concentration of iron precursor, but this affects the amount of free iron available during the nucleation and growth phase and generally results in less size distribution control.

As was discussed in Chapter 1, not all phases of iron oxide are viable candidates for use in MPI. Either maghemite and magnetite are needed, but it is desirable to reproducibly synthesize one phase over the other for the purposes of consistency and performance. Magnetite has a higher bulk saturation magnetization than that of maghemite and thus it is desirable to have phase control in SPION synthesis to get magnetite. Larger sizes of SPIONs (15 to 30 nm) generally can be oxidized to be solely magnetite, while smaller sizes (<10 nm) usually form maghemite under oxidizing conditions.

Thermolysis reactions require the use of an inert atmosphere to prevent uncontrolled oxidation of SPIONs and unsafe reaction conditions due to autoignition temperatures of solvent being below reaction temperature. It is suggested that small-scale thermolysis reactions may oxidize from as-nucleated wüstite to maghemite or magnetite through only the latent oxygen present after inert atmosphere purging and oxygen introduced through leaks. When approaching to commercially relevant reaction scale, uncontrolled oxygen presence is no longer sufficient fully oxidize SPIONs, and a controlled oxidation procedure must be employed. Chemical oxidation through an oxidizing agent such as trimethylamine N-oxide is possible,

but not advised due to unsafe use conditions. It is preferred to use an *in situ* oxidation through the introduction of oxygen diluted by an inert gas. This procedure was introduced for thermolysis of iron oleate at a large scale by Kemp [52]. Without the introduction of a 1% oxygen-99% argon gas flow as the tested reaction scale, a clear presence of a core-shell structure of wüstite and magnetite was present. When the 1% oxygen-99% argon flow is maintained during the growth phase of the reaction, pure or near-pure magnetite SPIONs are formed and are observed to perform significantly as tracers for MPI.

2.1.1 Methods

The SPIONs used in this work were prepared based on previously published methods [69, 52].

Iron oleate synthesis

Briefly, a solution of iron (III) chloride and sodium oleate were dissolved in a mixture of hexanes, ethanol, and water (liquid ratio 5:3:1.8). In a flask equipped with a cooled condensing column, this mixture was heated for 4 h at reflux (57 °C). The resultant iron oleate product was washed three times with deionized water and extracted in a separatory funnel. The organic phase was then collected, dried with sodium sulfate, and filtered with qualitative filter paper. The solvent was removed first by careful rotary evaporation, then by vacuum for at least 2 h.

Table 2.1: Approximate molar ratios of thermal decomposition synthesis of relatively small and large core sizes.

	Relative %	
Component	<10 nm	23 to 28 nm
iron oleate	5.0	3.6
1-octadecene	89.5	71.0
oleic acid	5.5	25.4

Thermal decomposition

Based on determined mass after solvent removal, iron oleate was diluted to the appropriate concentration with 1-octadecene and oleic acid, relative % of each illustrated for two size ranges shown in Table 2.1. The reaction mixture was placed under vacuum and heated at 50 °C overnight. Two bump bulbs were added to the reaction flask and the system purged by vacuum and argon gas. Under an inert atmosphere, the temperature was brought to 324 °C and held until nucleation occurred (observed as a color change to white brown) plus 15 min. The temperature was then lowered to 318 °C and a 1% oxygen/99% argon gas flow was added. The reaction was held in this state until 39 h had passed since the initial point of nucleation. The critical steps in the synthesis of SPIONs are illustrated in Fig. 2.2 including the general colors observed at each point. After the reaction was completed, the reaction solution was reheated to 50 °C and stirred to evenly distribute the SPIONs. They were then transferred to a glass bottle with a minimal amount of hexanes and temporarily stored at 4 °C until initial size characterization could be completed.

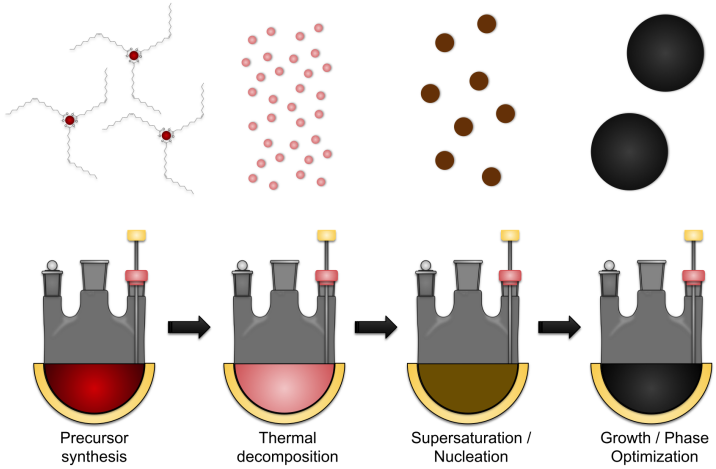

Figure 2.2: Notable steps, observed as changing color, in the synthesis and subsequent thermal decomposition of iron oleate in order to prepare SPIONs at a scale between laboratory and commercial.

Long-term storage

When desired and most often with SPION batches of appropriate size and narrow size distribution, it is possible to store and maintain the physical and magnetic properties after synthesis when appropriate steps are taken. First, the as-synthesized SPIONs, containing nanoparticles, 1-octadecene, oleic acid, hexanes, and synthesis by-products, are divided into multiple smaller glass vials, leaving minimal headroom in the vial. Each vial is then sealed with Parafilm, and they are placed in long-term storage at −80 °C. As long as this temperature is maintained, SPION batches can be made dispersible in aqueous solution and retain consistent magnetic properties for approximately 4 years.

2.2 SPION coatings

Nanomaterials are made dispersible in organic solvents and aqueous solution either *in situ* during synthesis or after the fact through a variety of methods. In this work, the focus is on coatings and coating methods associated with SPIONs synthesized through thermal decomposition of organometallic precursors.

2.2.1 Colloidal stabilization

The purpose of the inclusion of surfactants/ligand molecules in the synthesis of nanoscale materials is two-fold. Firstly, it allows for increased control of the growth mechanism through the association and dissociation of ligands throughout the growth phase. For example, ligands can be used to control the final shape of nanomaterials as some ligands bind preferentially to specific crystal planes as growth progresses. This prevents new atoms from binding where ligands are preferentially bound and forces growth in other crystal directions [72]. In the case of SPIONs for MPI, it is advantageous to use a ligand that does not increase shape anisotropy as spherical SPIONs with low anisotropy have better ac magnetization behavior compared to cube or pyramid-shaped particles which have higher anisotropy. It is clear from TEM images of SPIONs larger than 15 to 20 nm that highly symmetric faceting occurs, but this is due to

energy minimization from the growth of specific cubic crystal planes of iron oxide over others.

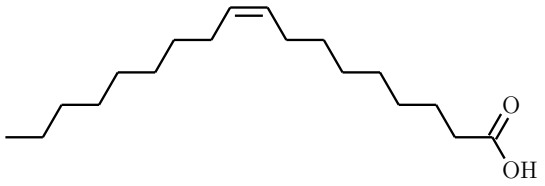

Figure 2.3: Chemical structure of oleic acid.

The second purpose for ligands in the preparation of nanoscale materials is their colloidal stabilization after initial synthesis. Without any ligand, forces promoting aggregation, such as energy minimization through the decrease of surface area and interparticle magnetostatic interactions, dominate. For this reason, colloidal nanomaterials are generally prepared with or coated after the fact with ligands that increase the amount of steric bulk on the surface and decrease the surface area-to-volume ratio which decreases the overall energy of the system [73]. Hydrophobic ligands are necessary to stabilize nanomaterials in the presence of organic solvents, such as hexanes, or organics that are long-chain and higher boiling for high-temperature reaction conditions, such as 1-octadecene.

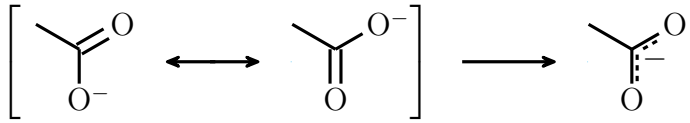

Figure 2.4: Carboxylate resonance and apparent delocalization of double bond and charge.

SPIONs synthesized by thermal decomposition of iron oleate are coated, most often, with oleic acid, the chemical structure of which is shown in Fig. 2.3. The carboxylic acid terminal group on oleic acid allows for electrostatic interaction and, more favorably, chemisorption onto the iron oxide surface. Also, the bonding between iron and oleic acid is made stronger by the formation of a carboxylate ion with a delocalized double bond and negative charge, as shown in Fig. 2.4, which results in a strongly adhering and stabilizing ligand.

Nanomaterials for biomedical applications are nearly always only useful when successfully dispersed in an aqueous solution. This presents a difficulty for SPIONs synthesized by thermal

decomposition of organometallic precursors as the reaction is carried out in organic solvents and the resulting capping ligands are hydrophobic. This means that SPIONs synthesized in this manner must be made hydrophilic through a phase transferring process. There are several routes through which phase transfer is accomplished, each with varying degrees of effectiveness depending on the type of nanomaterial. The primary concerns when discussing aqueous dispersions for biomedical applications is their hydrodynamic size, size distribution, and stability, both short- and long-term, in solution.

2.2.2 Excess ligand removal

The first step that must be taken to make hydrophobic SPIONs dispersible in aqueous solution is to remove the excess amount of non-adhered ligand, reaction solvent, and any decomposition by-products of ligand and solvent from initial synthesis. This is accomplished through repeated dispersion and precipitation of SPIONs in appropriate organic solvents. This process continually dilutes the concentration of long-chain organics and eventually removes enough for the amount leftover to be negligible for practical purposes. It is important to note that this process does not remove the ligand chemically bound to the surface of SPIONS as would using a ligand stripping agent like Meerwein's reagent [74]. Instead, the hydrophobic coating of ligands remains to stabilize SPIONs in organic solvent until additional coating or ligand exchange procedures are carried out.

Purification procedure

SPIONs were washed in different solvent mixtures to remove synthesis by-products and excess reaction solvent and surfactant. The solvent mixtures were ethyl acetate (100%) once, hexanes and ethyl acetate (50%/50%) once, and hexanes/acetone (40%/60%) five times. Each solvent mixture was added and then sonicated with the SPIONs for 30 to 60 s. The container was then placed on a strong magnet until the SPIONs had entirely moved in solution to be adjacent to the magnet. The supernatant was then removed by Pasteur pipette, and the

next solvent mixture added. After the final removal of supernatant, the SPIONs were placed under vacuum for approximately of 24 h to remove any trace amounts of solvent.

2.2.3 Ligand exchange

Once the concentration of excess long-chain organic molecules is dilute enough that they can be considered negligible, it is then possible to alter the surface coating of SPIONs such that they are hydrophilic and able to be dispersed in aqueous environments. There are multiple methods through which this can be accomplished, the first being the removal and exchange of the hydrophobic ligand with one that is hydrophilic. This process, called ligand exchange, has the capability of being efficient and offers a wide variety of possible ligands and surface functionalization.

Ligand exchange is possible due to the non-constant binding state of any ligand molecule on the surface of a nanomaterial. When SPIONs are in solution, there are association and dissociation processes of ligand molecules constantly occurring where the amount of time it is associated outweighs the dissociation. This equilibrium is thermodynamically driven and thus is temperature dependent with additional consideration for the binding strength of the ligand and nanomaterial surface. The generally accepted mechanism through which ligands are replaced in ligand exchange is the temporary and reversible association of the new ligand, Y,

$$\mathrm{MX} \quad + \quad \mathrm{Y} \quad \rightleftharpoons \quad \mathrm{MX \cdot Y}$$

followed by the dissociation of the old ligand, X.

$$\mathrm{MX \cdot Y} \quad \longrightarrow \quad \mathrm{MY + X}$$

If the new ligand is more strongly binding to the surface of the nanomaterial then it dissociates less frequently and is essentially permanent concerning the number of new ligands present on a surface. In most cases, nanomaterials are mixed with an excess of the new ligand to shift the equilibrium balance of this process further in favor of the new ligand. Additionally,

these ligand exchange processes are executed at elevated temperatures to increase the rate of dissociation for the old ligand and allow more time for the new ligand to associate with the surface.

One of the most commonly employed ligands in ligand exchange methods is molecules containing a thiol functional group which is a sulfur-containing variant of an alcohol functional group. Ligand exchange methods employing thiol-containing molecules have been used to stabilize noble metal nanoparticles in aqueous solution for more than two decades [75, 76] due to the strong affinity of thiol functional groups for the surface of noble metals [77]. In the case of SPIONs, recent examples of ligand exchange methods include hydroxyl reactive agents to replace oleic acid molecules [78] and high-temperature reactions of iron(III) acetylacetonate with 1,2-hexadecanediol to replace oleic acid and oleylamine [79]. In each of these cases, the size of the new ligand of the surface of the nanomaterial is relatively small (50 to 500 $\mathrm{g\,mol^{-1}}$) which is a viable candidate for materials were the primary mechanism of aggregation is electrostatic interaction. In these cases, the new ligand can be a charged species allowing for electrostatic repulsion between individual nanomaterials. These ligands are often insufficient to maintain colloidal stability in high salt concentration solutions, as are observed in biological environments and solutions, where the free ions act as bridges between charged nanomaterials and promote, rather than prevent, aggregation.

Where electrostatic repulsion is no longer sufficient, the addition of steric bulk to nanomaterial coatings is a viable option to promote colloidal stability. In these situations, polymers or biological moieties are commonly employed where they still include functional groups capable of adhering the molecule to the surface of a nanomaterial. In this work, the focus is on polymeric entities due to their relative non-reactive structure and ability to vary molecular weight.

The most common functional groups utilized in ligand exchange on the surface of SPIONs are catechols, which are aromatic rings with two hydroxyl groups in ortho positioning, and triethoxysilanes, which have a silicon atom bound to three ethyl groups through oxygen atoms. Each of these functional groups is easily bound to polymers such as polyethylene

glycol (PEG) allowing for both strong chemisorption to the surface of SPIONs and colloidal stability in aqueous environments with hydrophilic steric bulk. Examples of catechol and triethoxysilane terminated PEG molecules are shown in Fig. 2.5 where the variant of catechol is dopamine.

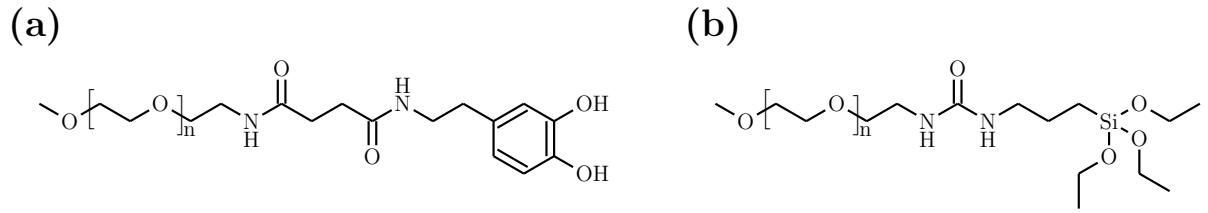

Figure 2.5: Chemical structures of dopamine (a) and triethoxysiloxane (b) terminated PEG.

As previously discussed, the binding strength of the functional group dictates how much of the oleic acid on the surface of hydrophobic SPIONs is replaced. As long as the majority of oleic acid is replaced, SPIONs are dispersible in aqueous solution, but it is advantageous to replace as much as possible. Previous work has shown that oleic acid is readily replaced by dopamine and nitro-substituted dopamine functional groups making them ideal options for ligand exchange procedures. Phosphonate, amine, and carboxylic acid functional groups are also viable options, but have less affinity for the surface of SPIONs and thus replace a smaller fraction of oleic acid [80]. Triethoxysilane was not included in that study, but is equivalent to or better than catechol functional groups due to the possibility of generating three iron-oxygen bonds on the surface of SPIONs.

Previous work in the Krishnan group has included the use of dopamine and triethoxysilane terminated PEG for the coating and aqueous dispersion of mid-sized to ultra-small SPIONs. Mid-sized SPION ligand exchange was successful through the initial silanization with an anhydride containing silane and subsequent conjugation with amine terminated PEG [81]. Ultra-small SPIONs were coated with dopamine and triethoxysilane terminated PEG prepared before the ligand exchange process [47] to generate SPIONs relevant in MRI applications. A variation on this method has since been employed in the ligand exchange of ultra-small

SPIONs for use in on-going studies of short- and long-term iron metabolism after injection in mice.

Silanization procedure

SPIONs were made dispersible in aqueous solution through a modified approach to previously published silanization methods [47]. Briefly, ultra-small SPIONs were washed by dispersion, sonication, and precipitation in the following mixtures of solvents: ethyl acetate:ethanol (50%/50%) once, ethyl acetate:ethanol:hexanes (35%/35%/30%) twice, acetone:ethanol:hexanes (65%/25%/10%) three times, and acetone:hexanes (85%/15%). After the final precipitation on a magnet was carried out, the solvent was decanted, and the SPIONs were dried under vacuum for 24 h. The dried SPIONs were weighed and dispersed by sonication in chloroform at a concentration of $1\,\mathrm{mg\,mL^{-1}}$. Triethoxysilane-functionalized methoxy-PEG (Layson Bio, Inc. MW = $10\,\mathrm{kg\,mol^{-1}}$) was added in a PEG:SPION mass ratio of 21:1. The glass vial was sealed with Parafilm and placed on a rotary shaker table at 50 rpm and 50 °C for 48 h. The newly PEG-coated SPIONs were precipitated by adding hexanes until the solvent became opaque. The SPIONs were precipitated on a magnet and washed, as before, with the following solvent mixtures: ethanol:hexanes (10%/90%) once, ethanol:chloroform:hexanes (20%/5%/75%) three times, chloroform:hexanes (15%/85%) once, and hexanes (100%) once. The final solvent was decanted and the SPIONs dried under vacuum for 24 h. They were readily dispersed in deionized water at a concentration of $2\,\mathrm{mg\,mL^{-1}}$ through 30 min of sonication. The SPIONs were transferred to 1X PBS by gel chromatography in a PD-10 column equilibrated in 1X PBS. Their final concentration was determined by elemental analysis of iron content.

2.2.4 Hydrophobic-hydrophobic interaction coating

A significant limitation of the ligand exchange process is the size of possible ligands that can be directly adhered to the surface of nanomaterials. While polymers can be synthesized with high molecular weights ($> 50\,\mathrm{kg\,mol^{-1}}$) and biological molecules such as proteins can similarly

have high molecular weights, the total amount of steric bulk on the surface of a nanomaterial is still limited. In the case of nanomaterials such as noble metals and fluorescent quantum dots, this is not a significant concern in their final application. However, SPIONs are magnetic, and thus the interactions between adjacent particles must be taken into consideration. These magnetostatic interactions, or dipole-dipole interactions, between two or more magnetic nanoparticles, affect how they behave in a given application and is a function of the distance between them. The effect of magnetostatic interactions is covered in more detail in §5, while this section discusses the coating mechanism of SPIONs dispersed in aqueous environments where magnetostatic interactions become minimal to a non-factor.

The hydrophobic coating, oleic acid, on SPIONs prepared by thermal decomposition in their as-synthesized state allows for more than stabilization in organic solvents. The hydrophobic nature of oleic acid is such that it is a higher energy state for water molecules to interact with the non-polar molecule than it is for it to interact with another non-polar molecule. This tendency for hydrophobic molecules to closely associate with other hydrophobic molecules allows for a convenient coating mechanism of SPIONs that doesn't require the removal and replacement of oleic acid.

Here, it is possible to add another molecule or polymer that is partially hydrophobic and partially hydrophilic, defined as an amphiphilic molecule, to a dispersion of SPIONs. To minimize the energy of the system, the hydrophobic SPION coating associates with the hydrophobic group of the amphiphilic molecule, which leaves the hydrophilic group exposed to water and ultimately stabilizing the SPION in aqueous environments. Additionally, the amphiphilic molecule can be a relatively low molecular weight (30 to 50 $\mathrm{kg\,mol^{-1}}$) or have a very large molecular weight (500 to 1000 $\mathrm{kg\,mol^{-1}}$) depending on the desired amount of steric bulk on the surface of the SPIONs.

Pellegrino *et al* demonstrated the first use of poly(maleic anhydride alt-1-octadecene) (PMAO), as shown in Fig. 2.6a, with a molecular weight of 30 to 50 $\mathrm{kg\,mol^{-1}}$ for this type of hydrophobic-hydrophobic interaction transfer of nanomaterials from organic solvent to aqueous solution [43]. They were able to stabilize 9.2 nm average diameter SPIONs in water

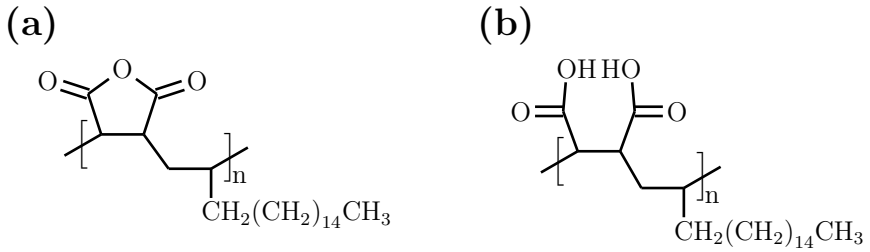

Figure 2.6: Chemical structure of poly(maleic anhydride alt-1-octadecene) (PMAO) without (a) and with (b) hydrolysis of the anhydride ring.

(as well as Au, $CoPt_3$, and CdSe/ZnS nanocrystals). The primary mechanism of stabilization with PMAO is the increased steric bulk over most ligand exchange processes, but an additional stabilization component is possible when its anhydride rings are hydrolyzed to carboxylic acids through the addition of strong or weak base. The presence of carboxylic acids, which are generally deprotonated and charged, adds electrostatic repulsion between adjacent SPIONs and increases stability in aqueous solution. This holds for low salt content solutions, but decreased stability is observed in high salt content solutions due to the bridging effect of ions in solution.

It is possible to neutralize the charge from carboxylic acids through the addition of small methyl terminated capping molecules or through cross-linking of carboxylic acids with amines with EDC-NHS coupling reactions, as shown in Fig. 2.7. The Krishnan group has readily utilized this method of coating SPIONs with PMAO and further conjugation for their stabilization as well as functionalization with molecules of interest for *in vitro* and *in vivo* applications [49, 61].

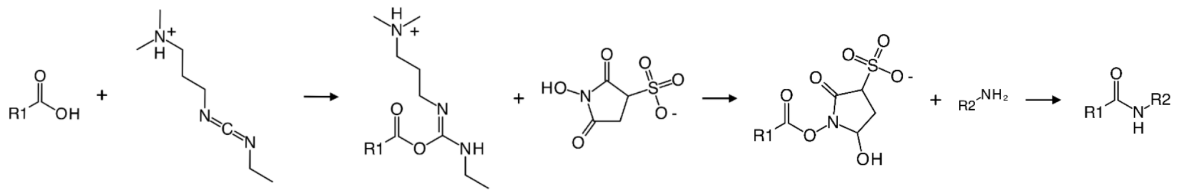

Figure 2.7: EDC-NHS coupling reaction of carboxylic acids and primary amines including urea intermediate and sulfo-NHS amine-reactive ester.

While the PMAO method of coating SPIONs is viable for core diameters up to approximately 20 to 22 nm, it does not sufficiently separate larger core diameters and thus further increases to the steric bulk surrounding SPIONs must be employed. One such improved method for phase transferring SPIONs to water was developed by Yu *et al* who used a copolymer of PMAO and polyethylene glycol (PEG) in place of PMAO alone [44]. The PMAO molecule has an average of 114 anhydride rings along its polymer chain that can serve as binding sites for PEG molecules with appropriately reactive terminal functional groups. The best option, in this case, is a primary amine which is readily reactive with anhydrides to form a stable amide bond, the reaction of which is illustrated in Fig. 2.8. The number of PEG molecules reacted with PMAO and filling a portion of the available reaction sites, also known as a loading percentage, affects the stability of the SPIONs in aqueous solution as well as the *in vivo* circulation half-life.

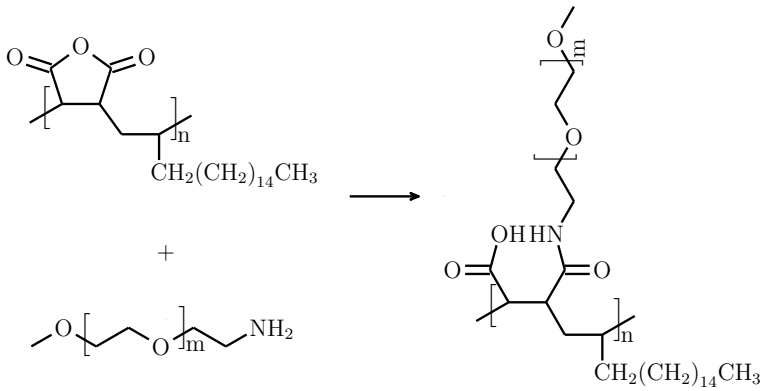

Figure 2.8: Amide formation reaction of poly(maleic anhydride-*alt*-1-octadecene) (top-left) and polyethylene glycol (bottom-left) used to make the amphiphilic co-polymer PMAO-PEG (right).

Previous work has determined that an optimal 18.8% loading of PEG on PMAO results in optimal blood half-life in mice when utilizing 20 kg mol^{-1} PEG [12]. This level of loading results in SPIONs with low surface charge and is excellent for long circulation *in vivo*, but it is important to note that lower loading percentages (1-5%) are more optimal for cell loading applications and others where high uptake is desired. This is discussed in more detail in Chap. 4. In this work and especially in cases involving SPIONs exposed to cellular environments,

loading percentages were maintained at approximately 5%.

Amphiphilic polymer synthesis procedure

As synthesized SPIONs were made hydrophilic through the addition of amphiphilic polymer coatings. Briefly, poly(maleic anhydride-alt-1-octadecene) (PMAO) and amine-terminated polyethylene glycol (PEG) were each added to solutions of dichloromethane (DCM) and small amounts of triethylamine (Et_3N), allowed to dissolve fully; then the solutions were combined in one container. The reaction was allowed to proceed for 48 h and while watching for signs of reactions progress noted by increasing viscosity of the solution as observed by changing stir bar procession under constant set point.

The resulting copolymer was dried by rotary evaporation, placed under vacuum for several days, and then dissolved in deionized water. The new solution was transferred to 100 kDa cutoff tubing and put in a beaker with deionized water. The water was replaced several times over two to three days, and the purified product was then transferred to a round-bottom flask. The solution was frozen in a dry ice/acetone bath while spinning at 300 rpm. The copolymer was lyophilized over four days and the final product collected and weighed. It was then stored under vacuum or inert gas until used in the SPION coating process.

Amphiphilic polymer coating procedure

Previously purified and dried SPIONs were weighed and chloroform added to a concentration of $1\,\mathrm{mg\,mL^{-1}}$. Amphiphilic polymer was then added in a ratio of 10 mg per 1 mg SPIONs and allowed to dissolve overnight while on a shaker table. The solvent was then removed by rotary evaporation, leaving behind a film of SPIONs and polymer coating the container. This was dried under vacuum for 24 h followed by the addition of deionized water to a concentration of $1\,\mathrm{mg\,mL^{-1}}$. The new solution was sonicated for approximately 3 h. The SPIONs were transferred to 1X PBS by gel chromatography in a PD-10 column equilibrated in 1X PBS. SPIONs in aqueous solution were stored in glass vials or Falcon tubes, sealed with Parafilm, at 4 °C until ready for use.

2.3 SPION surface functionalization

SPION coatings are crucial to their stability in solution, magnetic performance, and *in vivo* behavior, but the ability to conjugate various ligands to the coating is potentially most important for biomedical applications long-term. As was previously discussed, it is possible to conjugate amine functionalized ligands to the PMAO backbone of the amphiphilic polymer coating through EDC-NHS coupling reactions. There are limitations to this approach that include potential steric hindrance and incomplete coupling when the reaction is attempted in the presence of PEG. The nature of PEG conformation in solution is complex, but the key aspect here is that it can form a brush-like structure that makes the molecule's size large relative to the surface of the SPION. When this happens, the backbone is more difficult to access, in particular for high molecular weight ligands such as proteins.

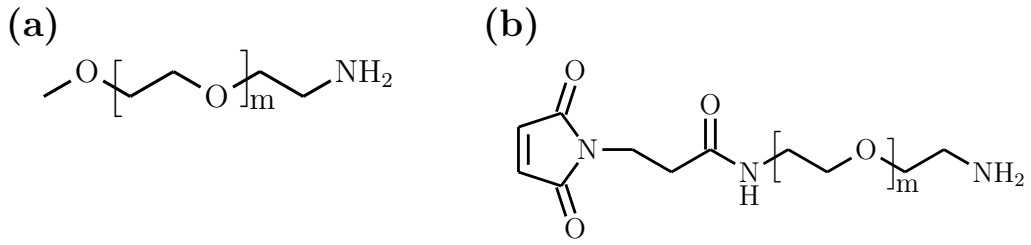

Figure 2.9: Chemical structure of PEG with methoxy (a) and maleimide (b) terminal functional groups.

This limitation of EDC-NHS coupling leaves only the terminal functional group of PEG as a viable location for further functionalization. So far, the PEG portion of the amphiphilic polymer coating discussed here has included only non-reactive methoxy terminal groups that do not allow for the addition of new functionalization. It is thus important to consider other potential PEG terminal functional groups that readily allow for further functionalization to occur. Methoxy-terminated PEG, as shown in Fig. 2.9a, can be replaced by a reactive maleimide terminal group, as shown in Fig. 2.9b, to allow for fast and uncomplicated functionalization of new ligands.

The maleimide functional group is chosen for its ability to react with thiol, or sulfhydryl

groups, present or that can be formed on a wide variety ligands. Since the 1950's, maleimides have been shown to efficiently react with sulfhydryl group to form stable bonds [82]. Since then, maleimide-sulfhydryl chemistry has been frequently employed in coupling reactions of maleimides and thiol containing molecules. The mechanism, illustrated in Fig 2.10, involves nucleophilic attack of the double bond in the maleimide by the thiol group resulting in a thioether formation and the loss of a H^+.

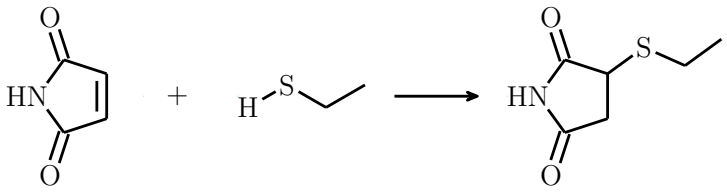

Figure 2.10: Reaction of maleimide and thiol functional groups to form thioether bonds.

2.3.1 Methods

Maleimide-terminated PEG containing amphiphilic polymer is synthesized in the same manner as in Sect. 2.2.4, but with maleimide-terminated instead of methoxy-terminated PEG. Also, the reaction is carried out while protected from light to prevent degradation of the maleimide functional group.

2.3.2 Results & discussion

Multiple instances of this maleimide-terminated PEG functionalization platform have been used in collaboration with Krishnan Group members. The first case being for the purposes of targeting and imaging of tumors. Here, lactoferrin, a brain cancer targeting protein [49], was thiolated and conjugated to SPIONs coated with maleimide containing PMAO-PEG, as depicted in Fig. 2.11. It was shown that lactoferrin functionalized SPIONs were able to be uptaken with higher efficiency than non-lactoferrin functionalized SPIONs in tumors *in vivo* consisting of brain glioma cells [20].

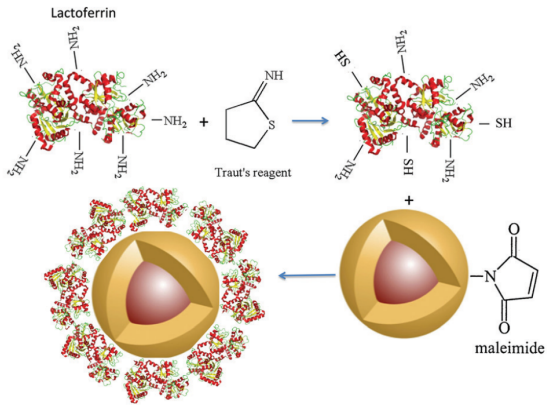

Figure 2.11: Method for the functionalization of maleimide-containing PMAO-PEG coated SPIONs with lactoferrin. Adapted from [20].

The second instance of the maleimide-terminated PEG functionalization platform utilized for further studies in the Krishnan Group is in studying the *in situ* effects of coating on colloidal stability. Here, L-cysteine and an arginine-rich peptide, both thiol containing and shown in Fig. 2.12, were each independently conjugated to SPIONs coated with maleimide-containing PMAO-PEG. These SPIONs were then observed *in situ* in a liquid environment in a TEM to characterize how well the coating protected SPIONs under an electron beam and changing pH of the solution. It was shown that arginine-rich peptide functionalized SPIONs experience irreversible degradation of the core structure and redeposition within the positively charged coating. L-cysteine, which is zwitterionic and contains positive and negative charge, showed reversible degradation depending on the electron beam dose and resulting pH of the aqueous environment surrounding the SPIONs [83].

2.4 Summary

The methods for synthesis and coating addressed in this chapter have been chosen for their ability to prepare SPIONs that perform optimally in *in vivo* applications of MPI. This discussion is important to inform why each route was selected and the benefits of each over the available options. Specifically thermal decomposition of organometallic precursors was used to prepare SPION cores due to its increased control over size, size distribution, and

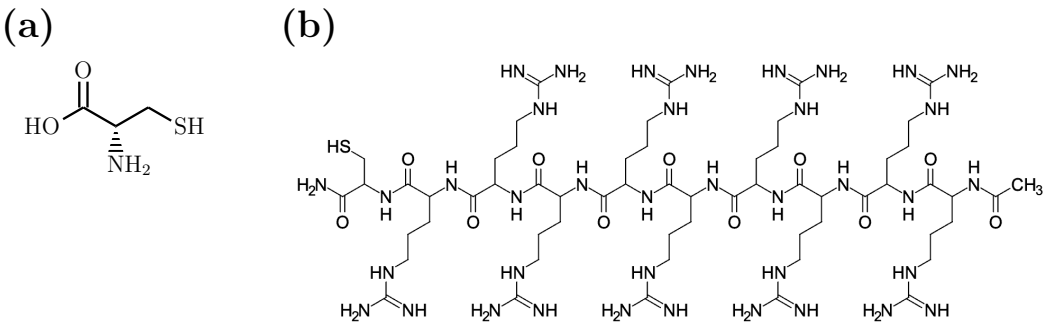

Figure 2.12: Chemical structure of L-cysteine (a) and an arginine-rich peptide (b) conjugated to SPIONs.

phase as compared to coprecipitation. Amphiphilic polymer coatings were chosen to transfer SPIONs to aqueous solution based on the available mechanisms to control size and surface charge as well as the numerous options for surface functionalization with minimal negative effects on the beneficial aspects of this coating. The next chapter is an introduction to the techniques necessary to characterize SPIONs before they can be use in any real-world applications.

Chapter 3

CHARACTERIZATION OF SPIONS

The characterization techniques necessary in working with MPI optimized SPIONs are presented here including background, sample preparation, and standard experimental analysis.

3.1 Size, morphology, and crystal structure

There are several methods utilized in the characterization of SPIONs including direct physical observation of size and morphology and observing their interaction of high energy photons to obtain crystal phase information. The following sections include background information on the suitable technique for these characterizations, sample preparation methods, and explanations and examples of data analysis.

3.1.1 Transmission electron microscopy

Transmission electron microscopy (TEM) is an imaging technique available when materials are, or can be made to be, transparent to accelerated electrons, and greater magnifications and better resolution than those achievable through conventional light microscopy methods are possible.

Background

Light microscopy provides for imaging of many materials with continually improving resolution due to technological advancements, but there are limits preventing imaging of sub-cellular and even atomic resolution features. In particular, the limiting factor is the Abbe diffraction limit which accounts for the interaction light waves converging to a position smaller than the

wavelength of that light. The resolution, d, wavelength, λ, and the numerical aperture, NA, are related by

$$d = \frac{\lambda}{2\mathrm{NA}} \tag{3.1}$$

It is possible to push the resolution to smaller and smaller sizes by using smaller wavelength light such as ultraviolet and x-ray, but the ability to detect as wavelength decreases becomes more difficult. The more prudent option is the use of another probe that is capable of achieving a smaller wavelength such that the diffraction limit is no longer a concern. Electrons are an ideal candidate as they can be readily generated, accelerated and manipulated through electric and magnetic fields, and are easily detected. The details of how electrons are generated and focused will not be discussed here, but can be found in [84].

Once the electrons have been focused to the appropriate sample region, they pass through the sample and are diffracted or scattered, then focused again onto a detector for image collection and interpretation. The electron beam can be passed through the sample under two general conditions including parallel and converged-probe. Parallel beam illumination allows for an equal flux of electrons through a region of interest while converged-probe focuses electrons to a tiny point and rasters the beam across the region of interest to generate an image. Parallel beam and converged-probe illumination are primarily associated with bright-field and scanning imaging modes, respectively.

Sample preparation and data collection

Samples containing only SPIONs discussed in this thesis were prepared by the following method, utilized unless otherwise noted. SPIONs were purified as described in §2.2.2 to remove excess long-chain organic molecules and by-products from initial synthesis. Purified SPIONs were then dried under vacuum, weighed, and dispersed in chloroform at a concentration between 0.9 and 1.0 mgFe/mL. A 200 mesh pure carbon-coated copper TEM grid was suspended by locking tweezers, carbon side up, and 5 µL of SPION dispersion was pipetted

onto the grid. The chloroform was allowed to evaporate, and the grid was transferred to a grid box for further drying under vacuum and storage.

Imaging of these samples was carried out using an FEI Tecnai G2 F20 Supertwin with a Gatan CCD camera (FEI Company, Hillsboro, OR, USA). This instrument was operated at 200 kV and typical imaging conditions incorporated the use of the objective aperture. Further, images collected for size analysis were intentionally maintained at a magnification of 19,500x when possible as this provided a balance of SPIONs per image and ability for quality image analysis by software macro in the image processing software ImageJ [85]/Fiji [86].

Experimental analysis

The contrast between the SPIONs and the background is crucial to getting a quality characterization of size with a significant number of objects counted. If the contrast is good enough, the analysis software cannot readily distinguish between SPIONs that need to be measured and the background or other material. An objective aperture is used to facilitate higher contrast in TEM imaging. It is a piece of metal with a smaller circular opening situated in the TEM column below the specimen and objective lens. It is thick enough to block electrons that are scattered at high angles by aberrations or internal diffraction in the sample. The result is a lower intensity of electrons that reach the imaging detector, but those that do are of high contrast between given areas of the specimen. The amount of increased contrast is controlled by the size of the circular opening in the objective aperture with smaller openings increasing contrast more.

Analysis of images collected for size analysis was carried out through the use of a macro run in the image processing software ImageJ. The macro is presented in full in Appendix D. Briefly, the macro filters noise from the original image, generates a black and white image based on user-defined or automatically generated contrast points, identifies circular objects in the new image based on a degree of circularity set by the user, and finally generates and exports a list of objects that meet the criteria as well as their characteristics. This macro depends on accurate calibration of the pixel size in each image which can be determined from

metadata or measurement of an embedded scale bar. Metadata, in this case, is the most accurate and fast method for inclusion of pixel size in the macro workflow.

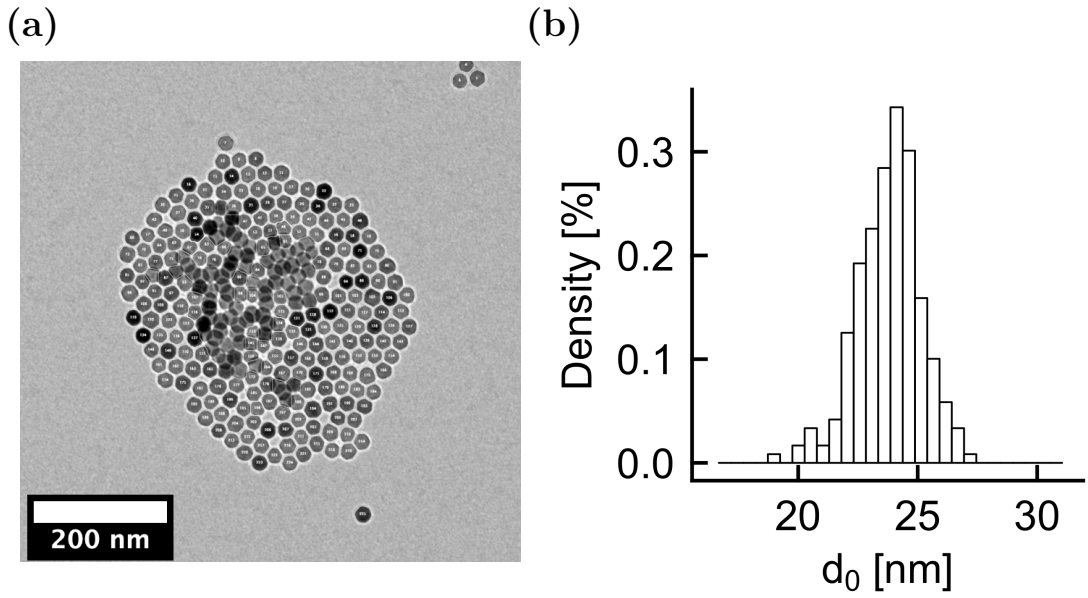

Figure 3.1: Example image of SPIONs with those outlined in green when meeting macro defined parameters for size analysis (a) and output histogram of sizes from a single image (b).

Example images of identified and outlined SPIONs and a histogram of sizes from a single image is shown in Fig. 3.1. It is important to note that the sizes from an individual image do not follow a well-defined distribution due to the low number of counted particles. For this reason, many images are collected, analyzed by an ImageJ macro, and compiled into a histogram of sizes. The histogram is generated with the binning being automatically determined by the Freedman-Diaconis rule [87]. A log-normal distribution is fitted to the histogram where the use of log-normal is based on prior assessments of magnetic nanoparticle syntheses and resulting distributions [88]. The probability density function of a log-normal distribution is shown in Eq. 3.2 where d is the diameter of the SPION and σ is the distribution

parameter;

$$f(d) = \frac{1}{d} \cdot \frac{1}{\sigma\sqrt{2\pi}} \exp\left(-\frac{(\ln d/d_0)^2}{2\sigma^2}\right) \tag{3.2}$$

The fitting process gives two values including an average diameter, d_0, and log-normal distribution parameter, σ, and the probability density function can be compared to the histogram of sizes. Examples are shown in Fig. 3.2 with Fig. 3.2a and Fig. 3.2b illustrating how fits and resulting values vary based on the number of measured SPIONs.

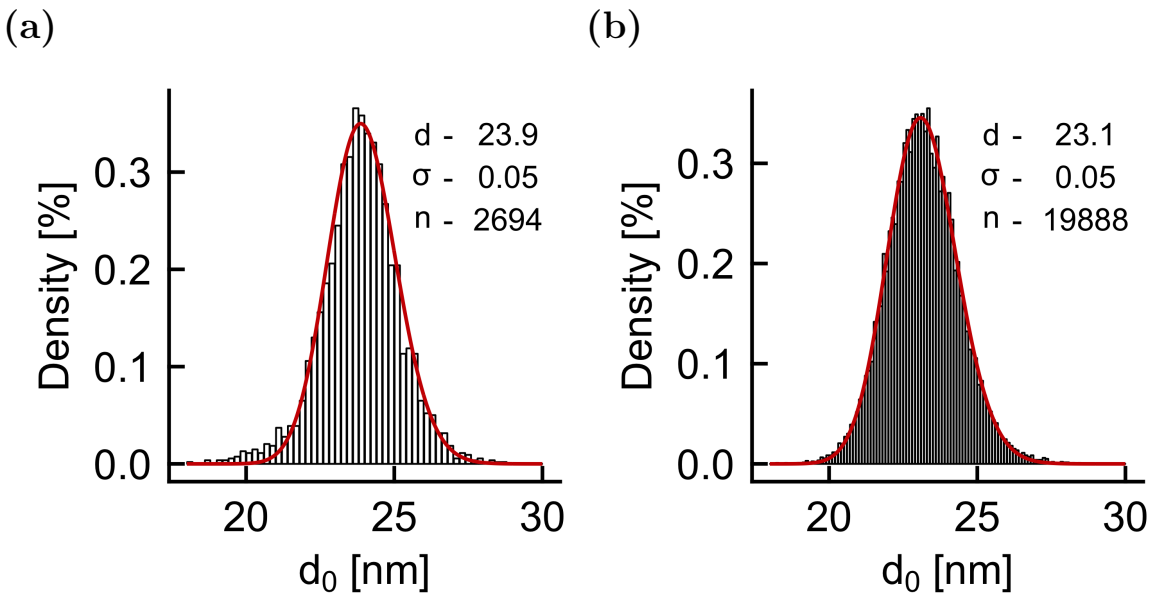

Figure 3.2: Example histograms of low (a) and high (b) counts, n, and associated log-normal probability densities (red lines) for the same batch of SPIONs.

In this case, the higher count, n, shows closer agreement to the histogram of sizes and the size is determined to be slightly smaller than the lower count. A minimum of 2000 correctly identified SPIONs is reasonable, but higher than 10,000 is desired. Also, images should be collected from a variety of positions on the TEM grid to diversify the sampling as much as possible. While this shows an improvement on the statistical significance of the size determined through TEM, it is important to remember that several thousand is a miniscule

percentage of the total number of SPIONs in a given batch, which is on the order of $1x10^{15}$ to $1x10^{22}$ SPIONs.

3.1.2 X-ray diffractometry

As was discussed in §1.2, there are four crystal phases of iron oxide that are possible to generate when preparing SPIONs. Only two, magnetite and maghemite, are of use in MPI and thus it is essential to know what reaction conditions are capable of generating one of the two. X-ray diffractometry (XRD) is one method used for determining the crystal phase. The principle of diffraction is discussed first followed by the preparation and analysis of SPION samples.

Background

XRD is accomplished by the generation and bombardment of x-ray radiation onto a crystalline material. X-rays are first generated by the acceleration of electrons at a high enough energy, called the excitation potential, at a pure material to eject core electrons. Once the core electron has been ejected, a higher energy electron falls into the lower energy core level and releases a photon. The energy fo the photon is characteristic of the material and more specifically the core and higher energy electron pair causing the photon. The most common materials used for x-ray generation in XRD are copper, iron, molybdenum, and tungsten with copper K_α being used prominently.

Once the x-rays are generated, they are directed towards the material of interest through a series of slits to eliminate extraneous and incorrect energy photons. When the x-rays interact with crystalline materials, diffraction occurs if the Bragg condition is satisfied and constructive interference of parallel photons occurs [89]. This requires a repeating lattice of atoms with consistent interplanar spacing, d. The interaction of x-rays and crystalline materials is illustrated in Fig. 3.3 where both the incident and diffracted x-rays are parallel

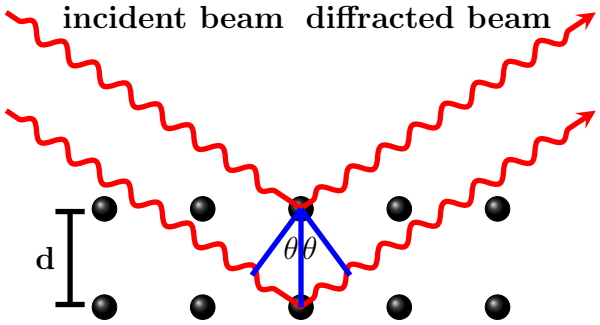

Figure 3.3: Diagram of atoms and x-ray photon beam interactions in an ordered crystal resulting in diffraction at an angle of 2θ and satisfying Bragg's Law.

and have traveled different distances based on Bragg's law

$$n\lambda = 2d \sin\theta \tag{3.3}$$

where n is the diffraction order, λ is the wavelength of incident photons, and θ is the scattering angle.

Sample preparation and data collection

Samples for XRD are generally powders where there is enough mass to fill a small indentation in a sample holder. It is possible, but difficult to prepare enough SPIONs to meet this mass requirement and thus samples are generally prepared with an awareness that signal noise is an on-going concern. First, double-sided tape is placed across the width of a standard glass microscope slide. SPIONs are purified as to remove excess long-chain organics, following the procedure in §2.2.2, and dried under high vacuum for at least 2 h. The glass vial containing the SPIONs is then tapped gently against a lab bench to release them from the inner surface and allow their removal from the vial. The SPIONs, now a free-flowing black powder, are poured onto the double-sided tape, and a small spatula is used to spread the powder so that most of the tape is covered. Approximately 3 mg is necessary, but the applied layer of powder should be as thick as possible. The microscope slide with the sample is then labeled and stored in a microscope slide box. It should not be left in ambient air for more than 24 h

before analysis by XRD.

In the specific case of observing phase evolution, SPIONs initially synthesized by thermal decomposition of organometallic precursor under inert atmosphere were oxidized in ambient air. The as-synthesized SPION solution was heated to 100 °C at 5 °C min^{-1} while stirring at 400 rpm. 5 mL aliquots were taken at semi-regular intervals of 0, 3, 6, and 12 h. Then, each aliquot was purified and XRD samples prepared as previously described.

Table 3.1: Diffracting crystal planes for magnetite and maghemite with associated 2θ values, interplanar spacing, and relative intensities. Values obtained for magnetite from PDF #19-0629 [90] and maghemite from PDF #39-1346 [91].

Phase	2θ [°]	d [Å]	Rel. %	(hkl)
Magnetite	18.270	4.852	8	(1 1 1)
	30.095	2.967	30	(2 2 0)
	35.423	2.532	100	(3 1 1)
	37.053	2.424	8	(2 2 2)
	43.053	2.099	20	(4 0 0)
	56.944	1.616	30	(5 1 1)
	62.516	1.485	40	(4 4 0)
Maghemite	30.241	2.953	35	(2 2 0)
	35.631	2.518	100	(3 1 1)
	37.250	2.412	3	(2 2 2)
	43.284	2.089	16	(4 0 0)
	57.273	1.607	24	(5 1 1)
	62.926	1.476	34	(4 4 0)

A Bruker F8-Focus X-ray diffractometer was used for this work including a copper K_α radiation source ($\lambda = 1.54$ Å) and operating voltage and current of 40 kV and 40 mA, respectively. Additionally, a monochromator was utilized to remove fluorescence caused by excitation of the iron K-edge by copper K_α radiation. This results in much lower signal but allows for observation of iron oxide XRD peaks. The samples were analyzed from a 2θ range of 25° to 70° in increments of 0.03° and a 3 s dwell time.

Experimental analysis

To determine if either magnetite or maghemite is present is SPION samples, the diffraction patterns are compared to known peak databases for these materials as are shown in Table 3.1. Six peaks have a high enough relative intensity to be detected and fall within the observed 2θ range for these two crystal phases. One limitation in using XRD for determination of iron oxide crystal phase lies in the nearly identical interplanar spacings and 2θ peak positions for magnetite and maghemite. Even with careful inclusion of a standard to appropriately shift peak positions, distinguishing between these iron oxide phases is tremulous. It is not the goal of this work determine which is explicitly present and further information on determining if magnetite or maghemite are the present crystal phase can be found in [92].

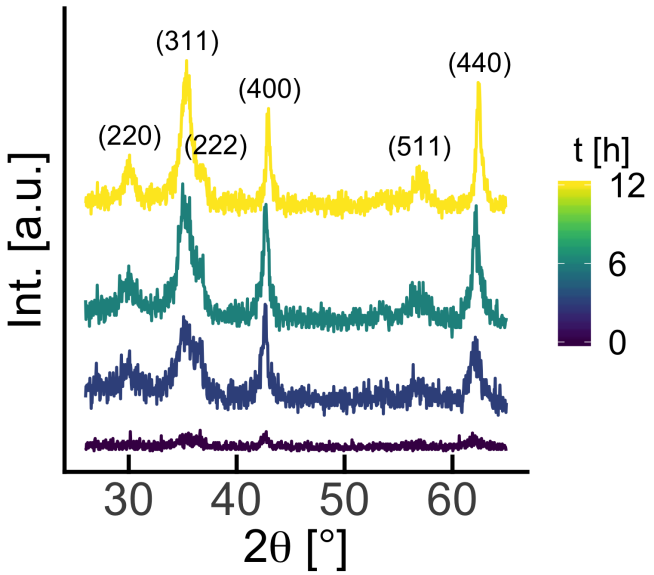

Figure 3.4: Phase evolution observed by XRD following time-dependent oxidation of SPIONs. At 0 h, there is minimal intensity and broad peaks associated with partially crystalline or multiphase nanoparticles. At 3 h, there is significantly higher peak intensity and narrow peaks that can be associated with magnetite or maghemite. This improvement continues through the 6 h and 12 h oxidation times.

By knowing the peaks to look for, it is possible to observe the phase evolution of SPIONs

from a non-crystalline or mixed phase of wüstite and magnetite to pure magnetite or maghemite. SPION phase during oxidation in ambient air was observed over a 12 h span. Fig. 3.4 at 0 h shows minimal intensity and broad peaks suggesting non-crystalline SPIONs were present. After 3 h, peaks with significant intensity at 2θ values for magnetite and maghemite are present, but still broad indicating only a portion of SPIONs in the sample were magnetite or maghemite. 6 and 12 h illustrates the narrowing and further increasing intensity of the appropriate peaks where an increasing portion and then all SPIONs are phase pure. This result was published as an *ex situ* method for oxidation of SPIONs [51] and was followed by *in situ* methods that allow for oxidation during initial SPION core synthesis [52].

3.2 Colloidal dispersions

Characterization of other environmental conditions can either be controlled by the solution in which SPIONs are dispersed and the ambient conditions in which a sample is held. For pH and ionicity, the contents of the dispersion need to be carefully controlled. This usually means the preparation of separate solutions at known pH and salt contents and use of these solutions to dilute the SPION dispersion as is discussed in the following section. Control of temperature is carried out by placing the sample in a closed compartment and allowing the temperature to equilibrate before measurement. Temperatures below freezing, 0 °C, and above physiological, 37 to 40 °C, are not a concern for biomedical applications and, thus, will not be discussed in this thesis.

3.2.1 Dynamic light scattering

Dynamic light scattering (DLS) is a light scattering technique for determining the hydrodynamic size, d_{H}, of a nanomaterial dispersed in a liquid medium. In the case of SPIONs, d_{H} in aqueous solution is most important as this is the state necessary for use in biomedical applications. d_{H} is the crucial characteristic that determines circulation time *in vivo* and allows for magnetic imaging over extended periods of time.

Background

The d_{H} of a particle dispersed in a solution is determined by observing their motion over time through the resultant scattering of monochromatic laser light. The motion of a particle in solution due to the thermal energy of the system is called Brownian motion with a given speed of diffusion given by the Stokes-Einstein equation:

$$d_{\mathrm{H}} = \frac{k_B T}{3\pi\eta D_t} \tag{3.4}$$

where d_{H} is the hydrodynamic size, k_B is the Boltzmann constant, T is temperature, η is the solution viscosity, and D_t is the translational diffusion coefficient. Particles of different sizes move at different speeds causing variations in the intensity of scattered light with time. Noting that larger particles move more slowly while smaller particles move more quickly, an autocorrelation function can be solved over time to determine the final d_{H}. More information about this topic can be found in [93, 94].

Sample preparation and data collection

All samples discussed in this thesis were measured with a Zetasizer Nano S (Malvern Instruments Ltd., Worcestershire, UK) and experimental values were calculated with the Zetasizer software (Version 7.11, Malvern Instrumental Inc.) provided with the instrument. This instrument includes a 50 mW He-Ne laser producing light at 633 nm and detected at a backscattered angle of 173° to the incident light. Unless otherwise stated, samples were measured at 20 °C, and each value is an average of 25 measurements.

An example sample preparation method, utilized unless otherwise noted, included diluting 5 µL of SPION dispersion at a concentration of 1 mgFe/mL to 500 µL with deionized water. Mixing and measurement carried out in narrow polycarbonate cuvettes with clear sides set in line with the incident light direction. The Zetasizer software provides feedback in cases of low and high concentration dispersions and measurement following advisement was carried out as needed.

Experimental analysis

The measurement of SPIONs in aqueous solution gives several values with different significance to the actual characteristics of the dispersion and its quality. The DLS software is initially able to calculate the distribution of sizes in a dispersion weighted by the intensity of light associated with each size bin. The method by which particles scatter light depends on their size relative to the wavelength of the incident light. In this case, 633 nm is much larger than the particles causing the scattering. This means that Rayleigh scattering is dominant where the scattered light from a given particle is equal in all directions. Also, the intensity of light is a function of the diameter of the particle doing the scattering with $I \propto d^6$ [93]. Functionally this means that the intensity of a more massive particle is several orders of magnitude more intense than the intensity from a smaller particle when their sizes differ more than a few nm.

The intensity distribution does not provide an accurate picture of the hydrodynamic size distribution for agglomeration of SPIONs. It can be converted to a volume or number distribution with $I \propto d^3$ and $I \propto d$, respectively. The relationship between the three types of weighted distributions is shown in Fig. 3.5 where a mixture of 5 and 50 nm particles in equal quantity are shown to be as such by the number distribution, Fig. 3.5a, but the 5 nm is significantly less represented in the volume distribution, Fig. 3.5b, and even less in the intensity distribution, Fig. 3.5c.

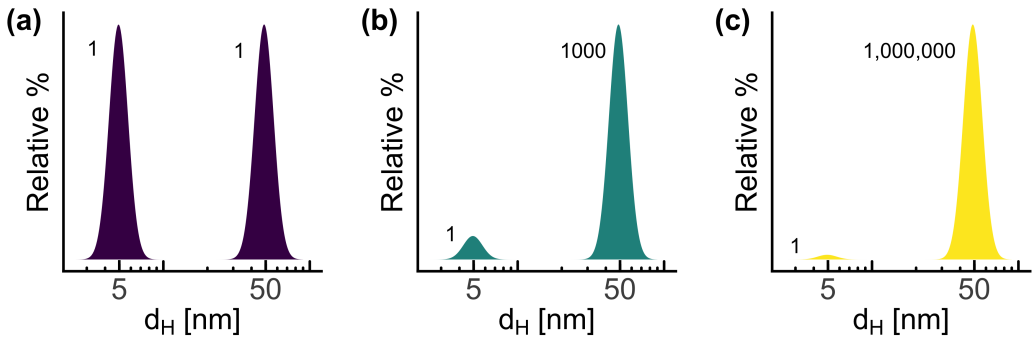

Figure 3.5: Differently weighted size distributions, number (a), volume (b), and intensity(c), of a bimodal mixture of 5 and 50 nm particles present in equal numbers. Adapted from [93].

In the case of this thesis, values presented will either be the number weighted distribution or the Z_{avg}, which is a value generated by the higher level fitting of the scattered intensity over time.

3.2.2 Inductively coupled plasma - optical emission spectrometry

Inductively coupled plasma - optical emission spectrometry (ICP-OES) is a technique used to determine the quantity of each element present in a sample. SPIONs are dispersed in an aqueous medium through a phase transfer process where the total mass that is successfully dispersed depends on the efficiency of that process. Since there are known steps in a phase transfer where mass is lost and others that include concentrating or diluting the dispersion, the final concentration of SPIONs must be determined before further use in biomedical applications is possible.

Background

ICP-OES uses the extremely high-temperature environment of plasma to evaporate a liquid sample, break any ionic bonds present, and excite valence electrons of individual atoms. This promotion of electrons from their ground state to an excited state and subsequent spontaneous relaxation back to ground state results in the emission of a photon characteristic to a given element, as illustrated in Fig. 3.6. The intensity of photons emitted with a specific energy/wavelength is directly proportional to the amount of that element present in the sample.

In the case of SPIONs, it is the mass of iron present that is desired when using ICP-OES. The total mass of iron oxide can be calculated after the fact if the crystal phase is known. For example, magnetite is 72.36% iron and 27.64% oxygen by mass, so the total mass of magnetite, $m_{Fe_3O_4}$, is the mass of iron, m_{Fe}, divided by 0.7236.

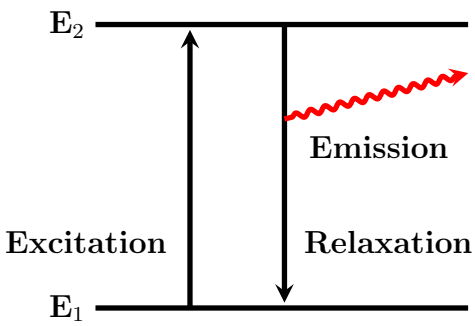

Figure 3.6: Excitation and relaxation of an electron after exposure to the plasma environment of and ICP-OES. Emission of a characteristic photon occurs during the relaxation of an electron from its excited state to ground state.

Sample preparation and data collection

The intensity of characteristics photons from an element is an instrument, and even session, dependent and, as a result, it is necessary to compare samples of unknown concentration to standards of known concentration. These standards are generated by digestion and dilution of a stock iron solution at 1000 ppm (Ultra Scientific, North Kingstown, RI, USA). The amounts of stock solution, concentrated hydrochloric acid, and deionized water necessary to the appropriate range of standard concentrations is shown in Table 3.2. The standard labeled Reagent is used to account for the amount of a given element present in the concentrated hydrochloric acid solution used to digest the stock and unknown solutions.

Table 3.2: Standard solutions of iron for generation of a concentration curve in ICP-OES.

Conc. [ppm]	Stock [µL]	HCl [µL]	DI [mL]
0	0	0	40.000
Reagent	0	800	39.200
0.05	2	800	39.198
0.1	4	800	39.196
0.5	20	800	39.180
1	40	800	39.160
5	200	800	39.000

ICP-OES cannot measure concentrations of unknown or standard solutions that are too high as the intensity floods the detector and give false values. As such, the stock solutions are maintained between 0 to 5 ppm and samples of unknown concentration are diluted down to approximately this same range. Preparation of samples for ICP-OES includes the addition of 5 µL of the unknown samples to a 15 mL Falcon tube. 100 µL of concentrated hydrochloric acid is then added and allowed to sit for approximately 5 min so the acid fully digests the SPIONs and coating. 95, 800, and 4000 µL of deionized water are added in sequence with the appropriate pipettor for the volume. The Falcon tube is then sealed and vortexed to mix the sample thoroughly. Each sample is prepared in triplicate for better statistical significance. The samples are then ready to be analyzed using an ICP-OES (PerkinElmer, Inc., Waltham, MA, USA) with an autosampler that first collects the intensities of the standards and then the unknowns.

It is important to know the correct characteristic photon for a given element that is measured. Each element generates multiple characteristic photons with different relative intensities and generally the photon with the highest relative intensity is chosen for analysis. The ions of iron, characteristics photon wavelengths, λ, and relative intensity are shown in Table 3.3. The most common wavelengths used are 238.2 and 248.3 nm.

Table 3.3: Highest relative intensities of characteristic photons for iron with associated wavelengths and oxidation states.

Rel. %	λ [nm]	Ox. State
100	238.2	Fe(II)
70	239.6	Fe(II)
70	259.9	Fe(II)
100	248.3	Fe(I)
70	373.5	Fe(I)
60	248.8	Fe(I)

Experimental analysis

The ICP-OES used in this work automatically generates the standard curve necessary to determine the concentration of unknown samples. The measured intensity of characteristic photons is linear with concentration allowing for a linear fit to the curve. An example concentration curve and linear fit for the standards in Table 3.2 is shown in Fig. 3.7. The linearity of fit is quantified by the R^2 value and it is generally between 0.999 900 to 0.999 999. R^2 values that do not fall within this range are cause for preparation of new standards as they may have been poorly prepared or not stored properly between uses.

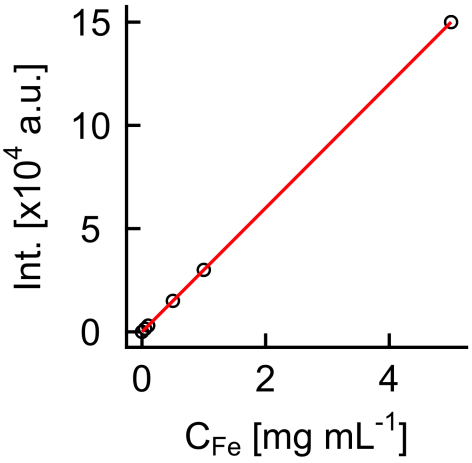

Figure 3.7: Examples standard curve of characteristic photon intensity vs concentration of iron generated by ICP-OES.

The intensities of the unknown samples are then compared to the standard curve, and their concentrations are determined by interpolation of the linear fit. The concentrations of the diluted samples are recorded in ppm which is directly converted to $\mathrm{mg\,mL^{-1}}$ due to the 1000x dilution factor used in sample preparation.

3.3 Magnetic properties

3.3.1 Vibrating sample magnetometry

Vibrating sample magnetometry (VSM) is a technique for collection and observation of the hysteresis behavior of magnetic materials [95, 96]. Properties associated with SPIONs obtained through this method include the saturation magnetization, M_s, and the particle magnetic core size, d_0. The relatively simple sample preparation and instrument setup allows for quick initial assessment of synthesized SPIONs while additional magnetic properties can be extracted when desired with high mass sensitivity.

Background

A material is placed within a constant magnetic field that causes a net magnetic moment within the material. The sample is physically moved in close proximity to a pick-up coil such that a voltage, V, is induced in the coil according the Faraday's law of induction. A sinusoidal oscillation dictates this movement following an angular frequency, ω. Given the induced voltage and known frequency of change, a magnetization of the sample as a function of time, $M(t)$, can be determined according to

$$M(t) = \frac{V}{C \cdot A \cdot \omega \sin(\omega t)} \tag{3.5}$$

where A is the amplitude of oscillation and C is an instrument-specific coupling constant. A given VSM can apply a homogenous magnetic field with upper limits between 1 to 5 T with the instrument used for this work having a maximum of 1.5 T.

Sample preparation and data collection

Preparation of liquid samples for VSM is dependent on the type of liquid in which SPIONs are dispersed. For aqueous phase samples, 100 µL, with a known concentration of iron, is transferred to a 100 µL polycarbonate capsule (Quantum Design Inc., San Diego, CA,

USA). For organic phase samples, 100 to 150 µL, generally without a known concentration, is transferred to a 200 µL gelatin capsule (Quantum Design Inc., San Diego, CA, USA). Both types capsules are sealed with double-sided tape and placed in a short piece of plastic straw for mounting on a VSM sample rod.

The sample rod is attached to the vibrating arm of a Lakeshore 7350 VSM (Lakeshore Cryotronics Inc., Westerville, OH, USA) with the sample centered between the electromagnet and pick-up coil. The instrument cooling and power are then turned on and the arm vibration initialized. Software protocols are utilized to collect hysteresis behavior repeatable magnetic field characteristics and sweep rates. Generally, the VSM is operated below 500 mT for characterization of SPIONs. Specifically for characterization of magnetic core size, three sweeps from positive to negative to positive fields are performed with maximum magnitudes of 2.5 mT, 20 mT, and 200 mT. The three hysteresis loops are then either observed for general shape and initial assessment or exported for further analysis. An example of hysteresis shape of SPIONs is shown in Fig. 3.8a-c.

Experimental analysis

The two fundamental properties that can be determined from analysis of magnetic hysteresis curves for SPIONs is the saturation magnetization, M_s, and magnetic core size, d_0. The saturation magnetization is the highest magnetization of a given sample and is observed when increasing the magnetic field does not increase the magnetization. This occurs at both the positive and negative maximum fields applied and appears as a horizontal line from the saturation point until the highest applied field as shown in 3.8c.

The magnetic core size is obtained from a hysteresis curve through Chantrell fitting [88]. It is assumed that the synthesized SPIONs have a log-normal distribution and the Langevin function can approximate their hysteresis.

$$L(\xi) = \coth(\xi) - \frac{1}{\xi} \tag{3.6}$$

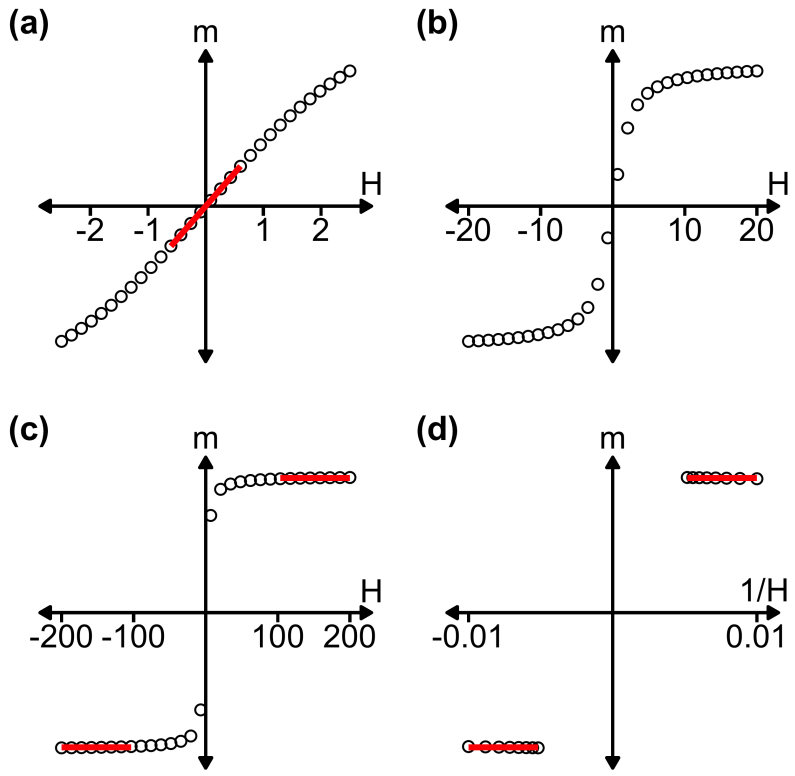

Figure 3.8: Idealized examples of hysteresis behavior for SPIONs between 20 to 30 nm under low (a), mid (b), and high (c) ranges of applied magnetic field. Chantrell size analysis necessitates fitting of portion of each field range as well as the inverse of magnetization for the high field (d). Linear fits shown as red lines.

Chantrell fitting is a series of linear fits of different portions of a hysteresis curve to obtain experimental values that are then used in derived equations for size, d_0, and size distribution, σ. Magnetic core size is defined by

$$d_0 = \left[\frac{18 k_B T}{\pi M_s} \left(\frac{\chi_i}{3M} \frac{1}{H_0} \right)^{1/2} \right]^{1/3} \tag{3.7}$$

where k_B is the Boltzmann constant, T is the temperature, M_s is the saturation magnetization, and χ_i is the initial susceptibility. M is the intercept of the magnetization axis and H_0 is intercept of the field axis for the linear fit of inverse field vs. magnetization. M_s, χ_i, and $1/H_0$ are all experimentally determined from fits. In addition to the size, size distribution of a given sample can be extracted by

$$\sigma = \left[\ln \left(\frac{3\chi_i}{M \frac{1}{H_0}} \right) \right]^{1/2} /3 \tag{3.8}$$

where the same previously determined values are used. It is important to note that the distribution is volume weighted and must be divided by three to be compared to a number-weighted distribution of SPION core size obtained by TEM image analysis.

Poorly dispersed samples, such as SPIONs larger than 20 nm in organic solvents, do not exhibit superparamagnetic behavior due to aggregation and magnetostatic interaction between particles. Chantrell fitting cannot be used to accurately determine size in this case because it depends on fitting the linear and inversely linear regions of a superparamagnetic hysteresis curve. When samples are well dispersed, more often when well coated with a polymer and in aqueous solution, then Chantrell fitting provides sizes and size distributions in close agreement with TEM analysis. This method can be considered more advantageous in some situations because instead of measuring thousands of particles, VSM samples contain several orders of magnitude more particles and can be said to have better statistical significance in size estimations. An example of hysteresis for 25.3 nm SPIONs dispersed in water is shown in Fig. 3.9 where Fig. 3.9d is the expected distribution density at each magnetic core size. Note

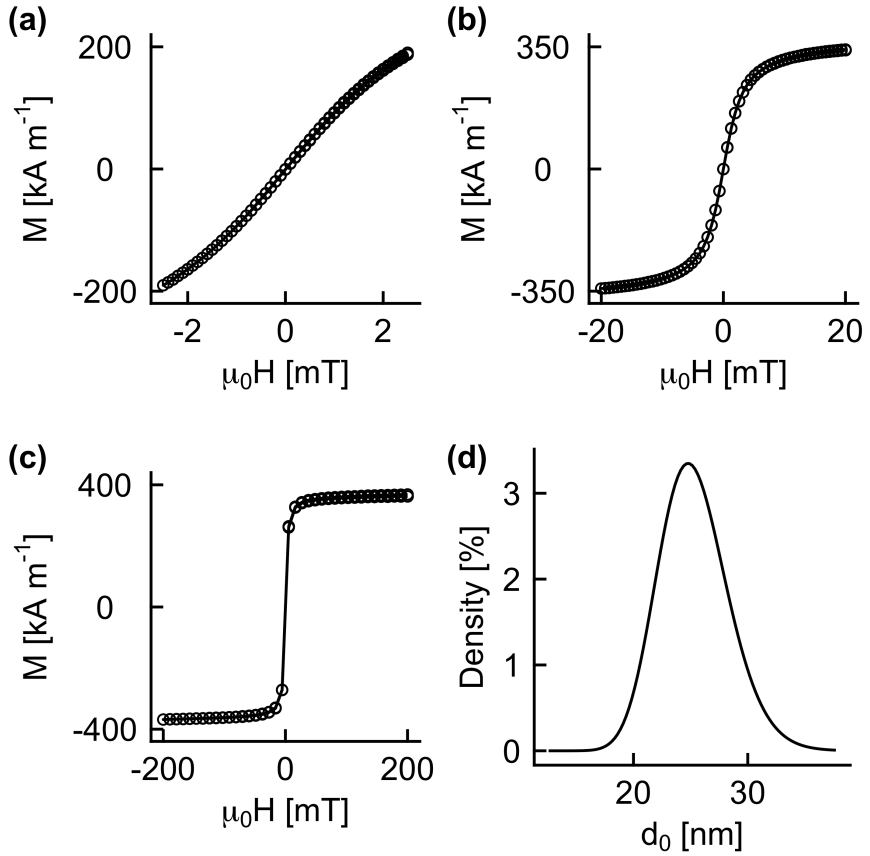

Figure 3.9: Example hysteresis data and size analysis for 25.3 nm SPIONs including low (a), mid (b), and high (c) ranges of applied magnetic field and the expected distribution density (d).

that large and no longer superparamagnetic particles are predicted, but not always directly observed under TEM.

3.3.2 Magnetic particle spectroscopy

The principle behind magnetic particle spectroscopy has been discussed in §1.4. This section covers general sample preparation, instrumentation parameters, and experimental analysis.

Sample preparation and data collection

Sample preparation for MPS included a transfer of liquid to 600 µL centrifuge tubes that fit within the dimensions shown in Fig. 3.10. Liquid samples dispersed in aqueous media consisted of 150 µL diluted to an appropriate concentration confirmed through elemental analysis by ICP-OES. Lyophilized samples were prepared initially with 150 µL to maintain consistency with liquid samples, but any physical changes of dried matrices were noted to ensure all sample mass remained within the pick-up coil region. Samples containing cells were maintained in culture media of no more than 100 µL previously ensuring that media did not produce any MPS signal as well.

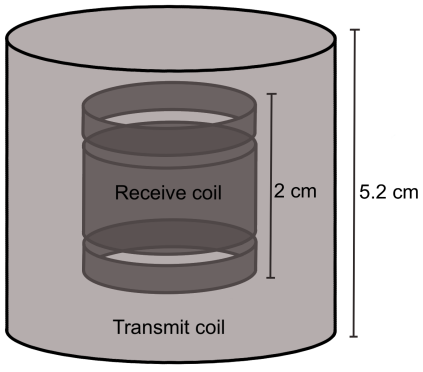

Figure 3.10: Schematic of the transmit and receive coils of the home-built MPS system including dimensions. Adapted from [97].

All MPS samples in this work were analyzed using a home-built system with a drive frequency of 26 kHz and field amplitude of 20 mT. The temperature of the transmit coil

wire increases as current is applied until a steady-state with ambient cooling is achieved. Thus, the instrument was turned on and a current allowed to run through the transmit coil while observing the magnetic field amplitude. In general, a constant amplitude was reached between 30 to 60 min after startup. Instrument operation included the following steps: 1) background signal acquisition without anything between the pick-up coil, 2) gentle placement of sample tube in between coils, 3) sample signal acquisition with between 5 to 30 averages depending on sample concentration.

Experimental analysis

Data collected using the home-built system in this work primarily includes the time-dependent magnetization of SPIONs in an ac magnetic field. Included in the metadata of these files are instrument parameters such as field amplitude, field frequency, instrument-specific sensitivity parameters, and others. Analysis allows for extraction of the field-dependent magnetization, integrated ac hysteresis, and harmonic spectra. The R script utilized for this analysis is shown in full in Appendix F and was adapted from a Mathematica script previously written by Matthew Ferguson [97].

Briefly, the script imports the data previously generated by LabView. One period of the raw signal, from minimum to maximum applied field, is extracted and the point spread function (PSF) generated by subtracting the background signal from the sample signal, Fig. 3.11a. This is converted from a time to field-dependent PSF through a known field frequency, Fig. 3.11b. The PSF can then be integrated to generate the ac hysteresis for SPIONs at the applied field amplitude and frequency, Fig. 3.11c. Lastly, a Fourier transform is performed on the raw signal, and based on instrument parameters, a harmonic spectrum is generated, Fig. 3.11d. Only the odd harmonics are generally considered as their magnitude is several orders of magnitude greater than the even harmonics and have less noise.

A useful characteristic of MPS harmonic and point spread function intensity is its linearity as a function of mass. Fig. 3.12a shows harmonic spectra for samples with 0 to 75 µgFe. It is important to note that samples with minimal mass, the harmonics higher than the 3^{rd} and

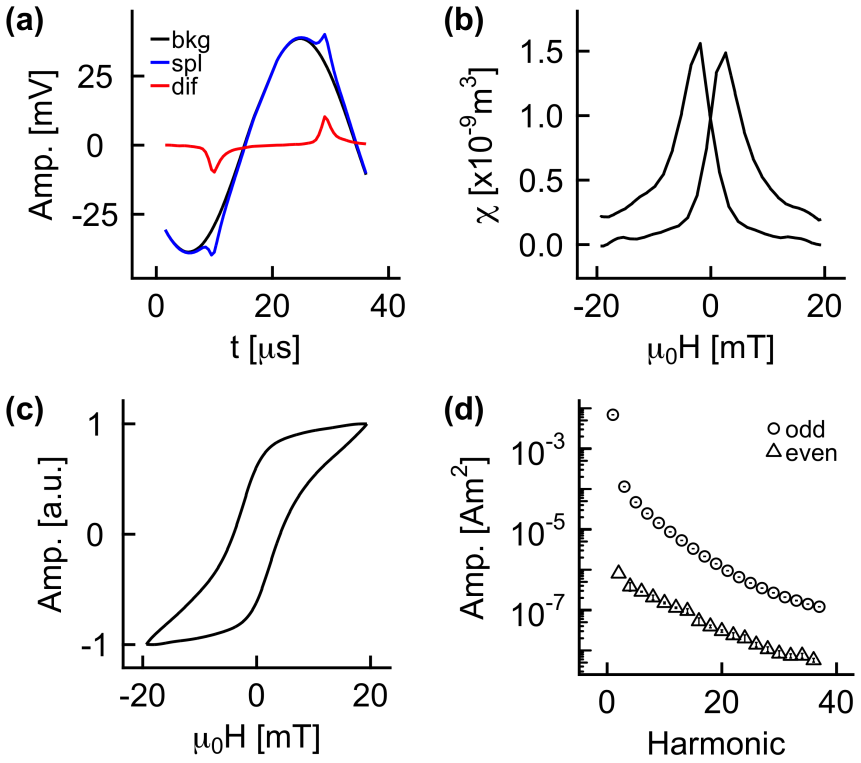

Figure 3.11: Example MPS data for 25.3 nm SPIONs including raw background, signal, and their difference vs time (a), MPS point spread function vs field (b), ac hysteresis vs field integrated from the point spread function (c), and harmonic spectrum (d).

5^{th} become mostly noise. By plotting the amplitude of the 3^{rd} harmonics as a function of iron mass as shown in Fig. 3.12b, the signal linearity is clear.

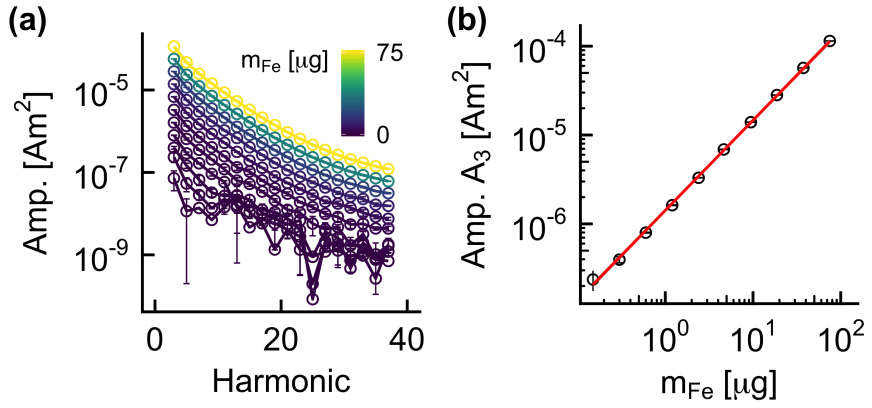

Figure 3.12: MPS harmonic spectra for a dilution series from 5 to 0 mgFe/mL (a) with each decrease in concentration being half of the previous value. 3^{rd} harmonic intensity as a function of concentration (b) illustrating the linearity of MPS harmonic signal down to 1x10^{-3} mgFe/mL.

3.4 Summary of SPION properties

Based on the methods described in this chapter, this section includes a summary of the properties for the SPIONs utilized in §4 and 5. Each of these samples is coated with PMAO-PEG with a 20 kg mol^{-1} PEG loading of 5%. The properties of these particles have been characterized before use by TEM, VSM, MPS, and DLS with the relevant properties summarized in Table 3.4.

Table 3.4: Summary of SPION properties.

d_{TEM} [nm]	σ_{TEM}	d_{VSM} [nm]	σ_{VSM}	M_s [kA m^{-1}]	d_H [nm]	PDI
21.9	0.04	19.9	0.07	367.4	94.1	0.130
25.3	0.08	24.1	0.05	389.1	48.6	0.104
27.8	0.06	25.8	0.09	363.4	97.0	0.121

The SPIONs show increasing core diameters and narrow size distribution parameters of 21.9 (0.04), 25.3 (0.08), and 27.8 (0.06) nm (σ) and are approaching optimal performance in

MPI. There is some overlap in size for these batches as illustrated by the histograms in Fig. 3.13d.

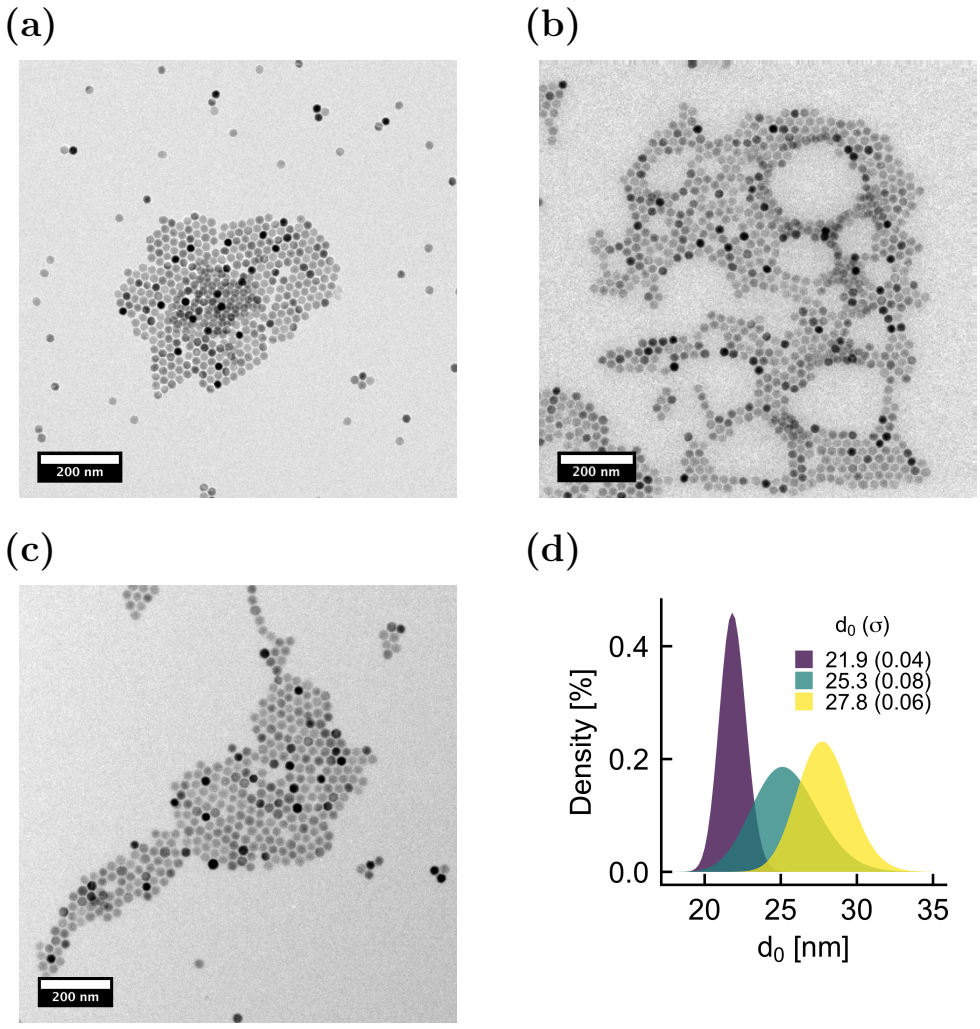

Figure 3.13: Representative TEM images of the three batches of SPIONs used in this work (a-c) and the log-normal size distribution based on size analysis of the images (d).

The core diameters measured by VSM are consistently 1 to 2 nm smaller than those measured by TEM. This is primarily due to the difference between TEM measurement of the physical diameter and VSM measurement of the magnetic core diameter. SPIONs are observed to be single crystals with higher disorder near the particle surface due to incomplete

bonding. This is described as the surface anisotropy that is different from the inner SPION anisotropy. The magnetic core diameter is thus a function of both aspects, but the decreased magnetic alignment at the surface gives an effective magnetic core diameter smaller than the physical diameter.

Deviation from the expected magnetic properties is observed by VSM in Fig. 3.14b-c where the largest core diameter, 27.8 nm, shows a lower saturation magnetization than the next largest, 25.3 nm. This is attributed to increased agglomeration during the phase transfer process resulting in a small fraction of SPIONs in this sample acting as multicore particles with dipolar interactions between cores. This is also observed by the small shoulder in Fig. 3.15a for the 27.8 nm sample.

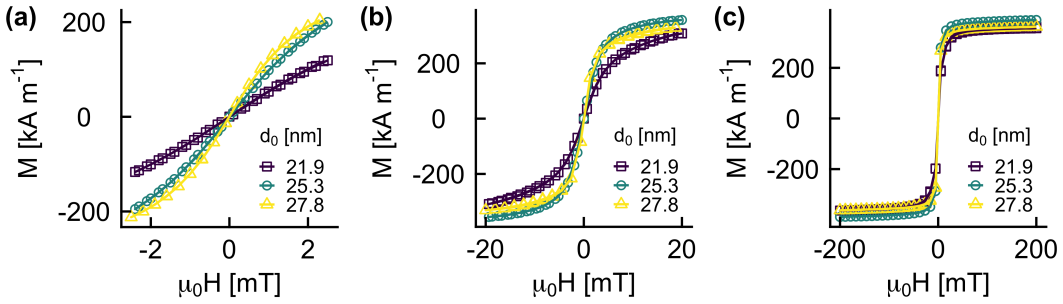

Figure 3.14: VSM data of the three batches of SPIONs used in this work over applied field ranges of −2.5 to 2.5 mT (a), −20 to 20 mT (b), and −200 to 200 mT (c)

These SPIONs show expected MPS properties as core diameter increases including increasing peak intensity, narrowing FWHM, shown in Fig. 3.15a, and slower loss in amplitude with increasing harmonic number, shown in Fig. 3.15c. Note that the FWHM of the point spread function (PSF) is correlated with the rate of amplitude loss with increasing harmonic in the harmonic distribution where narrower FWHM equates to slower amplitude loss.

SPIONs dispersed in aqueous solution vary in hydrodynamic size significantly bringing in a potentially confounding factor of magnetic relaxation when comparing the various sizes. The hydrodynamic volume, V_{H}, is a component of the Brownian relaxation time and will affect the overall magnetic performance of certain size ranges of SPIONs. It is thus important to

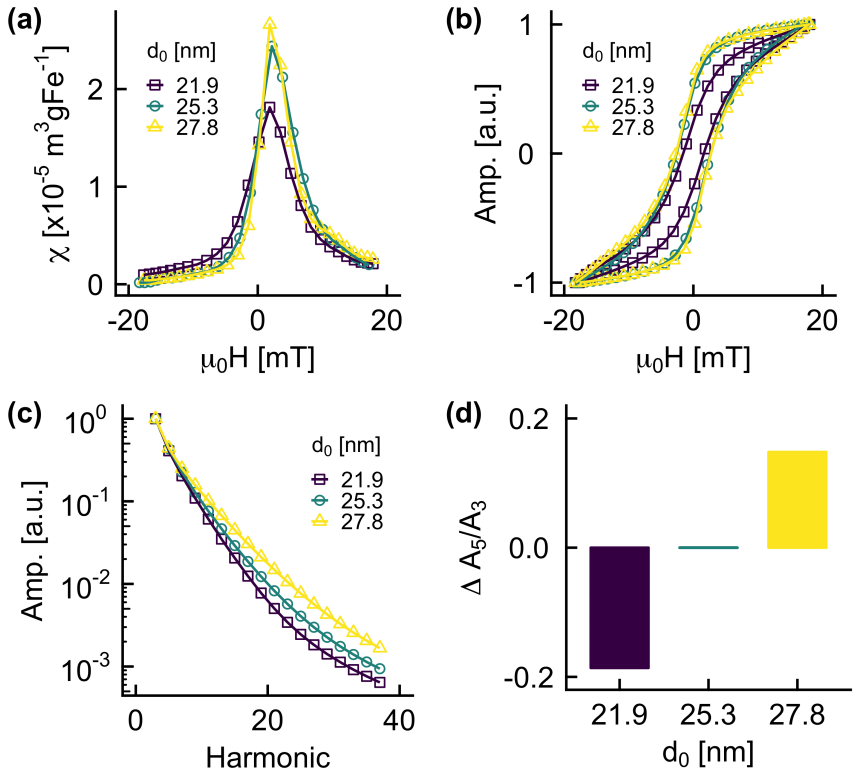

Figure 3.15: MPS data of the three batches of SPIONs used in this work observed over an applied ac magnetic field of −20 to 20 mT. Collected data includes PSF (a), integrated hysteresis curve (b), normalized harmonics (c), and the change in A_5/A_3 for the three batches normalized to 25.3 nm.

keep in mind the variation observed here in interpreting the results of SPIONs in MPS when Brownian relaxation is possible. If there is no change associated with Brownian relaxation, then the variable hydrodynamic size is expected to be a factor with little significance overall.

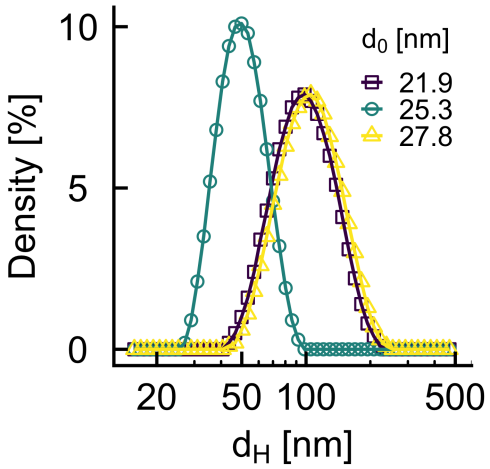

Figure 3.16: Intensity-weighted hydrodynamic size distributions of the three batches of SPIONs used in this work.

3.5 Summary

Many of the techniques described in this chapter are primarily utilized in routine characterization of SPIONs after initial synthesis and transfer from organic to aqueous environments. These techniques, while not novel, are crucial to characterize SPIONs after they have been prepared to determine their usefulness for a given application and the properties that dictate the behavior of SPIONs in more complex environments including their internalization in cells, magnetic behavior after internalization, and fate over time. The next chapter includes an investigation the internalization and fate of SPIONs in those environments.

Chapter 4

UPTAKE AND LOCALIZATION OF MPI OPTIMIZED SPIONS

In the general case of exposing SPIONs to cells, multiple different possible interactions can occur. The first, and least desired for cell loading and targeting applications, is for the SPIONs to be fully non-interacting with the surface of cells. Here, SPIONs would remain outside of cells and additionally would not adhere to the surface of the cells and travel as the cells move. The second possibility is for the SPIONs to remain in the extracellular space surrounding cells, but for there to be a physi- or chemisorption event causes the SPIONs to adhere to the cell surface. The third option for SPIONs when interacting with cells is their complete uptake into the intracellular space and subsequent processing by the cell as is described in the following sections. The full uptake of SPIONs is desirable for cell loading and targeting *in vivo*, but it is crucial to keep in mind the highly variable and potentially damaging environment within the cell and the effects it can have on SPIONs and their performance. This chapter is an exploration of the uptake and eventual state of cells and SPIONs after uptake.

4.1 Cellular pathways for processing of nanomaterials

The mechanisms through which extracellular fluids, molecules, and larger materials are internalized into the cell can be divided primarily into two categories, as illustrated in Fig. 4.1. The first is membrane diffusion through passive and ion channel assisted mechanisms that allow water and ions to enter the cells. This allows the cell to balance the necessary ion content of the cell with the extracellular space. The second mechanism of extracellular material internalization is broadly categorized as endocytosis. Endocytosis can be broken into several subcategories depending on the size of the extracellular material and mechanisms

available to the cell. When the material is tiny, for example $< 10\,\text{nm}$, it is typically observed that pinocytosis occurs. This is the formation of a small vesicle from the plasma membrane surrounding the extracellular component. Pinocytosis is most commonly observed in internalization of proteins and extracellular fluid necessary for internal regulation and communication with surrounding cells.

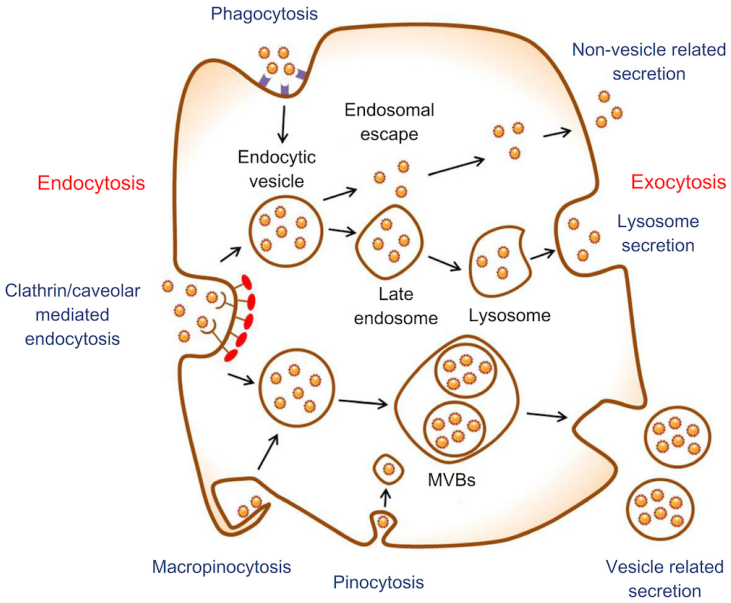

Figure 4.1: Simplified illustration of the possible endo- and exo-cytosis pathways that cells utilize to process extracellular materials. Adopted from [98].

Moving up the range of possible extracellular material size brings clathrin- and caveolae-mediated endocytosis into consideration. Each of these methods depends on receptors present on the exterior surface of the plasma membrane which interact with materials in the extracellular space. Thus this mechanism is regulated by the number of receptors present at a given time on the plasma membrane, the composition of the exposed material surface, and the contents of the extracellular fluid. In the case of nanomaterials such as SPIONs coated with an amphiphilic polymer, it is expected that this receptor-mediated endocytotic pathway dominates and primarily depending on the interaction of the charged species with the necessary receptors.

Continuing up the range of possible sizes, more massive than 500 nm, brings phagocytosis into consideration. This mechanism depends on the presence of specific proteins to interact with extracellular materials and trigger uptake. Only certain cell types contain the necessary plasma membrane proteins, and thus phagocytosis is only considered as an option in phagocytes, of which macrophages are an example. In these cells, much larger materials can be internalized which is why phagocytosis is most often observed as a method for "garbage collection."

SPIONs internalized through endocytosis are initially encapsulated in endosomes, which are vesicles of the cell membrane that have folded in on themselves and hold material that had previously been on the exterior of the cell. Endosomes then move in the interior of the cell through the cytoplasm until they unite with lysosomes or the material goes through the process of endosomal escape. Both circumstances retain the material within the cell's plasma membrane, but endosomal escape allows for the material to interact with other organelles and cell components. If the SPIONs remain within the endosome until they become or unite with other lysosomes, then the cell is then able to process what is degradable through the harsher environment of the lysosome, including higher acidity helping the cell process and digest the internalized material.

If the material that has been internalized can be utilized by the cell, then its constituent components are processed through the lysosome. The remainder is then expelled through the primary exocytosis mechanism known as lysosome secretion. This process involves the merging of lysosome and plasma membrane and subsequent release of lysosome contents to the extracellular environment.

4.2 Quantification of SPION uptake

In situations where SPIONs and cells are placed in close proximity, the likely event, based on previous studies of cell and SPION interactions, is the uptake of the SPIONs into the intracellular space. It is thus essential to determine if the SPIONs utilized in this work, coated with $20\,\mathrm{kg\,mol^{-1}}$ PMAO-PEG loaded at 5%, follow the expected behavior. The first

method to determine if SPIONs are interacting or non-interacting with cells of various types is through quantification of iron content present inside cells after exposure to SPIONs. There is a small quantity of iron naturally present in cells, but this amount is not detectable through the ICP method used here and considered especially negligible in contrast to the amount of iron from SPIONs.

4.2.1 Methods

Human epithelial fibrosarcoma cells (HT-1080) and mouse macrophage leukemia virus-induced cells (RAW 264.7) were maintained in Eagles Minimum Essential Medium (EMEM) and Dulbecco's Modified Eagle's Medium (DMEM), respectively, supplemented with 10% FBS and 1% Penicillin-Streptomycin at 37 °C and 5% CO_2 atmosphere. Cells were passaged at least three times after thawing before use and never allowed to reach higher than 90% confluence. SPIONs were made sterile through 200 µm filtration and diluted down to the necessary concentration using 1X PBS. SPION solutions were then diluted to final exposure concentration with EMEM or DMEM, depending on cell type, supplemented with 1% Penicillin-Streptomycin. All solutions had equal total volumes and an equal percentage of media; only SPION concentration was varied.

Cells were seeded in 6-well plates at $5x10^4$ HT-1080cells/well and $3x10^5$ RAWcells/well in 3 mL of media and maintained for 24 h at 37 °C and 5% CO_2 atmosphere. Media was then aspirated off, cells washed with 1X PBS, and media containing SPIONs added to the wells. Exposure was allowed to continue for 8, 16, and 24 h, then the supernatant was aspirated off, cells washed with 1X PBS, and cells digested with 1 mL concentrated HCl. Three wells of cells were not digested and instead collected with 0.25% Trypsin-EDTA for cell counting. 800 µL of digested solution was transferred to a 15 mL Falcon Tube and diluted to 5 mL with deionized water for ICP analysis. Operation of the ICP instrumentation was carried out as described in §3.2.2.

4.2.2 Results & discussion

Here a total iron content is determined for each sample over increasing SPION exposure concentrations and using previously determined cell counts, an iron content per cell is obtained. Fig. 4.2a is representative of the trend observed in SPION uptake with increasing exposure concentration and observed at 8, 16, and 24 h. As may be expected, there is an increase in the iron content of each cell as the concentration of SPIONs in the extracellular space is increased. This is physically explained by the increased accumulation on the surface of cells allowing for more SPIONs to be encapsulated in the cell membrane with each endocytosis event. These results are in agreement with previously reported uptake quantification of SPIONs in similar cell types [99].

The exception here is the 24 h time point which does not show the highest iron content. This is attributed to the exocytosis processes which cells utilize to expel foreign materials, in this case the SPIONs with a polymer coating. The amount of time it take for exocytosis to occur is nanoparticle and coating dependent, but 24 h is sufficient for cells to process and expel a portion of SPIONs. [98] While the amount is lower than at 8 h and 16 h, an important characteristic of SPIONs utilized in cell tracking and long-term *in vivo* studies is their presence and detectability. This method does not indicate their physical state or imaging and therapeutic performance but does allow for continued exploration of these properties knowing that over these periods the SPIONs are actively and strongly interacting with cells, be it through internalization or adherence to the cellular membrane.

In addition to observing the iron content over time, identical concentrations of SPIONs were exposed to both HT-1080 epithelial and RAW 264.7 macrophage cells over 24 h. Fig. 4.2b show the different iron content for each cell type. Macrophage cells utilize phagocytosis allowing for higher rates of uptake through the "engulfing" of foreign materials. Just as increasing the concentration in the extracellular space allows for increased SPION count in each encapsulation, increasing the size of the encapsulation space increases the total number of SPIONs that can be internalized. At each concentration exposed to each cell type,

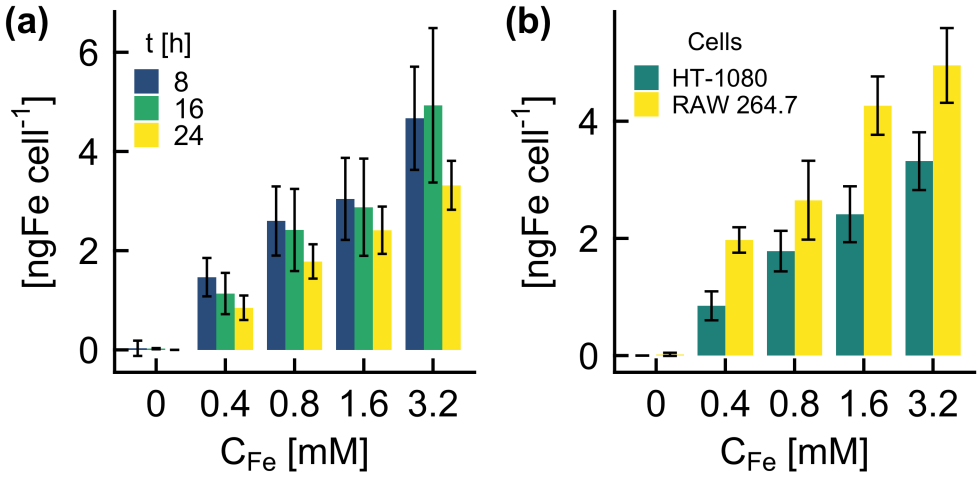

Figure 4.2: Quantification of SPION uptake in HT-1080 cells over 24 h period (a) illustrating a drop in iron content per cell with increasing time. Quantification of SPION uptake after 24 h in two cell types (b) showing the expected increase in uptake for macrophage cells.

there is a sizable increase of 100% at lower concentrations to approximately 25% at higher concentrations.

4.3 Cytotoxicity of SPIONs

SPION cytotoxicity is often considered a non-factor in the majority of studies due to the known biocompatibility of iron oxide, as discussed in §1.2. While this holds in most cases [100, 101], it is possible for iron to be toxic factor *in vivo* through its over-accumulation and subsequent iron overload. *In vitro* it is possible to cause toxicity with iron oxide through extreme concentrations in the extracellular space, but there may be other factors contributing to the toxicity. One example factor may be the presence of carcinogenic chemicals not fully removed during the removal of core synthesis by-products.

There are a variety of methods through which nanoparticles can interact with and damage cells including, but not limited to, uptake-independent effects, uptake-dependent effects, reactive oxygen species generation, proliferation limiting, and cell function impairment. It is not trivial to narrow down which plays the most significant role as diverse situations result in different aspects being dominant.

In addition, many studies fail to consider the variations in dosimetry that occur over the range of nano- to micron-scaled materials due to their kinetic behavior in solution. This premise focuses on the idea that particles move through cell culture media during *in vitro* assessments in varying ways. As a result of this kinetic consideration, the actual dose that reaches the cell is a factor of the nanoparticle's diffusivity, susceptibility to gravity, and tendency to agglomerate [102].

The focus of this work is not to determine the sole source of toxicity in situations where it exists. Instead, these factors are discussed because it is crucial to keep in mind that the toxicity of a specific material is unknown until directly tested. As such, the SPIONs utilized in this work must also be tested at a variety of concentrations and over an appropriate time frame to determine if damage to cells occurs.

Here, the resazurin assay has been utilized to determine cell viability and toxicity of SPIONs. This assay determines the oxidative-reductive behavior of cells as an indicator of mitochondrial activity. Cells that are viable process the blue indicator dye, resazurin (7-hydroxy-3H-phenoxazin-3-one 10-oxide), and generate its reduced pink form, resorufin, that can then be measured by either absorbance or fluorescence methods.

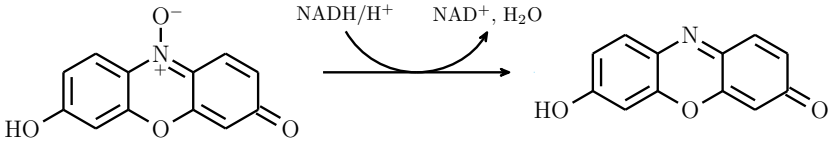

Figure 4.3: Reduction process of resazurin to resofurin in the presence of NADH within living and metabolically functioning cells.

4.3.1 Methods

Human epithelial fibrosarcoma cells (HT-1080) were maintained in Eagles Minimum Essential Medium (EMEM) supplemented with 10% FBS and 1% Penicillin-Streptomycin at 37 °C and 5% CO_2 atmosphere. Cells were passaged at least three times after thawing before use and never allowed to reach higher than 90% confluence. SPIONs were made sterile through

200 µm filtration and diluted down to the necessary concentration using 1X PBS. SPION solutions were then diluted to final exposure concentration with EMEM or DMEM, depending on cell type, supplemented with 1% Penicillin-Streptomycin. All solutions had equal total volumes and an equal percentage of media; only SPION concentration was varied.

Cells were seeded in 96-well plates at $1x10^4$ HT-1080cells/well 100 µL of media and maintained for 24 h at 37 °C and 5% CO_2 atmosphere. Media was then aspirated off, cells washed with 1X PBS, and media containing SPIONs added to the wells. A subset of wells each received either only media or media containing 2% Triton X-100. Exposure was allowed to continue for 24 h, then the supernatant was aspirated off, cells washed with 1X PBS, the supernatant was again aspirated off, and 100 uL of 0.0036% Resazurin working solution was added to each well. Absorbance was read from each well using a Multiskan Spectrum UV/Visible Microplate Reader (Thermo Labsystems, Beverly, MA, USA) at wavelengths of 570 and 600 nm.

4.3.2 Results & discussion

Cell viability of HT-1080 cells has been observed over iron concentrations similar to those used in the uptake quantification of SPIONs by ICP. Here it is noted that with each increase in concentration, there is a small decrease in the % of cells remaining viable, though even at the highest iron concentration exposed to cells there is only a 3.9% decrease from the zero iron case. These results are both significantly improved or comparable to previous cytotoxicity studies of SPIONs prepared by the Krishnan group [57, 103]. In those previous studies, the polymer coating and overall process of transferring SPIONs from hydrophobic to aqueous phase were in continuous development. It is a positive sign for the future use of the PMAO-PEG coated SPIONs that minimal toxicity was observed for this stage of coating and purification process development.

It is further noted that other potential factors may contribute to the toxicity of SPIONs, be it minimal or otherwise, that must be kept in consideration. SPIONs dispersed in hydrophobic environments are exposed to many different long-chain organics and solvents including oleic

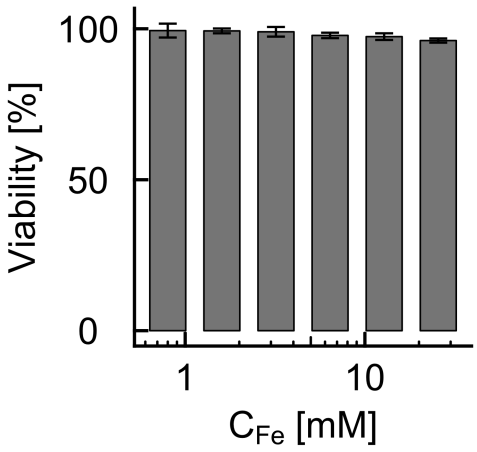

Figure 4.4: Observation of cell viability of HT-1080 epithelial cells after 24 h for increasing concentrations of PMAO-PEG coated SPIONs showing minimal drop in overall cell health.

acid, 1-octadecene, hexanes, chloroform, acetone, ethyl acetate, and by-products of the initial thermal decomposition reaction. It is possible for trace amounts of these chemicals to remain physisorbed to the SPION surface or coating and be carried through to the final use case such as injection or exposure to cells. Purification steps are implemented throughout the preparation of these samples, but dilution and exchange of the dispersion medium is not a guarantee of complete removal. In particular, SPIONs are dispersed and sonicated for significant periods in chloroform which is a known carcinogen and could actively affect the toxicity of a given sample if purification is not successful in removing enough of the chloroform. This is further complicated by the known azeotrope between chloroform and water that is not possible to remove unless the SPIONs are thoroughly dried.

4.4 Intracellular localization of SPIONs

The first characteristic of internalized SPIONs that must be determined is where are the particles going once entering the cell, i.e. their localization. A visual determination of SPION localization in the cell informs what type of environment the SPIONs encounter.

SPIONs coated with PMAO-PEG and incubated with HT-1080 epithelial cancer cells are

readily observed to show uptake by quantification of iron content in cells, as discussed in §4.2, but their localization exterior or interior to the cell is unknown by that method. SPIONs experience significantly different environments based on their localization. For example, media and serum containing salts, sugars, and proteins exist outside of the cell membrane, and these components are capable of adhering to the nanoparticles thereby potentially changing their hydrodynamic size or causing electrostatic agglomeration that may prevent uptake.

In addition, it is essential to take note of localization as it relates to the effect on the cell. SPIONs in some regions of the cell make toxicity, either acute or chronic, more likely. One prime example is the introduction of iron oxide to the nucleus of a cell increases the likelihood of reactive oxygen species generation and damage to DNA. If internalized SPIONs are not found within the nucleus, it is still important to note their localization as different organelles and the cytoplasm can have different environmental conditions. These conditions include increased viscosity of cytoplasm and organelles and increased acidity (decreased pH) within lysosomes, [104, 105] to name a brief subset of possible conditions.

There are four expected locations in which SPIONs could be found including the nucleus, cytoplasm, within an organelle, or adhered to the exterior of the cell membrane. In order to accurately determine the localization of SPIONs, confocal fluorescence imaging and TEM is used as it provides high contrast under appropriate sample preparation and are the ideal techniques for imaging over the expected length scales of SPIONs (<30 nm) up to the size of a whole cells (5 to 20 µm).

4.4.1 Methods

Human epithelial fibrosarcoma cells (HT-1080) were maintained in Eagle's Minimum Essential Medium (EMEM) supplemented with 10% FBS and 1% Penicillin-Streptomycin at 37 °C and 5% CO_2 atmosphere. Cells were passaged at least three times after thawing before use and never allowed to reach higher than 90% confluence. SPIONs were made sterile through 200 µm filtration and diluted down to the necessary concentration using 1X PBS. SPION solutions were then diluted to final exposure concentration with EMEM supplemented with

1% Penicillin-Streptomycin. All solutions had equal total volumes and an equal percentage of media; only SPION concentration was varied.

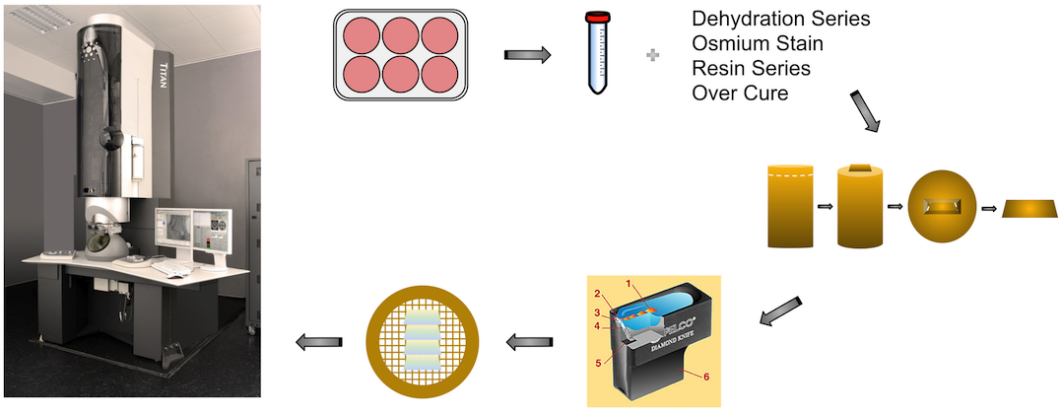

Figure 4.5: Diagram illustrating the process of exposing SPIONs to cells and the necessary steps to prepare cells for imaging with TEM.

Cells were seeded in 6-well plates at $3x10^6$ cells/well in 3 mL of media. Three wells were seeded with coverslips on the bottom to allow for confocal microscopy. After 24 h of incubation, the supernatant was aspirated and serum-free media added. Two drops of NucBlue^{TM}Live Cell Stain (Life Technologies, Carlsbad, CA) was added to each well and allowed to sit at room temperature for 20 min. This mix was then aspirated away, cells gently washed with 1X PBS, and coverslips were transferred to a new well plate with 4% paraformaldehyde that had been prepared fresh in 1X PBS and 0.03 M sodium cacodylate. This was incubated at room temperature for 20 min while protected from light. The paraformaldehyde solution was aspirated, coverslips washed with 1X PBS twice, and mounted to microscope slides using one drop of Vectashield mounting medium. Samples were stored for no more than one day at 4 °C before imaging. Confocal fluorescence microscopy was performed using a Leica DMi8 (Leica Microsystems GmbH, Germany) inverted confocal microscope with 405, 488, and 532 nm excitation lasers and PMTs corresponding to fluorophore emission peaks to avoid spectral overlap and allow simultaneous multicolor imaging.

To the remaining culture plate wells, without coverslips initially, 0.25% Trypsin-EDTA

was added. Released cells were collected in centrifuge tubes, pelleted, and supernatant was removed. 100 µL of pre-melted 1% low-melting-point agarose was added and the mixture spun down at 1500 rcf for 10 min. Tubes were cooled at 4 °C for 30 min to solidify the agarose solution, after which 1 mL of Karnovsky's fixative [106] was added. Samples were kept at 10 °C and shaken at 300 rpm overnight. Samples were then further fixed in 1% osmium tetroxide for 3 h.

Agarose blocks were trimmed to remove excess not containing cells, noted by a lack of blackened color from osmium fixation. The cell-containing agarose blocks were then dehydrated in the following ratios of acetone and Milli-Q water; 50:50, 70:30, 90:10, 100:0, 100:0. Samples were embedded in PolyBed/Araldite resin following a dilution series of increasing resin and decreasing acetone at each step in the following ratios; 33:67, 50:50, 67:33, 100:0, the preparation of which is shown in Table 4.1. The resin was cured at approximately 65 °C for five days.

Table 4.1: PolyBed/Araldite resin dilutions preparation.

		mass [g]			
Resin %	Component	33%	50%	67%	100%
29.41	PolyBed	1.76	2.65	3.53	5.29
16.18	Araldite	0.97	1.46	1.94	2.91
52.94	DDSA	3.18	4.76	6.35	9.53
1.47	DMP-30	0.09	0.13	0.18	0.26
	Acetone	12.00	9.00	6.00	0.00

Resin blocks were trimmed with razor blades until cells were near the resin block surface and ultra-thin sectioned using a diamond knife to 70 nm thick. Serial-sections were collected where possible, with the priority being consistent section coloring. Sections were adhered to 75 mesh Cu TEM grids coated with pure carbon and Formvar. This process is highlighted, with resin block shape and sectioning diagram, in Fig. 4.5. Samples were post-stained with 2.5% Uranyl Acetate Alternative (Ted Pella, Inc.; Gadolinium Triacetate) for 8 min and 0.1% Lead Citrate solution for 90 s. Bright-field imaging was carried out using a JEOL JEM-3000SFF

(JEOL USA, Inc., Peabody, MA) transmission electron microscope with a direct electron detector and operated at 300 kV. Scanning probe imaging was carried out using an FEI Titan 80-300^{TM} with a Gatan CCD camera and operated at 300 kV.

4.4.2 Results & discussion

Particle localization in imaging is first established through confocal microscopy of cells with fluorescent dye-labeled nuclei and exposed to dye-conjugated SPIONs. Z-projections of cells both non-exposed, Fig. 4.6a, and exposed, Fig. 4.6b, to SPIONs illustrate significant uptake. Individual organelles are visible as locally concentrated higher intensity fluorescent signal as compared to surrounding cellular material suggesting the highest concentration of labeled SPIONs are present in those vesicles. It is not possible to discern the vesicle type through these images and magnifications nor do they unambiguously confirm internalization vs. adherence to the cell surface of SPIONs.

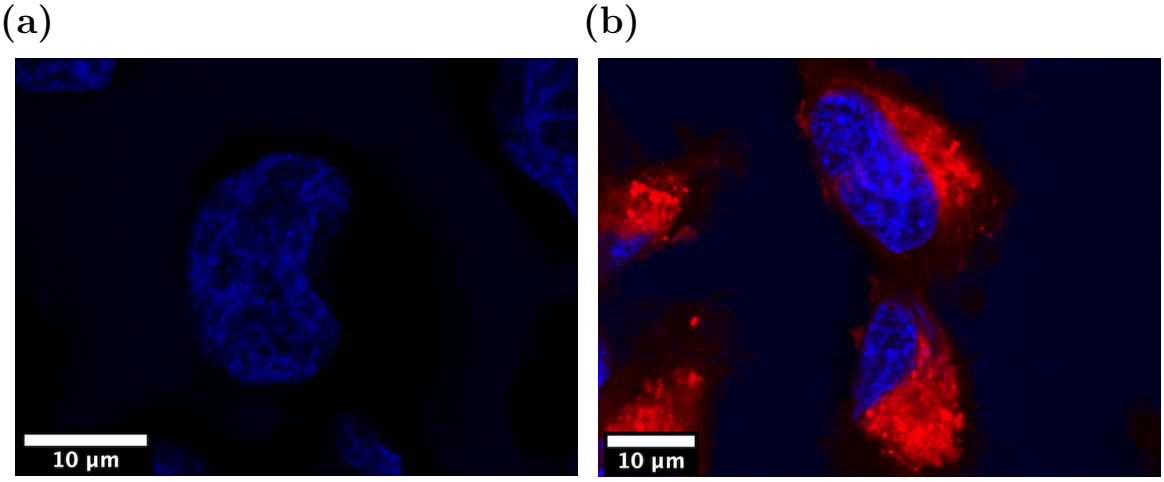

Figure 4.6: SPIONs internalization observed before (a) and after (b) cell exposure by confocal fluorescence microscopy.

Thus, further investigation has been carried out through the use of TEM imaging of cells both without, Fig. 4.7a and with, Fig. 4.7b, internalized SPIONs. These images confirm localization of SPIONs only within cytoplasmic vesicles. Higher magnification imaging further

confirms that these vesicles are endosomes, shown in Fig. 4.7c, and lysosomes, shown in 4.7d, as is expected for uptake of SPIONs through endocytosis pathways and in agreement with prior observations of PEG-coated SPIONs [22].

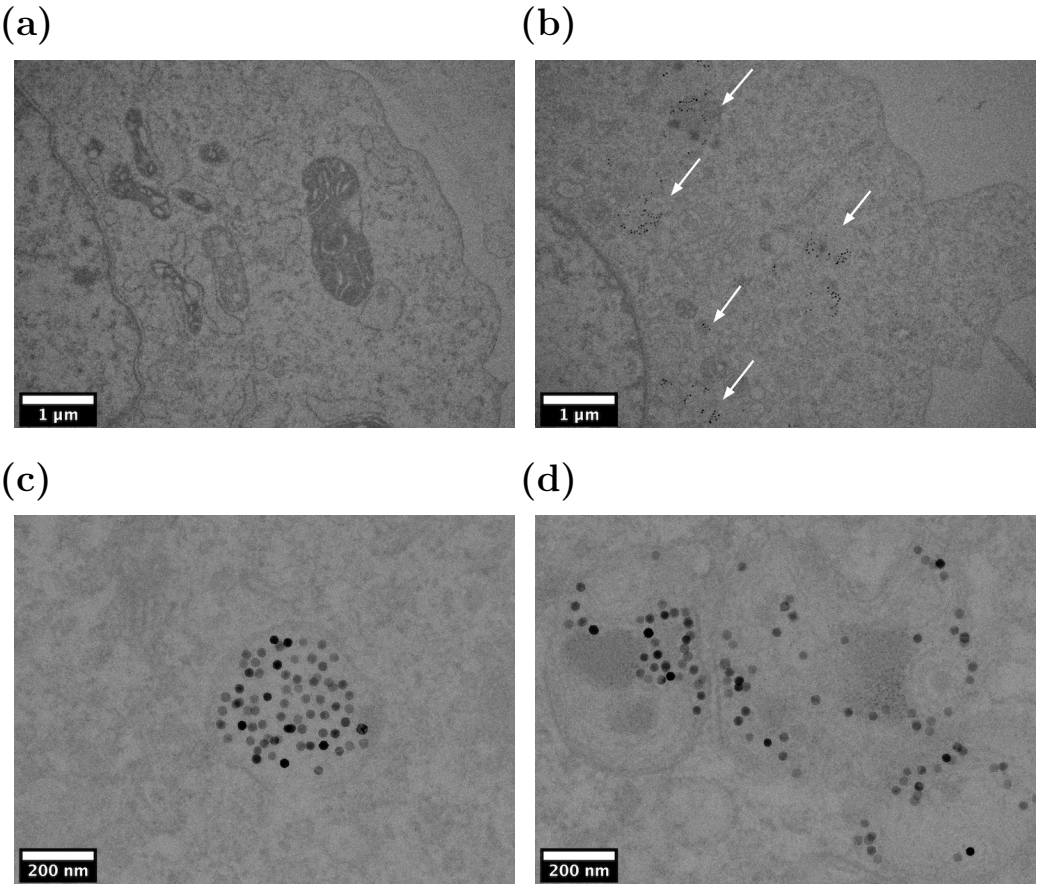

Figure 4.7: SPION internalization observed before (a) and after (b) cell exposure by TEM. Higher magnification reveals the specific cytoplasmic vesicles of internalization as endosomes (c) and lysosomes (d).

Further confirmation of localization in endosomes and lysosomes is accomplished through scanning transmission electron microscopy (STEM). In this method, higher atomic number elements appear brighter, as is apparent in the representative images in Fig. 4.8. Here the localization of SPIONs after internalization within endosomes and lysosomes is made more clear by the higher contrast of the cytoplasmic vesicle membranes and onion-like structure of

lysosomes, noted as the structure highlighted by white arrows. There are primary regions including the extracellular space that is outside of the cell, the cytoplasm encompassing everything between the cell membrane and nucleus, and the nucleus. Important factors to note are that SPIONs are never found within the nucleus, suggesting that damage to DNA over the observed periods does not occur. The second factor is that there are seldom SPIONs found outside of either endosomes or lysosomes and the less than 0.1% that have been found free in the cytoplasm can potentially be attributed to artifacts from sample preparation. The process of ultramicrotomy includes cutting resin embedded samples with a diamond knife, and it is known that the cutting process can dislodge and drag nanomaterials from their original locations. This is likely to have happened here due to the proximity of all particles to endosomes and lysosomes with SPIONs in them. After taking note of the localization of the SPIONs after internalization, the next step is to utilize higher resolution imaging to observe their exact physical state.

4.5 Intracellular physical stability of SPIONs

The first potential factor that can lead to a variation of magnetic performance in imaging and therapeutics of SPIONs is a physical change to the core size, size distribution, or crystalline phase. The size of the SPION plays a significant role in magnetic performance due to the changing saturation magnetization, anisotropy, and other less important, but still present magnetic properties. As the size changes, the mechanism through which the nanoparticle aligns with an applied magnetic field changes with the Brownian and Néel contributions shifting more towards Brownian dominated relaxation as the size increases. The contributions of each mechanism have different associated relaxation times, and a change in contribution affects overall performance. These aspects of SPION magnetic response is discussed in more detail in Chapter 5. The cell is known to have mechanisms for processing foreign materials, one of which includes a decreased pH to between 4.5 and 5.0 within the lysosome [32]. This environment is expected and has been shown previously, in *ex vitro* conditions, to change the magnetic response of SPIONs over time, but it should be noted that it took 48 to 96 h before

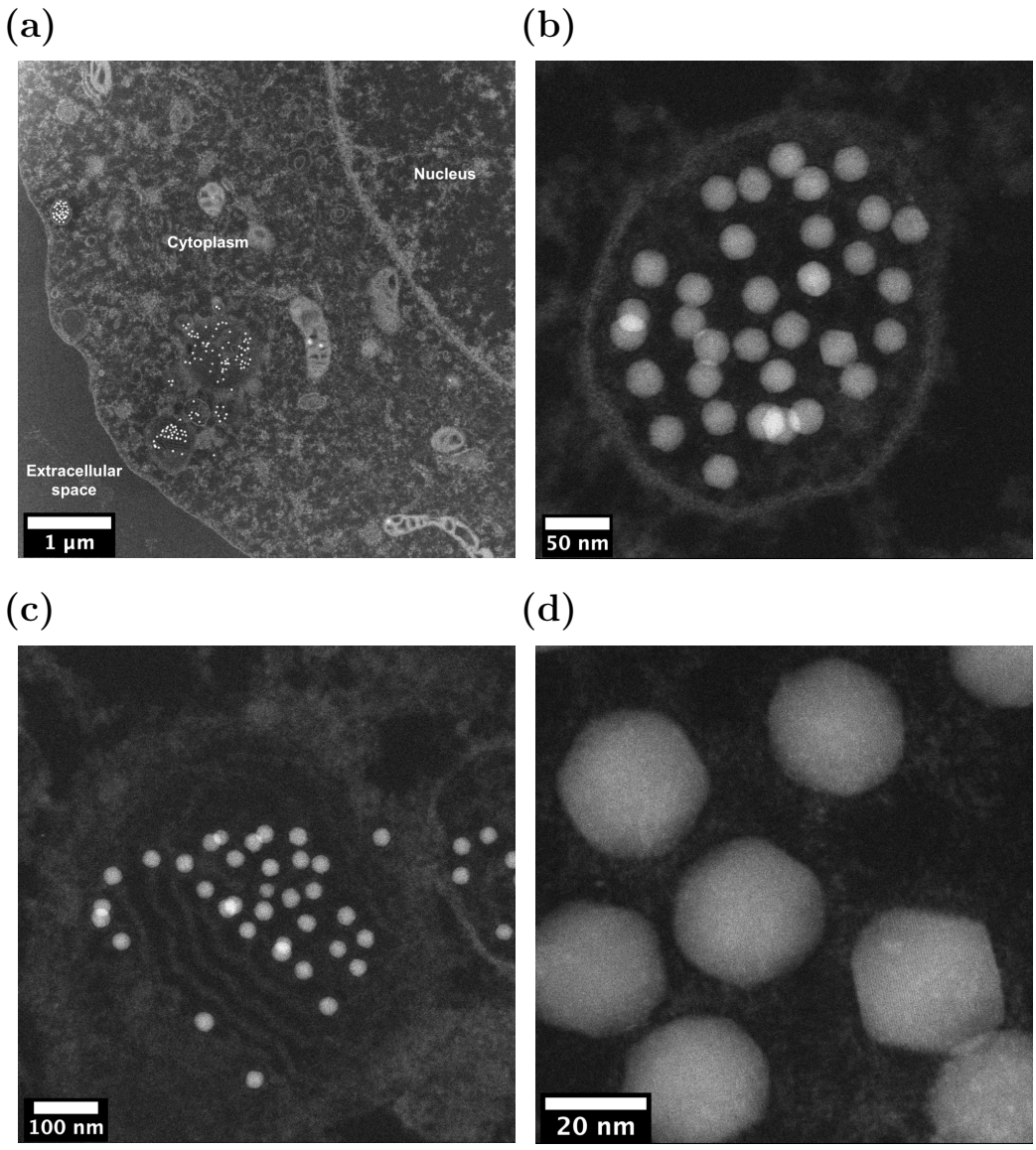

Figure 4.8: STEM images of intracellular SPIONs their localization within the cytoplasm (a), endosomes (b), and lysosomes (c) after 24 h. SPIONs within endosomes and lysosomes remain faceted and lattice fringes are observed (d).

a significant change was observed [107].

The last physical component of SPIONs that could affect the magnetic response is the crystalline phase of the particles. If the same lysosomal environment were to affect the crystalline phase through oxidation or reduction of the iron atoms in SPIONs, then it is possible that a mixed phase or single crystal and weak signal generating phase could be generated. Thus it is important to keep track of the crystallinity of SPIONs after internalization to determine if any significant change has occurred that can explain the observed change in magnetic performance.

4.5.1 Results & discussion

Keeping the potential changes in mind, low and high-resolution TEM imaging is used to examine the size, size distribution, and crystallinity of the SPIONs. They are further examined using image analysis of relatively low-magnification images with no change in either size and their associated size distribution observed. The results, as shown in Fig. 4.9, illustrate a minimal variation between the two cases, as-synthesized and internalized, which can be attributed to experimental factors such as the difference in the number of available SPIONs in images to be counted. The counts, n, for the two cases differ by 340 with $n_{\text{as-syn.}}$ and $n_{\text{internalized}}$ being 889 and 549, respectively. As was discussed in Sect. 3.1.1, the number of counted SPIONs varies the final determined size and size distribution with more error introduced in the low count case.

In regards to crystallinity, a representative image of internalized SPIONs imaged at higher resolution from the highlighted vesicle in Fig. 4.7c is shown in Fig. 4.10a. This image was collected in scanning imaging mode previously aligned to have sub-angstrom resolution which was confirmed through imaging of a gold standard (not shown here). It is clear from the regularly spaced lattice fringes observed in Fig. 4.10a that the SPION remains crystalline over the vast majority of the particle. It is possible to extract the intensity of the fringes and space in between them by collecting the pixel intensity in a direction perpendicular to the fringes. It is further possible to get significant signal-to-noise improvement by averaging the

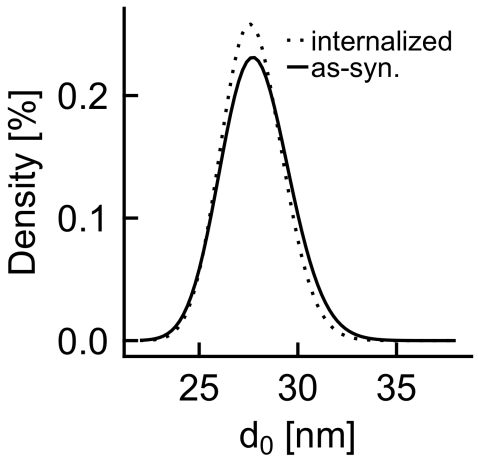

Figure 4.9: Comparison of as-synthesized SPION size and size distribution to that of intracellular SPIONs illustrating negligible changes in both characteristics.

intensity in the direction parallel to the fringes.

This analysis is performed in ImageJ by highlighting a rectangular region and generating an intensity profile as in shown in Fig. 4.10b. From this profile, the lattice spacing of this crystal plane is extracted by finding the distance between adjacent peaks and valleys in the profile and found to be 0.503 ± 0.031 nm. This value is 3.7% from the 0.485 nm lattice spacing corresponding to the (111) crystal plane of magnetite. This is well within the standard deviation of the measurement of lattice spacing by this image analysis method which is mainly limited by the number of pixels available.

Another factor is the TEM calibration which is generally accurate to within 5 to 10% of the measured value due to small voltage fluctuations during even a single TEM session. Also, there are no other iron oxide lattice spacings, including each of the four possible phases, within 30% difference of the measured value. Those lattice spacings for magnetite and maghemite are shown in Tab. 3.1. This supports the conclusion that the SPIONs are still magnetite after internalization for 24 h in cells.

It is expected that SPIONs imaged so that the (111) crystal plane is aligned with the electron beam would show further symmetry than only parallel lattice fringes in one direction.

It is possible that the resolution in this case is limited by the 70 nm of carbon containing resin and other cell contents that may be present. In a pristine sample with a well aligned microscope, individual atoms of the visible lattice fringes would also be visible, but as they are not, the resolution limitation is supported.

The crystallinity shown in this image reinforces the conclusion that no physical change has occurred within these SPIONs over the time scale of interest. It is possible that significantly longer internalization times could result in physical changes to the SPIONs, but the time scales of less than 24 h are considered significant for MPI and even more likely are time scales less than 1 to 2 h for most *in vivo* imaging.

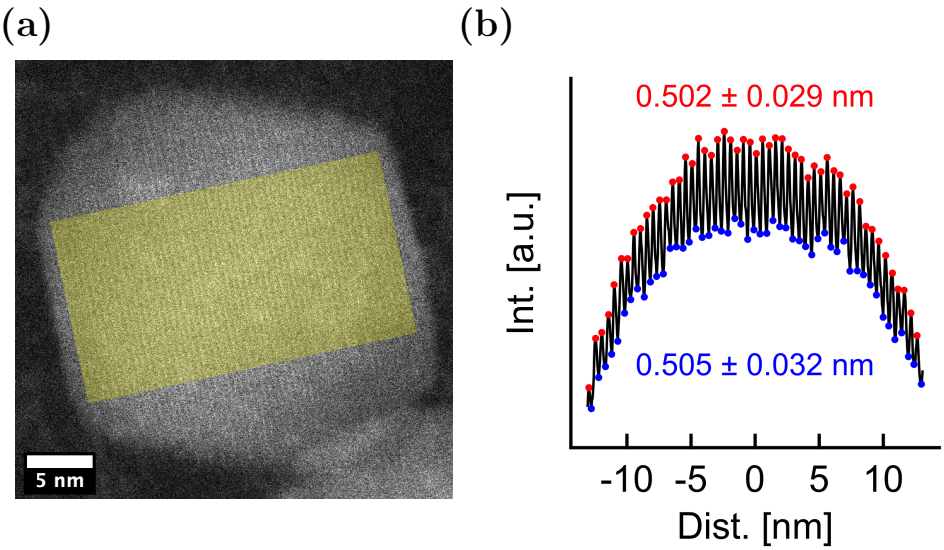

Figure 4.10: Representative image of SPIONs following 24 h internalization and illustrating retention of good crystallinity through clear lattice fringes (a). An intensity profile generated (b) from the highlighted region. Peaks (red) and valleys (blue) in intensity are used to obtain an average 0.503 nm spacing corresponding to the (111) plane of magnetite.

An important characteristic of SPIONs that has not yet been addressed is the presence and stability of the polymer coating in the intracellular environment. Fig. 4.11b shows two SPIONs that have been internalized in vesicles in the cytoplasm, as shown in Fig. 4.11a, and further show coronas surrounding the SPION cores that are attributed to the polymer coating.

It was previously not possible to view the polymer shell due to limited contrast of the primarily carbon-containing polymer against the embedding resin and Formvar supporting films on which ultra-thin sections were collected. By collecting samples on TEM grids containing only a thin carbon coating, it is possible to view the polymer coating by STEM imaging with Z-contrast.

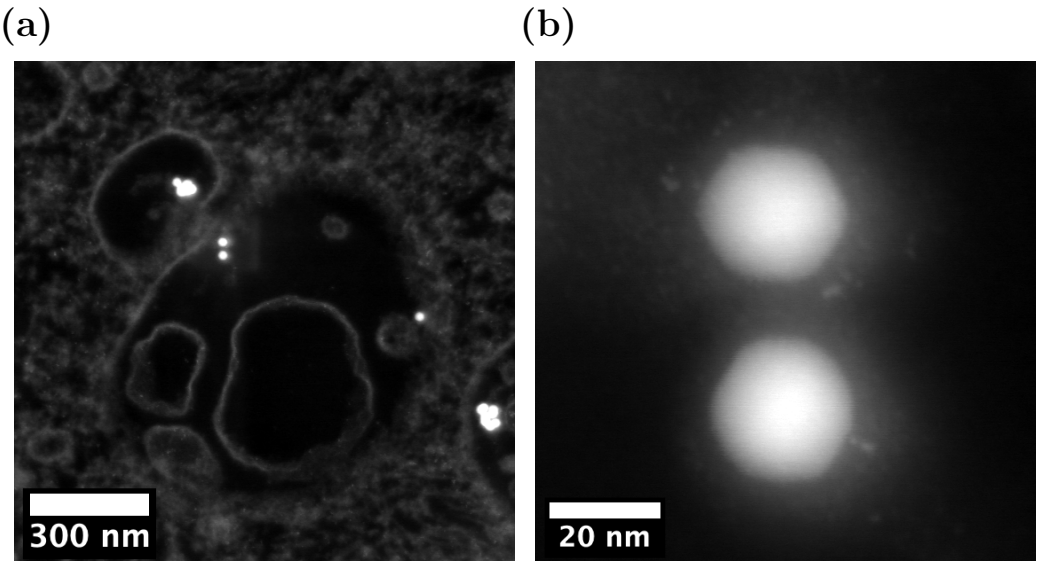

Figure 4.11: Image of SPIONs following 24 h internalization (a). Higher magnification image of two SPIONs from (a) showing a corona around the SPION cores attributed to the polymer coating (b).

It can be inferred from the stability of the SPION core size, size distribution, and crystal phase that the coating is still present 24 h after internalization, but this direct imaging of the polymer coating further supports that conclusion. This is shown by the continued crystallinity of the SPION cores which are known to readily react under acidic conditions, such as those found in the lysosome. Two possible cases of degradation were expected and not observed for intracellular SPIONs. The first is a decrease in core size from acidic digestion from the outer shell towards the center with iron and oxygen migrating away as the process occurs. With no decrease in core size and size distribution, this potential degradation mechanism is excluded. The second possibility is a selective digestion of iron or oxygen in the outer

layers of SPIONs in which an amorphous layer would be generated and would give SPIONs a core-shell structured appearance. This was also not observed for any of the SPIONs imaged after internalization.

With size and crystallinity retained, SPIONs are expected to be fully coated at this stage of internalization and time period as the PMAO-PEG coating is able to prevent transit of acidic species to the iron oxide surface. Additional evidence for the continued presence of the polymer coating is the fluorescence observed by confocal microscopy within cells and shown in Fig. 4.6. The fluorescent Cy5.5 molecule had previously been conjugated to the PMAO-PEG coating in which it would be expected that a loss of coating would also be indicated by a loss of fluorescence signal. Over the 24 h internalization period, fluorescence is retained and thus the conjugated polymer coating should still be in place on the SPIONs.

4.6 Summary

Based on the results and discussion here, it is clear that SPIONs optimized as imaging tracers for MPI and coated to allow for uptake in cells are stable over a desirable time frame. A majority of imaging after injection in clinical setting is expected to be carried out prior to 24 h and the physical stability of SPIONs, including the core and coating, used here is excellent over that span. As the physical characteristics observable by nanoscale imaging techniques is not the only potential route to variations in magnetic performance, it is thus important to experimentally characterize SPION performance *in vitro*. The next chapter incorporates this idea as well as a theoretical approach to understanding *in vitro* magnetic dynamics.

Chapter 5

INTRACELLULAR MAGNETIC DYNAMICS OF SPIONS

While the information gathered through uptake quantification, cytotoxicity measurement, and direct observation of SPION state after internalization did not indicate any negative impacts on both the cells and SPIONs, this does not give any indication of their magnetic properties in these environments. Factors outside of physical size and atomic arrangements contribute to the response of SPIONS to an ac magnetic field and must be fully characterized. This chapter is an exploration of the directly observed magnetic performance of SPIONs within live cells and a determination of the contributions to variations in the performance.

5.1 Intracellular SPION performance

Seeing no change in the physical characteristics and observing no apparent reasons why magnetic characteristics would be affected, it is important to directly observe the MPS performance of SPIONs after internalization in cells. One of the three batches of SPIONs has thus been exposed to cells under the same conditions as were used to observe internalization through microscopic imaging. Here a noticeable change in magnetic performance is observed for internalized SPIONs measured in live epithelial cancer cells. This change from freely dispersed in water to internalized in cells, shown in Fig. 5.1a, is observed as a decrease in the FWHM of the PSF. The PSFs for both aqueous dispersions and intracellular SPIONs are normalized between zero and one due to the significant difference in the raw signal intensity and an inability to normalize by concentration based on MPS sample preparation methods. As the intracellular sample contains a significantly lower mass of iron, it is much closer to the noise floor of the home-built MPS system, and thus the signal-to-noise ratio for this sample is low. Also, the MPS system has a fundamental sampling rate limit that prevents a more

rapid acquisition of signal as the ac magnetic field is varied.

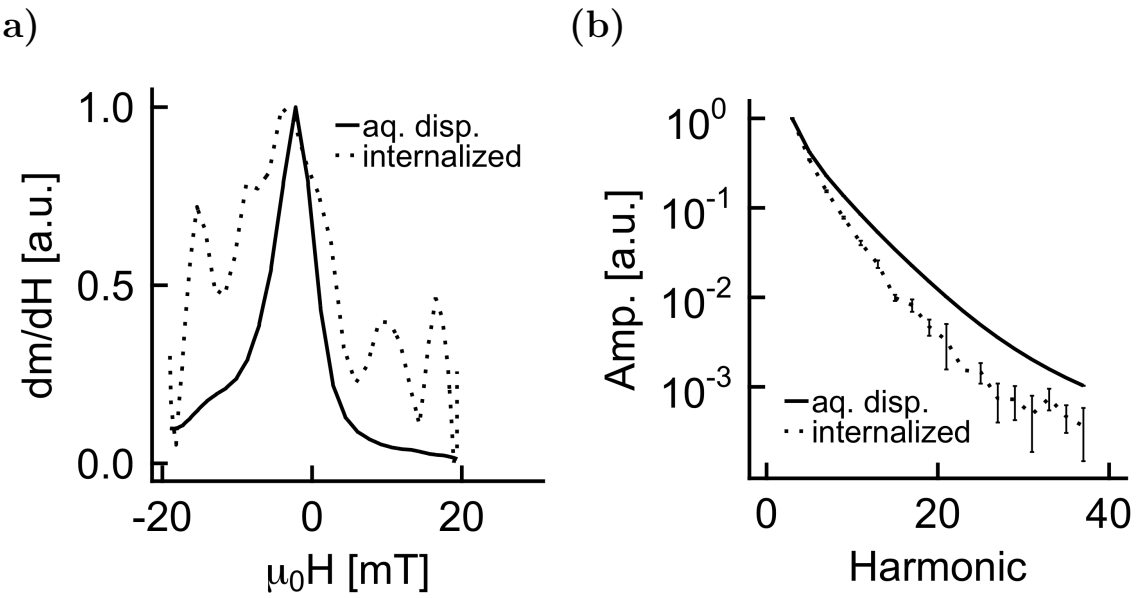

Figure 5.1: Comparison of pre- and post-internalization MPS PSF (a) and harmonic spectra (b). The PSF shows a notable though noise filled increase in FWHM while the harmonic spectra shows a clear decrease in harmonic amplitude with associated 20% drop in A_5/A_3.

Based on the limitations of the PSF as a comparison method, the harmonics spectra and the relevant extracted values will be utilized in the characterization of low iron mass situations, namely intracellular samples. The harmonic spectrum is generated from a signal over 64 periods of signal acquisition as compared to two periods for the PSF, allowing for increased signal-to-noise. Fig. 5.1b is the harmonic spectra for the same data acquisition series above. There is a noted decrease in the amplitude of harmonics higher than the 1^{st} and a 20 % decrease in A_5/A_3.

These results are representative of the 25.3 nm SPIONs utilized in this work and is the baseline of reduced intracellular magnetic performance. The remainder of this chapter outlines the theory of SPION magnetic response to an ac magnetic field, the experimental and theoretical methods to observe changing magnetic response, and associated results elucidating

the source of decreased intracellular performance.

5.2 Modeling Magnetic SPION Dynamics

The following is a brief overview of the Monte Carlo simulation implementation used in this work. It was written in the Python programming language by Carolyn Shasha of the Krishnan Lab at the University of Washington. The code used in this work has been validated previously against experimental conditions [108], and further details can be found in Carolyn's doctoral thesis [55].

5.2.1 Theory

The magnetization of SPIONs is typically described in terms of the Langevin function, shown in Eq. 5.1,

$$L(\xi) = \coth(\xi) - \frac{1}{\xi} \tag{5.1}$$

where $\xi = \frac{\mu_0 \mathrm{mH}}{k_B T}$. The Langevin function description of magnetization requires the assumptions that the system is in equilibrium and that the magnetic dipoles of each SPION have an isotropic distribution, neglecting realistic anisotropy. In terms of the rate of magnetization change, M, a system is considered in equilibrium only if the relaxation time, τ, is much smaller than the rate of change in magnetization, i.e. for an alternating field with frequency, f, $\tau \ll 1/f$. Typical operation parameters in MPI/MPS include alternating magnetic field frequencies $\geq$ 15 kHz and for the work here equal to 26 kHz.

Under this frequency range and higher, SPION alignment with an applied alternating field is opposed by internal anisotropy in addition to thermal fluctuations. These aspects can be accurately described and simulated in coupled stochastic rotation equations. The internal magnetic moment of a SPION, m_i, rotates within the volume of a magnetic nanoparticle

described by the Landau-Lifshitz-Gilbert (LLG) equation: [109, 110]

$$\frac{\mathrm{d}\hat{\mathbf{m}}}{\mathrm{d}t} = \frac{\gamma}{1+\alpha^2}(\mathbf{H} + \alpha\hat{\mathbf{m}} \times \mathbf{H}) \times \hat{\mathbf{m}} \tag{5.2}$$

with the electron gyromagnetic ratio, γ, damping parameter, α, and effective field, $\mathbf{H}$. The Brownian rotation of a SPION can be described in terms of the torque [111], $\boldsymbol{\theta}$, acting on the particle's easy axis, $\hat{\mathbf{n}}$, and dependent on the fluid viscosity, η, and hydrodynamic volume, V_h. These factors are combined to generate a second differential equation:

$$\frac{\mathrm{d}\hat{\mathbf{n}}}{\mathrm{d}t} = \frac{\boldsymbol{\theta}}{6\eta V_\mathrm{h}} \times \hat{\mathbf{n}} \tag{5.3}$$

Equations 5.2 and 5.3 describe the relaxation dynamics of a magnetic nanoparticle for the generalized case of non-zero fields and non-equilibrium conditions. The dominating contributions to these equations are enveloped within $\mathbf{H}$ and $\boldsymbol{\theta}$, which are both calculated from the Helmholtz free energy, $F = U - TS$, of the systems. This energy is a factor of the internal energy, U, temperature, T, and entropy, S. Entropy is considered negligible for monodisperse SPIONs and thus can be made equal to 0. Through the Helmholtz energy term, effective field and torque are written as:

$$\mathbf{H} = \frac{\partial F}{\partial \hat{\mathbf{m}}} \approx \frac{\partial U}{\partial \hat{\mathbf{m}}} \tag{5.4}$$

and

$$\boldsymbol{\theta} = \frac{\partial F}{\partial \hat{\mathbf{n}}} \times \hat{\mathbf{n}} \approx \frac{\partial U}{\partial \hat{\mathbf{n}}} \times \hat{\mathbf{n}} \tag{5.5}$$

The internal energy, U, incorporates several different contributions:

$$U = \varepsilon_{Zee} + \varepsilon_{pp-IA} + \varepsilon_{ai} \tag{5.6}$$

with the Zeeman energy term,

$$\varepsilon_{Zee} = -\mu\mu_0 \hat{\mathbf{m}} \cdot \mathbf{H}_{\text{app}} \tag{5.7}$$

the magnetostatic interaction energy term,

$$\varepsilon_{pp-IA} = -\sum_i \frac{\mu\mu_i\mu_0}{4\pi r_i^3} \left(3\left(\hat{\mathbf{m}} \cdot \hat{\mathbf{r}}_i\right)\left(\hat{\mathbf{m}}_i \cdot \hat{\mathbf{r}}_i\right) - \hat{\mathbf{m}} \cdot \hat{\mathbf{m}}_i\right) \tag{5.8}$$

and the anisotropy energy term

$$\varepsilon_{ai} = -KV_{\text{c}}(\hat{\mathbf{m}} \cdot \hat{\mathbf{n}})^2 \tag{5.9}$$

where r_i is the interparticle separation distance, K is the anisotropy and the magnetic moments, μ and μ_i, are equal to the saturation magnetization, M_{s}, times the SPION core volume, V_{c}. These equations describe the deterministic behavior of SPIONs, but do not include the contribution of random thermal fluctuations over time. A new term must be added to Eq. 5.10 and 5.11 to account for these fluctuations, giving [112]:

$$\mathbf{H} = \frac{\partial F}{\partial \hat{\mathbf{m}}} \approx \frac{\partial U}{\partial \hat{\mathbf{m}}} + \text{H}_{\text{th}} \tag{5.10}$$

and

$$\boldsymbol{\theta} = \frac{\partial F}{\partial \hat{\mathbf{n}}} \times \hat{\mathbf{n}} \approx \frac{\partial U}{\partial \hat{\mathbf{n}}} \times \hat{\mathbf{n}} + \theta_{\text{th}} \tag{5.11}$$

The derivation of these thermal fluctuations won't be included here. Briefly, the magnitude of H_{th} and θ_{th} primarily depend on SPIONs characteristics and temperature. To solve these coupled stochastic differential equations, stochastic calculus and numerical integration must be employed. Each of these equations describes the behavior of a single particle, but this process must be repeated many times to determine an aggregate magnetization value over time and as a function of applied field. Following these theoretical models, SPION behavior

under varying and controlled conditions can be simulated.

5.2.2 Methods

The range of possible arguments and relevant values used in the Monte Carlo simulations in this work are shown in Table 5.1. The values were chosen based on limitations in available process run time, experimental values, and appropriate theoretical considerations.

Table 5.1: Monte Carlo simulation parameters including those used in all simulations and when specifically controlling for relaxation mechanism with referenced sections of this chapter.

Arg.	Description, Units	Value	
N	time steps	10,000	
T	temperature, K	300	
H	field amplitude, mT	20	
f	field frequency, kHz	26	
d_0	core size, nm	21.9, 25.3, and 27.8	
σ	size distribution	0.04, 0.08, and 0.07	
K	anisotropy, $\mathrm{J\,m^{-3}}$	5200, 4700, and 4500	
		Brownian-only (Sect 5.3)	Néel-only (Sect 5.7)
η	viscosity, $\mathrm{Pa \cdot s}$	$8.89\text{x}10^{-4}$ to $3.19\text{x}10^{-2}$	N/A
d_{coat}	coating size, nm	100	N/A
C	concentration, particles/box	$1\text{x}10^{15}$	$6.46\text{x}10^{20}$ to $6.46\text{x}10^{23}$
N	number of particles	2,500	64
X	number of repetitions	400	313
	particle position	random	fixed-distance

5.3 Effect of viscosity on SPION response

As no change in core size, size distribution, and crystallinity of internalized SPIONs is observed, other potential mechanisms must be explored to explain the deterioration in intracellular SPION magnetic performance. Here, the relaxation mechanisms used by SPIONs in an ac magnetic field, Brownian and Néel, are considered. Each mechanism is a factor in the alignment of the SPIONs magnetic moment to an applied field and their respective

contributions dictate the final performance. Brownian relaxation is considered here first as the viscosity of the solution and the hydrodynamic size are both of potentially affected by intracellular environments.

SPION hydrodynamic size has been characterized as a function of temperature in commonly used buffer solution, 1X PBS, and cell culture media, DMEM, as shown in Fig. 5.2. Here, it is observed that SPIONs do not show any agglomeration tendencies as a function of increasing temperature. As SPIONs are incubated with cells at 37 °C, this suggests that hydrodynamic size is constant up until at least the point of endocytosis. As was discussed in the previous chapter, the SPION coating is expected to remain intact after internalization. The assumption is made that the inert nature of the PEG terminal group of the amphiphilic polymer coating will prevent non-specific and undesired reactions from occurring in the cell environment. Based on this, the coating and resulting hydrodynamic size will remain constant after internalization and only changing viscosity within cells will be examined further.

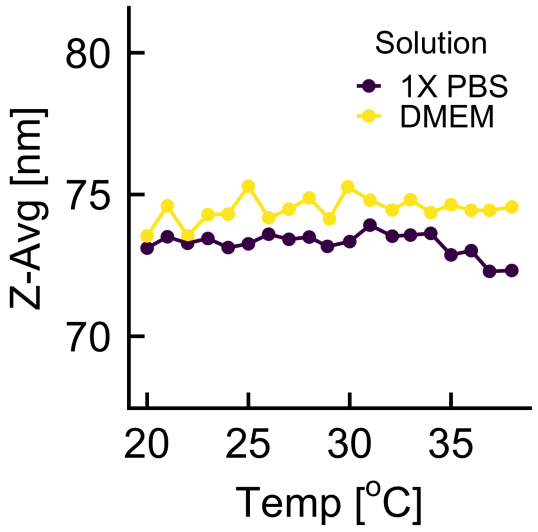

Figure 5.2: Observed consistency in hydrodynamic size of SPIONs, in two expected solutions, with increasing temperature over a range between room equivalent and biologically relevant.

5.3.1 Methods

To determine if a significant reduction in Brownian contribution has occurred, control solutions of varying viscosity were prepared from glycerol and deionized water following the values shown in Table 5.2. 135 µL of each of these solutions, ranging from 0 to 85 glycerol w/w%, were mixed 15 µL of SPION dispersions, and mixed thoroughly. The final mixture w/w% was accounted for in the dilution with SPION dispersion. The mixtures were then immediately characterized by MPS. Direct comparison to exact viscosity values used in Monte Carlo simulations is accomplished through conversion of final glycerol w/w% to viscosity through experimentally derived numerical formulae. [113, 114, 115]

Table 5.2: Glycerol solution preparation.

Initial w/w%	$m_{glycerol}$ [g]	m_{H_2O} [g]	Mixture w/w%	η [Pa · s]
0	0.00	5.00	0.0	$8.9\text{x}10^{-4}$
2	0.10	4.90	1.8	$9.3\text{x}10^{-4}$
4	0.20	4.80	3.6	$9.7\text{x}10^{-4}$
8	0.40	4.60	7.2	$1.1\text{x}10^{-3}$
16	0.80	4.20	14.4	$1.3\text{x}10^{-3}$
32	1.60	3.40	28.8	$2.0\text{x}10^{-3}$
64	3.20	2.80	57.6	$7.6\text{x}10^{-3}$
75	3.75	1.25	67.5	$1.5\text{x}10^{-2}$
85	4.25	0.75	76.5	$3.2\text{x}10^{-2}$

One important consideration in the data collection for samples of SPIONs and glycerol-water mixtures is the temperature at which the sample is maintained. The viscosity of the glycerol-water mixtures is dependent on temperature, as shown in Fig. 5.3, to a significant enough extent that a 5 to 10 °C increase in temperature will shift total viscosity from one to two orders of magnitude. The home-built MPS system used in this work generates heat as current is passed through its metal coils, but this heat can be minimized by reducing the ac magnetic field pulse rate. This has been done for these measurements to maintain room temperature throughout data collection.

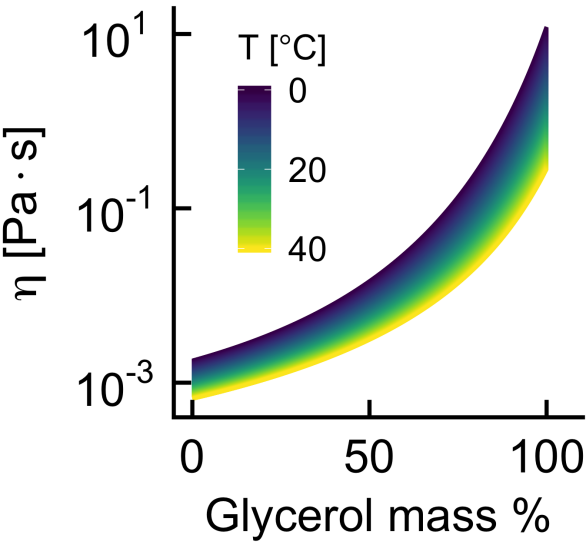

Figure 5.3: Viscosity of glycerol-water mixtures as a function of glycerol mass % and temperature of the solution.

5.3.2 Results & discussion

Fig. 5.4 clearly shows no change in the magnetic response of SPIONs as a function of increasing viscosity, for average core diameters between 20 and 30 nm. This is consistent with the non-linear Monte Carlo simulated response of SPIONs under identical conditions and suggests that over the range of viscosities studied, up to more than one order of magnitude greater than would be expected within a cell, there is no shift in magnetic response. In particular, the lack of decrease in A_5/A_3 suggests that the Brownian contribution to the magnetic performance of SPIONs with diameters between 20 and 30 nm is minimal. As viscosity only affects the Brownian component of magnetic relaxation, then it can further be said that viscosity should be ruled out as a contributing factor in the observed changes in the magnetic response of SPIONs with core diameters near those used in this work and internalized in cells.

The hysteresis curves of the minimum and maximum chosen viscosities are observed to reinforce further the conclusion that viscosity does not play a role in the magnetic response of

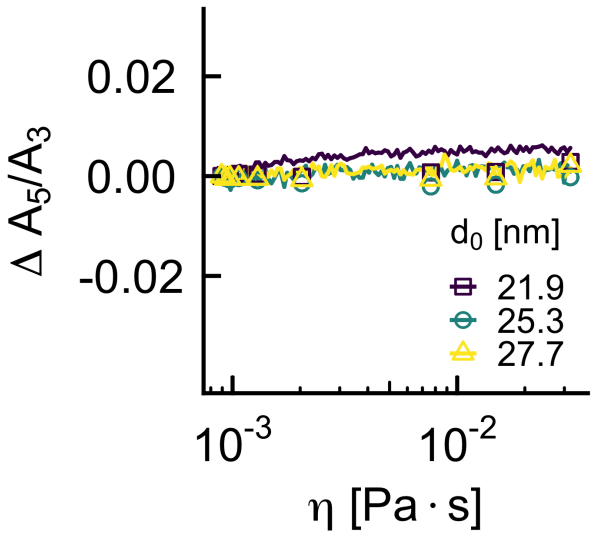

Figure 5.4: Change in MPS performance, Δ A_5/A_3, as a function of solution viscosity of three different batches of SPIONs with increasing average diameters. Performance is compared to that of each SPION batch in water. Monte Carlo simulation results (lines) of equivalent SPION characteristics show comparable performance to experimental results (points) over an expected range of viscosities.

SPIONs as observed by Monte Carlo simulations. A visual change in the shape and magnitude of the hysteresis curves would indicate a change even if the calculate A_5/A_3 did not. Fig. 5.5 shows the hysteresis curve for the minimum and maximum viscosities, and there is an apparent lack of even a minimal change between the two cases.

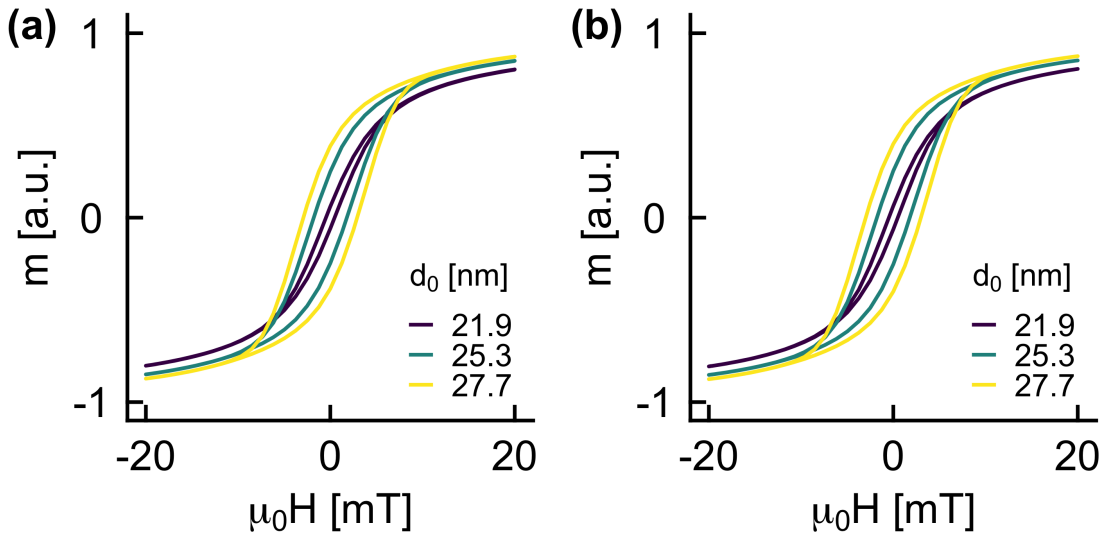

Figure 5.5: Simulated hysteresis curves for $8.9\text{x}10^{-4}\,\text{Pa}\cdot\text{s}$ (a) and $3.2\text{x}10^{-2}\,\text{Pa}\cdot\text{s}$ (b).

5.4 Magnetostatic energy and thermal destabilization

With viscosity ruled out as a significant factor, it is necessary to address magnetostatic interactions of SPIONs. It is possible to estimate the magnetostatic interaction energy by making assumptions about the size, magnetic properties, and alignment of multiple SPIONs with one another. The magnetostatic interaction energy, previously discussed in §5.2, is here reiterated for completeness. It is defined by

$$\varepsilon_{pp-IA} = -\sum_i \frac{\mu\mu_i\mu_0}{4\pi r_i^3}\left(3\left(\hat{\mathbf{m}}\cdot\hat{\mathbf{r}}_i\right)\left(\hat{\mathbf{m}}_i\cdot\hat{\mathbf{r}}_i\right) - \hat{\mathbf{m}}\cdot\hat{\mathbf{m}}_i\right) \tag{5.12}$$

where the magnetic moments, μ and μ_i are equal to $M_s V_c$ or the saturation magnetization times the core volume of the SPIONs. M_s is based on previously determined experimental

ranges, and the V_c is calculated by the volume of a sphere with the SPION diameter. The vector relationship between dipoles defined by

$$\left(3\left(\hat{\mathbf{m}}\cdot\hat{\mathbf{r}}_i\right)\left(\hat{\mathbf{m}}_i\cdot\hat{\mathbf{r}}_i\right)-\hat{\mathbf{m}}\cdot\hat{\mathbf{m}}_i\right) \tag{5.13}$$

is assumed to equal to two in this simplified case. This simplified equation is then used to calculated the magnetostatic energy and is plotted as a function of SPION diameter. Fig. 5.6 shows this range of diameters and energies in relation to the random thermal energy of the system, k_BT, at the temperature in which MPS measurements are carried out, 25 °C. Here it is notable that interparticle separations below approximately 100 nm for diameters greater than 30 nm are unable to destabilize through only random thermal energy. Below diameters of 30 nm there is a range of interparticle separations from approximately 50 to 90 nm where magnetostatic energy is most likely to dominate when compared to random thermal energy.

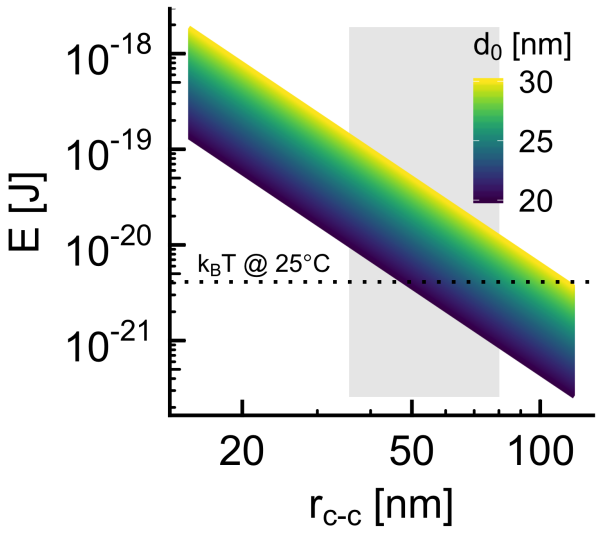

Figure 5.6: Magnetostatic interaction energy over a reasonable range of expected particle separations, $r_{c\text{-}c}$, with the left and right curves being the minimum and maximum expected energies, respectively. The dotted line represents the energy of random thermal motion, k_BT, at 25 °C.

With this initial approximation of the interparticle separations, it is now relevant to

determine if SPIONs dispersed in various environments exist with interparticle separations that fall under the stable or unstable regime in the comparison of magnetostatic and random thermal energy.

5.5 Interparticle separation in aqueous environments

Magnetostatic interactions are generally not brought into consideration when SPIONs are well dispersed in aqueous solution. This is true in the case of perfect solutions and when the core diameter of the SPIONs is below approximately 25 nm. When the solutions are not well dispersed, either due to electrostatic aggregation or interaction of the polymer coating trapping SPIONs in close proximity, then magnetostatic interactions vary across the distribution in a given volume. There may be a large percentage that is indeed well dispersed, but the signal can include a portion of which are interacting and reduce the maximum signal intensity or generate a "hump" or "shoulder" under an ac magnetic field.

When SPIONs are well dispersed, their average interparticle separation, r, can be estimated by

$$r = n^{-1/3} \tag{5.14}$$

where the particle density, n, is found by

$$n = N_{np}/V \tag{5.15}$$

where N_{np} is the number of nanoparticles in solution and V is volume of the same solution. N_{np} is a function of the mass of nanoparticles in solution, m_{np}, and mass of an individual nanoparticle core, m_c related by

$$N_{np} = m_{np}/m_c \tag{5.16}$$

As the concentration of iron, c_{Fe}, is a knowable quantity through elemental analysis by ICP,

m_{np} is determined as a function iron mass rather than the mass of magnetite iron oxide. As a result, m_{np} is found by

$$m_{np} = 1.382 \cdot c_{Fe} \cdot V \tag{5.17}$$

where the factor of 1.382 is a conversion of iron oxide nanoparticle mass to iron mass. m_c is dependent on the number of iron oxide unit cells, N_{uc}, and the mass of an individual iron oxide unit cell, m_{uc}, where

$$m_c = N_{uc} \cdot m_{uc} \tag{5.18}$$

N_{uc} is a function of the volume of an individual nanoparticle core, V_c, and the volume of an iron oxide unit cell, V_{uc}, related by

$$N_{uc} = V_c / V_{uc} \tag{5.19}$$

V_c is equal to the volume of a sphere of diameter, d_c, and V_{uc} is equal to the volume of a cube with edge length defined by the lattice parameter for magnetite, a. Lastly, m_{uc} is determined by the number and mass of iron atoms in a unit cell, n_{Fe} and m_{Fe}, and the number and mass of oxygen atoms in the same unit cell, n_O and m_O. The total m_{uc} is determined by

$$m_{uc} = (n_{Fe} \cdot m_{Fe}) + (n_O \cdot m_O) \tag{5.20}$$

Combining Eq. 5.14 through Eq. 5.20 gives r as a function of only c_{Fe}. From this final equation, a series of concentrations can be inputted to determine the range of interparticle separations for aqueous dispersed SPIONs. Fig. 5.7 shows two iron concentration ranges, 0.2 to 5 mg mL^{-1} and 5 to 20 mg mL^{-1}, which are the typical concentrations of SPION dispersions and excessively high concentrations illustrating the extreme case. Each of these situations show that well dispersed SPIONs in aqueous environments will remain greater than 200 nm apart in the typical case and greater than 100 nm apart in the extreme case.

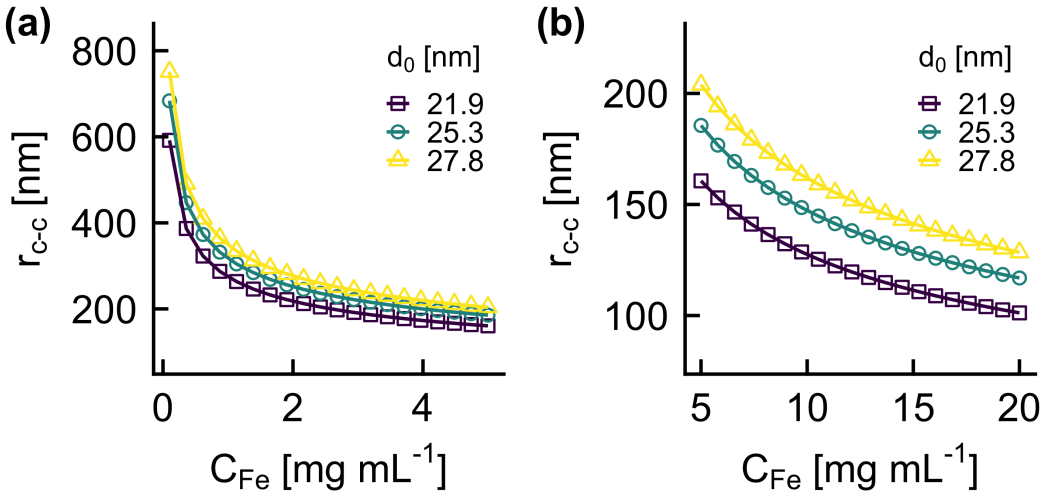

Figure 5.7: Interparticle separations of SPIONs at iron concentrations of 0.2 to 5 mg mL^{-1} (a) and 5 to 20 mg mL^{-1} (b). Separations for typical ranges do not drop below 200 nm while extreme concentrations do not drop below 100 nm.

Comparing these expected interparticle separations to the range of stable and unstable separations and associated magnetostatic interactions supports the assumption that SPIONs well dispersed in aqueous solution are stable with only random thermal energy. Fig. 5.6 illustrated that SPIONs with diameters between 20 and 30 nm are stabilized by random thermal energy when interparticle separations are greater than approximately 100 nm.

5.6 Interparticle separation in intracellular environments

When SPIONs are internalized into cytoplasmic vesicles within a cell, the previously discussed dispersion characteristics of well-dispersed SPIONs no longer holds. The endocytotic mechanisms of internalization including the surrounding and encapsulation of SPIONs in vesicles of cellular membrane forces them into closer proximity than when they are free-floating in the extracellular space. This has been qualitatively observed by direct imaging of internalized SPIONs by TEM as was shown in Chapter 4. It is now crucial to quantify the intracellular interparticle separations of SPIONs to determine if their magnetostatic energy can be overcome by random thermal energy.

Specific characteristics of the sample preparation process of biological materials for TEM, including ultra-thin section thickness and well calibrated known pixel size of obtained images, allow for determination of interparticle separations in the projected image of a three-dimensional sample.

5.6.1 Methods

Samples were prepared as previously discussed in §4.4.1. Raw images with calibrated pixel size metadata were imported into ImageJ and the center point of individual SPIONs, contained within cytoplasmic vesicles, were manually selected. Manual identification was chosen to ensure inclusion of all SPIONs including those that are overlapping in the projected images. The manually selected SPION positions were then processed by a Python script, shown in full in Appendix G, which determines the first nearest neighbor distance from each SPION. An example of the radial nearest neighbor distances is shown in Fig. 5.8.

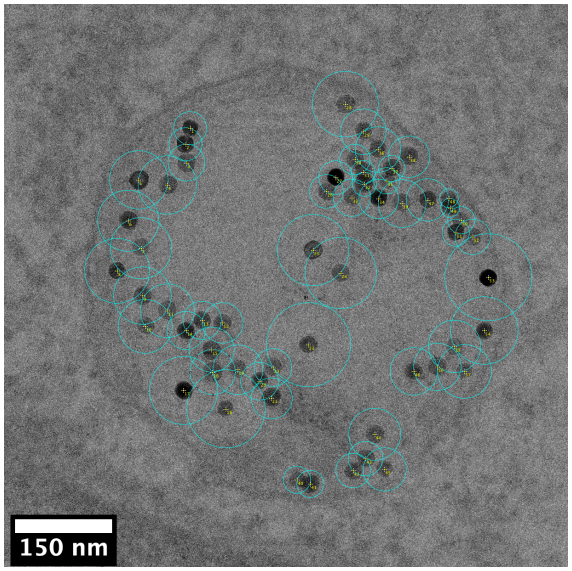

Figure 5.8: Example TEM image of SPIONs internalized in an endosome/lysosome with overlay from radial interparticle separation analysis

5.6.2 Results & discussion

Two-dimensional interparticle separations, $x\text{-}y_{c\text{-}c}$, for two exposure concentrations of iron have been tabulated and are shown in Fig. 5.9. It is observed that SPIONs internalized in cytoplasmic vesicles are primarily between 10 to 100 nm with a mean and standard deviation for both observed concentrations 36.4 ± 22.2 nm apart. In reality, the lower end of this range of interparticle separations is not possible due to the core diameter being greater than 20 nm. These values are instead an artifact of three-dimensional space being imaged as a two-dimensional projection.

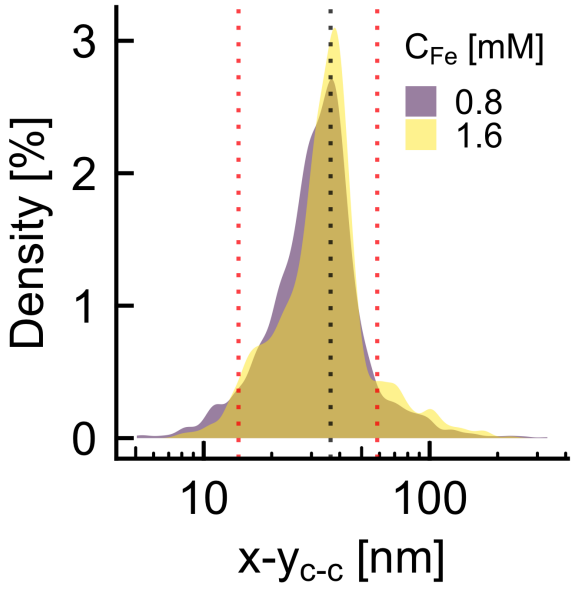

Figure 5.9: Direct observation of two-dimensional intracellular SPION interparticle separations as a function of concentration. The mean (black line) and first standard deviation (red lines) show the majority of two-dimensional SPION interparticle separations.

Additionally, there is virtually no change when comparing the two concentrations as their means differ by 2.5 nm with equal standard deviations. This suggests that there is a lower limit to the possible interparticle separation dictated by the coating surrounding the SPIONs. This steric bulk does not appear to degrade significantly over the 24 h period of incubation

meaning that it can maintain a physical barrier between individual SPIONs. This concept is discussed in greater detail in Chapter 6.

Samples have been prepared as ultra-thin sections of resin with biological and SPION material encased within. As the ultra-thin section thickness is set to 70 nm, the maximum z-separation, $z_{c\text{-}c}$, between individual SPIONs possible for the collected images is 70 nm. The range of possible three-dimensional interparticle separations, $r_{c\text{-}c}$, has been estimated using the Pythagorean theorem, as illustrated in Fig. 5.10, where $z_{c\text{-}c}$ is set at approximately equal intervals throughout the thickness of the ultra-thin resin sections. These are shown as $z_{c\text{-}c}$ equal to 30, 50, and 70 nm in Fig. 5.11a.

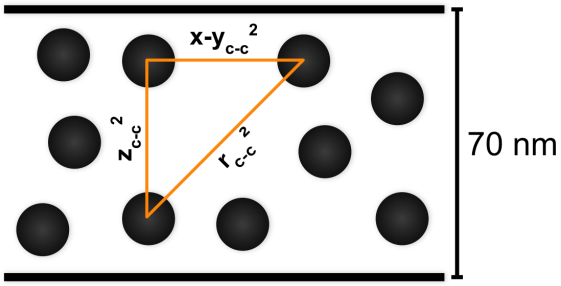

Figure 5.10: Illustration of a side-view of how $r_{c\text{-}c}$ was determined using previous direct measurements of x-$y_{c\text{-}c}$ and known maximum possible $z_{c\text{-}c}$ in the pythagorean theorem.

The averages of the minimum and maximum $z_{c\text{-}c}$ histograms can be used as a range of the most likely $r_{c\text{-}c}$. These average $r_{c\text{-}c}$ values are used to compare magnetostatic interaction energies to the thermal energy of the system, Fig. 5.11b. It is observed that the magnetostatic energy of SPIONs in the size range in this work is expected to be significant and unable to be destabilized by random thermal energy, k_BT.

5.7 Effect of magnetostatic interactions on SPION response

Based on the calculation of expected magnetostatic energy of SPIONs, it is hypothesized that interparticle interactions, even without destabilization of surface coatings and direct aggregation, are the dominant contribution to decreased magnetic performance after inter-

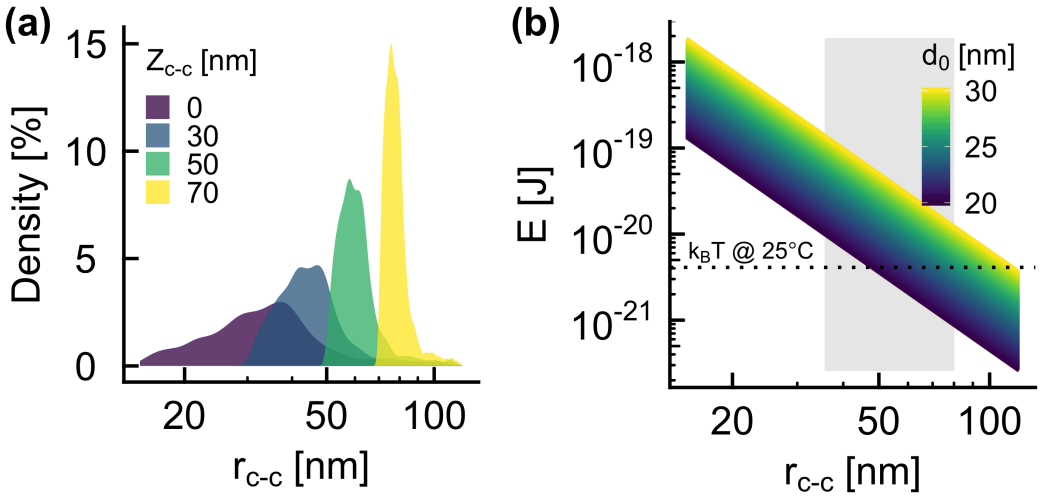

Figure 5.11: Direct two-dimensional and estimation of three-dimensional interparticle separations as observed by TEM (a). The gray region highlights the range interparticle separations possible within the constraint of ultra-thin section thickness as a maximum Z-separation. Dipole-dipole interaction energies are compared to random thermal energy, k_BT, over the extracted range of interparticle separations (b). The dipole-dipole interaction energy is notably higher than random thermal energy over most of this range.

nalization. To support this hypothesis, it is necessary to experimentally and theoretically observe nanoparticle magnetic performance under changing average interparticle separations.

5.7.1 Methods

To control for interparticle separation experimentally, SPIONs have been dispersed in solutions of mannitol and deionized water with varying w/w% of mannitol. Mannitol solutions were previously prepared over a range of total wt%/w according to Table 5.3.

Once the initial solutions were prepared, 133 µL of each was added to 17 µL of SPION dispersion and mixed thoroughly by pipette. The final mixture wt%/w was accounted for in the slight dilution with SPION dispersion. The sample tubes containing the mixtures were plunge-frozen in liquid nitrogen for 4 min and immediately transferred to a freeze dryer (Labconco, Kansas City, MO, USA) for lyophilization. Once thoroughly dry, the samples

Table 5.3: Mannitol solution preparation.

Initial w/w%	$m_{mannitol}$ [g]	m_{H_2O} [g]	Mixture w/w%
0.37	0.07	20	0.33
0.82	0.16	20	0.73
1.82	0.36	20	1.62
4.05	0.81	20	3.59
9.00	1.80	20	7.98
20.00	4.00	20	17.73

were removed from the freeze dryer and immediately characterized by MPS.

5.7.2 Results & discussion

Increasing mannitol w/w% has the effect of increasing physical bulk between nanoparticles on average and thus increasing their interparticle separations. Fig. 5.12a illustrates the performance of three different average core size SPIONs as a function of increasing mannitol w/w%. Here it is noted that increasing average core size has the effect of significantly degrading magnetic performance as nanoparticles are allowed to associate and magnetostatically interact more closely. The largest core size of the three shows a greater than 80% reduction in A_5/A_3 while the next smallest only shows approximately a 20% reduction. The smallest of the three sizes shows no change in magnetic performance over the possible interparticle separations in this study suggesting that its magnetostatic interaction energy is not significant until the particles are allowed much closer together.

Direct calculation of the interparticle separation is limited by the two-dimensional projection approximation and the experimental results, though broadly in agreement, are not entirely sufficient; thus the experimental results are also compared to Monte Carlo simulations. Fig. 5.12b illustrates supporting trends in SPION magnetic performance between approximately 40 to 60 nm center-to-center interparticle separations. This is a more detailed examination of the magnetostatic interaction energy with non-linear dynamics and thus more realistic than the first principles approximation in Fig. 5.11b.

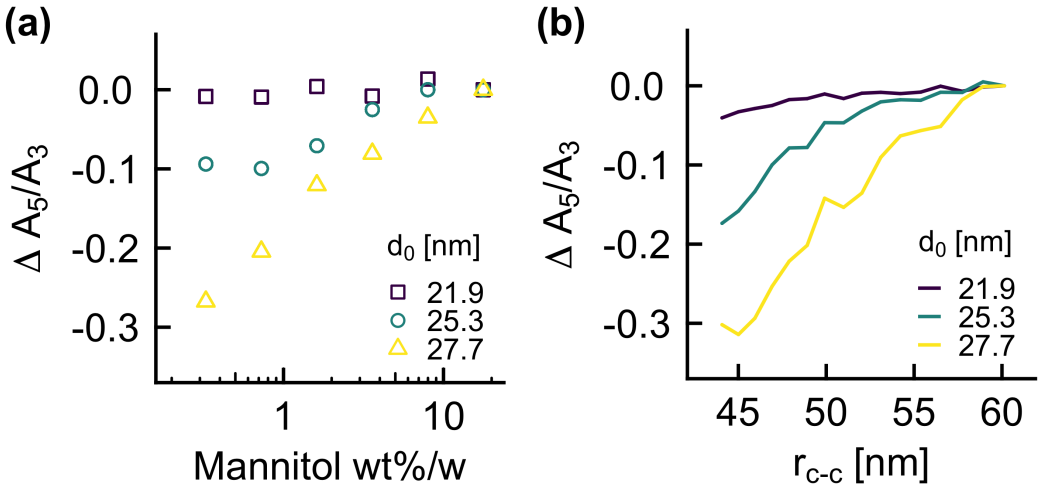

Figure 5.12: Change in MPS performance, Δ A_5/A_3, as a function of mannitol w/w% (a) and theoretical interparticle separation (b) of three different batches of SPIONs with increasing average core diameters. Performance is compared to that of the greater interparticle separation case. As before, Monte Carlo simulations support experimental trends over observed interparticle separations.

In the first principles approximation, there were assumptions made about SPION magnetic properties, relative alignments of magnetic moments, and the number of interacting particles at a given time (two in that case.) The Monte Carlo simulations allow for calculation of interactions of a much larger, and closer to reality, number of SPIONs in each run as well as including other important factors like thermal fluctuations. The primary limitation of the Monte Carlo simulations of the Néel-only case is the need to fix SPIONs in specific positions in the theoretical "box" in order to prevent unrealistic overlap of individual magnetic moments.

A potential limitation of the Monte Carlo simulation obtained magnetostatic interaction distance of 40 to 60 nm is the expected overlap of the polymer coating at these distances if it is assumed that SPIONs have an average hydrodynamic size of 50 to 90 nm. This suggests that the majority of SPIONs would never be able to come into close enough proximity for the magnetostatic interaction distance to be relevant. Fig. 3.16 illustrated the full distribution of hydrodynamic sizes for each of the experimental observations in this work. Here it is important to note that, even for the two different distribution ranges, there is still a significant

percentage of the hydrodynamic sizes of that fall within or below the range necessary for magnetostatic interactions to occur and play a role in decreases SPION performance. This variation in hydrodynamic size is the result of incomplete and over abundance of polymer coating on the surface of SPIONs as well as the inherent distribution of the molecular weight of PMAO-PEG after the copolymer synthesis process.

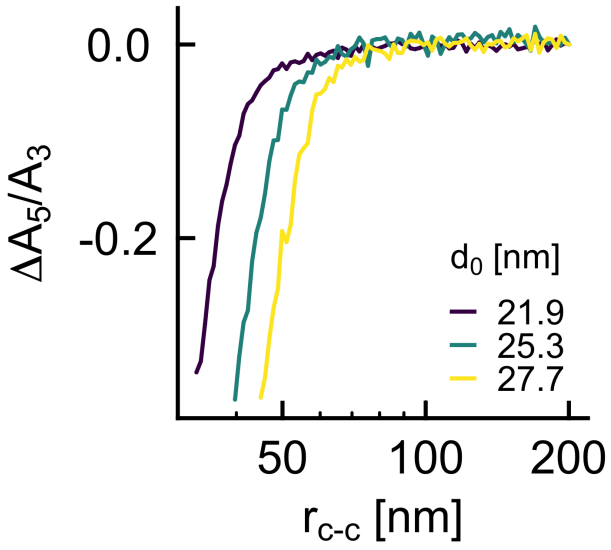

Figure 5.13: Expanded range of A_5/A_3 as a function of interparticle separations from Monte Carlo simulations illustrating each core size's completely loss of signal with continued decreases in separation.

Based on these results, it is concluded that the magnetostatic interactions between SPIONs within cells are the dominant and significant contributor to changing magnetic performance. The latter is a crucial point for which Magnetic Particle Imaging characteristics of SPIONs must be optimized. It is now understood that increasing interparticle separations before and after internalization leads to an overall improved magnetic performance in MPI.

It is important to note that the Monte Carlo simulations shown in Fig. 5.12b are a subset of the total range of observed interparticle separations from 30 to 200 nm. The full range of interparticle separations and the resulting change in A_5/A_3 is shown in Fig. 5.13. It is

observed that A_5/A_3 for all three core sizes decreases significantly when brought into close enough proximity, but that each drop starts and ends at different values of interparticle separation. They continue to follow the expected trend with the smallest of the three core sizes maintaining magnetic performance up to the closest interparticle separations, and the inverse is true for the largest of the core sizes.

As with the observation of viscosity by Monte Carlo simulation, the hysteresis curves at low and high interparticle separations can elucidate any further changes not already observed by the change in A_5/A_3. Fig. 5.14 shows the hysteresis curves for the 30 and 200 nm interparticle separations. Here it is clear that a collapse of the hysteresis curves has occurred at the 30 nm interparticle separation and that the response is much noisier than the 200 nm case. This is further confirmation of the loss of magnetic performance with decreasing interparticle separation.

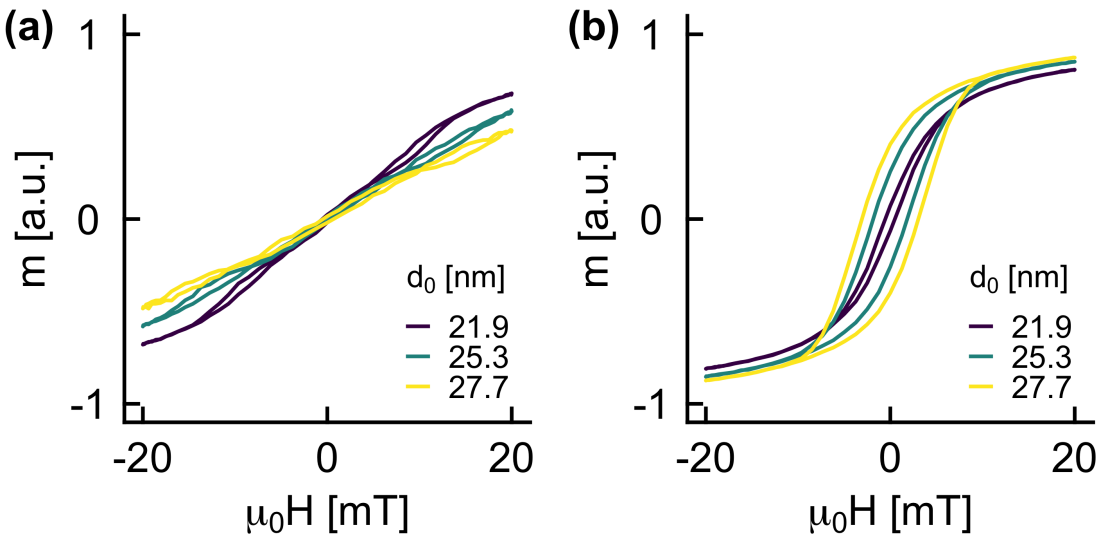

Figure 5.14: Simulated hysteresis curves for 30 and 200 nm separations.

5.8 Summary

Based on the results and discussion here, it is clear that the magnetic response of SPIONs within the size range approaching those optimized for MPI are primarily affected by inter-

particle interactions after internalization in cells. The constrained environment into which SPIONs are encapsulated after internalization forces SPION interparticle distances where magnetostatic energy dominates over thermal energy creating an increased energy barrier for magnetic relaxation. This informs the sizes of SPIONs usable for quantifiable biomedical imaging and diagnostic applications under conditions where coatings can not be varied. It further informs the necessary changes to SPION coatings that must be applied in order to recover magnetic performance through increasing interparticle separation.

Chapter 6

STERIC CONTROL OF MAGNETIC DYNAMICS OF INTRACELLULAR SPIONS

The work here has established a foundational knowledge base around magnetostatic interactions as the dominant factor in changes to SPION performance in MPS and the expected performance change in MPI. A logical follow-up that arises is: is it possible for the magnetic performance of SPIONs internalized in cells to be improved? Or even made to experience no change in performance as when observed in aqueous dispersions? This requires an examination of how SPIONs can be arranged within a cell and how their interparticle separation can be controlled.

6.1 Potential mechanisms for increasing interparticle separation

Previously, it was determined that SPIONs are localized within endosomes and lysosomes after internalization in cells. With this consideration, there are three potential routes through which interparticle separation can be increased to decrease the magnetostatic interaction energy between them. The routes include forced segregation of SPIONs into a higher number of individual cytoplasmic vesicles, an increased amount of electrostatic repulsion between individual SPIONs by increasing the total surface charge on each particle, and an increased amount of physical bulk surrounding each SPION through control of the coating material. These three potential mechanisms are illustrated in Fig. 6.1 with increasing quantities of each route moving from left to right. The viability of each mechanism is discussed in the following sections.

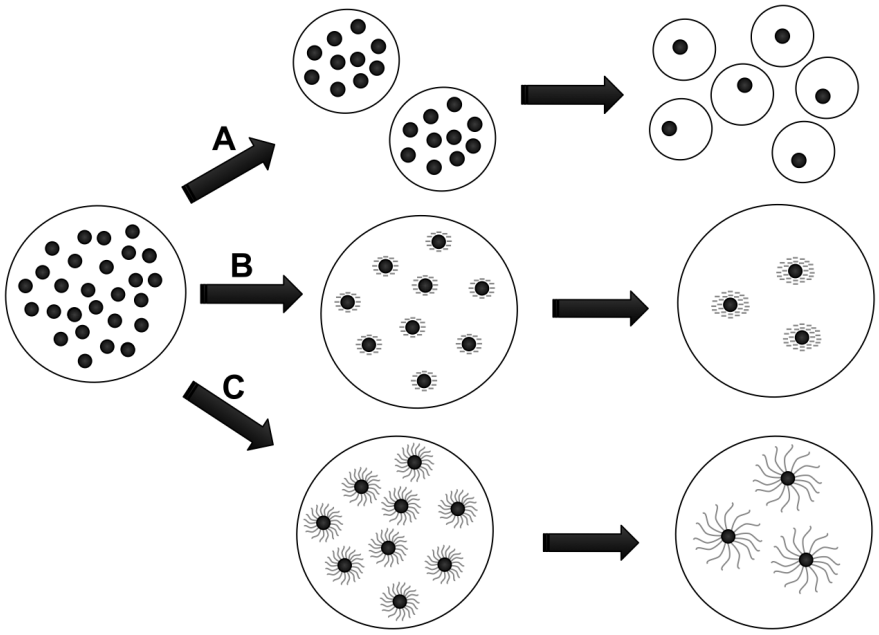

Figure 6.1: Graphical depiction of SPIONs within an endosome or lysosome. Path A shows segregation into individual vesicles. Paths B and show increasing surface charge and physical mass, respectively, around each SPION to increase average interparticle spacing while still in one vesicle.

6.1.1 Number of SPIONs per vesicle

Decreasing the number of SPIONs in each cytoplasmic vesicle requires that the average interparticle separation in solution increases. As the interparticle separation in solution is increased, the number of SPIONs that encounter a given location on the surface of a cell decreases. The endocytotic uptake pathways utilized by cells of the type in this work depend on the accumulation of SPIONs on the exterior surface of the cell and internalization follows through an internal or external cellular stimulus. Fewer particles at any given locations on the exterior of the cellular membrane mean a decrease in the resulting number of SPIONs in each endosome that forms within the cells.

Without affecting the properties of SPIONs, as those methods are considered in the following sections, SPION concentration remains as the only route to increase the interparticle separation of SPIONs dispersed in aqueous media. It is possible to decrease the concentration of SPIONs exposed to the cells, but this also decreases to the total amount of iron mass that is transferred to the interior of the cell. This means that there is a decreased maximum potential signal from the SPIONs in an imaging application such as MPI. As it already requires a significant amount of mass within each cell to reasonably detect SPIONs above instrument noise, it is not a viable method for improving the overall acquired signal. The lost signal due to magnetostatic interactions would be replaced by decreased signal due to lower iron mass, which potentially would be worse for final use in imaging and therapy applications.

6.1.2 Increased electrostatic repulsion

The electrostatic repulsion between SPIONs in solution is dominated by the zeta potential, ζ. Zeta potential is a measure of the charge on a surface and increases as the number of charged functional groups in the nanoparticle coating increases. It is then possible to increase the zeta potential through the exchange of PEG in the amphiphilic polymer coating of these SPIONs with another more highly charged species or through a reduction in the total content of conjugation on PMAO exposing the carboxylic acids of an opened anhydride ring. The

charged species can be either negative or positive, but not a combination of both as that would decrease the effective zeta potential and desired electrostatic repulsion.

While it is possible to increase the electrostatic repulsion between SPIONs, there is a resulting reduction in their colloidal stability in biologically relevant environments. As was discussed in Chap. 2, poor colloidal stability of highly charged species occurs in solutions with high salt contents, as is true of biological environments. This is due to the bridging effect of oppositely charged ions on the charged functional groups in the SPION coating. As ion content increases, electrostatic attraction between individual SPIONs occurs, resulting ultimately in aggregation and complete loss of colloidal stability. Due to this limitation, increasing the electrostatic repulsion between SPIONs to decrease magnetostatic interactions is not a viable option.

6.1.3 Increased steric bulk

The final potential route for increasing interparticle separation of SPIONs in cells is to increase the steric bulk that physically maintains a minimum separation despite external constriction from the cytoplasmic vesicles. The most promising candidate to accomplish this is increasing the molecular weight of the PEG molecule that is used to synthesize the amphiphilic polymer coating, PMAO-PEG. This maintains the desired properties of SPIONs for MPI, including long circulation times *in vivo* and biocompatibility, without decreasing the magnetic signal. An assumption is made in this case that the hydrodynamic size in solution is not significantly changed when varying the molecular weight of the PEG molecule as this can potentially affect the *in vivo* circulation time of SPIONs. Sufficient quantities of PEG, as was shown in Fig. 2.9a in Chap. 2, can be readily purchased in molecular weights ranging from 0.5 to $40\,\mathrm{kg\,mol^{-1}}$.

An added potential benefit of this method includes the expected constant or improved colloidal stability of SPIONs in aqueous solution. Based on these expected properties, the variation of steric bulk is chosen as a viable candidate for further examination as a method of alleviating magnetostatic interactions of internalized SPIONs.

6.2 Preparation of variable molecular weight amphiphilic polymers

The SPIONs utilized in Chap. 4 and 5 were coated with PMAO-PEG prepared with approximately 5% loading of 20 kg mol^{-1} PEG. Here, three molecular weights of PEG were chosen including 10, 20, and 40 kg mol^{-1} to prepare PMAO-PEG. All samples were maintained at 5% loading to limit variation in electrostatic interactions between SPIONs through surface charge. Also, the same batches of as-synthesized SPION cores were used here to allow for direct comparison to past magnetic performance.

6.2.1 Methods

Briefly, poly(maleic anhydride-alt-1-octadecene) (PMAO) and amine-terminated polyethylene glycol (PEG) were each added to solutions of dichloromethane (DCM) and small amounts of triethylamine (Et_3N), allowed to dissolve fully; then the solutions were combined in one container. The reaction was allowed to proceed for 48 h and while watching for signs of reactions progress noted by increasing viscosity of the solution as observed by changing stir bar procession under constant set point. It was noted that 10 kg mol^{-1} PEG caused significantly less viscosity increase than 20 kg mol^{-1} and 40 kg mol^{-1} PEG.

The resulting copolymer was dried by rotary evaporation, placed under vacuum for several days, and then dissolved in deionized water. The new solution was transferred to 100 kDa cutoff tubing and put in a beaker with deionized water. The water was replaced several times over two to three days, and the purified product was then transferred to a round-bottom flask. The solution was frozen in a dry ice/acetone bath while spinning at 300 rpm. The copolymer was lyophilized over four days, and the final product collected and weighed. It was then stored under vacuum or inert gas until used in the SPION coating process.

6.3 Magnetic performance in aqueous dispersion

It is observed that increasing the molecular weight of PEG in PMAO-PEG SPION coatings improves the overall magnetic performance of SPIONs dispersed in water. This is shown in

Fig. 6.2 where increasing PEG molecular weight improves all of the desired performance characteristics in MPS. Fig. 6.2a-b illustrate increasing mass normalized intensity and decreasing FWHM in MPS as PEG molecular weight is increased. These trends correlate to higher signal intensity and improved resolution in MPI as previously discussed. Fig. 6.2c-d show decreased loss of amplitude with increasing harmonic number and the resulting improvement to A_5/A_3.

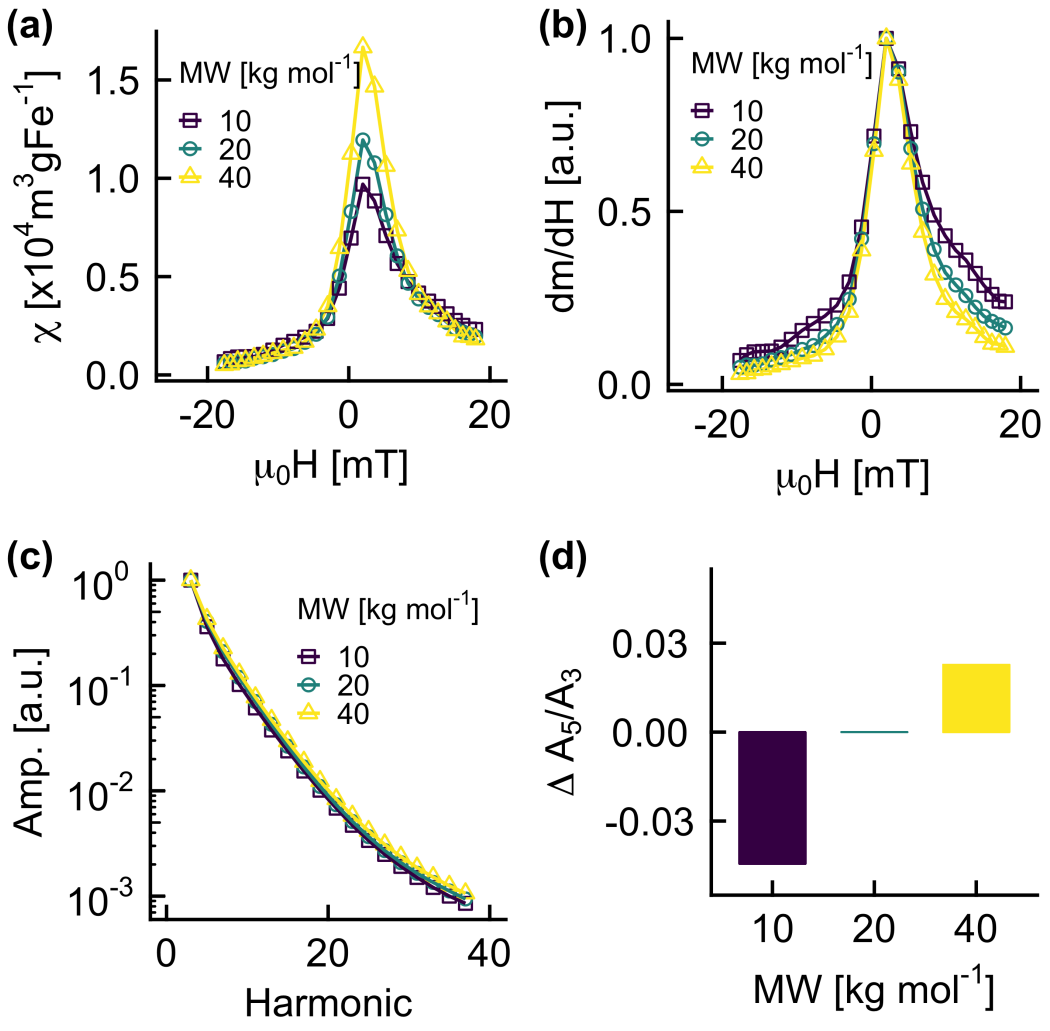

Figure 6.2: SPIONs with three different molecular weights of PEG (10, 20, and 40 kg mol^{-1}) used to synthesize PMAO-PEG and characterized by MPS including mass normalized PSF (a), normalized PSF (b), normalized harmonic spectra (c), and $\Delta A_5/A_3$ normalized to A_5/A_3 for 25.3 nm SPIONs (d).

These SPIONs show promising trends for SPIONs dispersed in aqueous environments. It is expected that the improvements are correlated to an increase in the minimum interparticle separation between individual SPIONs in the dispersion. In an aqueous dispersion of SPIONs, there is a random distribution of SPIONs throughout which a portion is closer than the average interparticle separation, which can be within the necessary distance for magnetostatic interactions to occur. The increase of steric bulk on the surface of the SPIONs thus provides an increase to the minimum possible distance between those SPIONs that are in the portion of more closely dispersed particles. This provides a decrease in the number of SPIONs that can potentially ever interact and cause a decrease to the final magnetic performance.

These results from freely aqueous dispersed SPIONs illustrates the strong potential that increasing the molecular weight of PEG has in improving the internalized magnetic performance of cells through decreasing magnetostatic interactions.

6.4 Magnetic performance in vitro

Direct observation of SPIONs *in vitro* is required to determine if the improvements observation in aqueous dispersions hold true under the harsher and more variable environment within cells. SPIONs have been incubated with HT-1080 cells under identical conditions as described in Chap. 4 and 5. Fig. 6.3 illustrates the resulting change in magnetic performance, as determined by A_5/A_3, for 25.3 and 27.8 nm with PMAO-PEG coatings containing 10, 20, and 40 $\mathrm{kg\,mol^{-1}}$ PEG.

Here it is observed that there is the expected trend of decreased signal when the molecular weight of PEG is decreased, and the inverse increase in signal for an increased molecular weight of PEG. The amount of change is not constant and appears to be non-linear between the two different core sizes. As the core size is increased or decreased, a resulting amplified change in performance is noted. This is due to the variation in magnetostatic energy generated between different core sizes over equivalent interparticle separations. Increasing separation is more likely to have a more significant effect on smaller core sizes as the magnetostatic interaction for larger core sizes continues over greater distances. This is reinforced by the

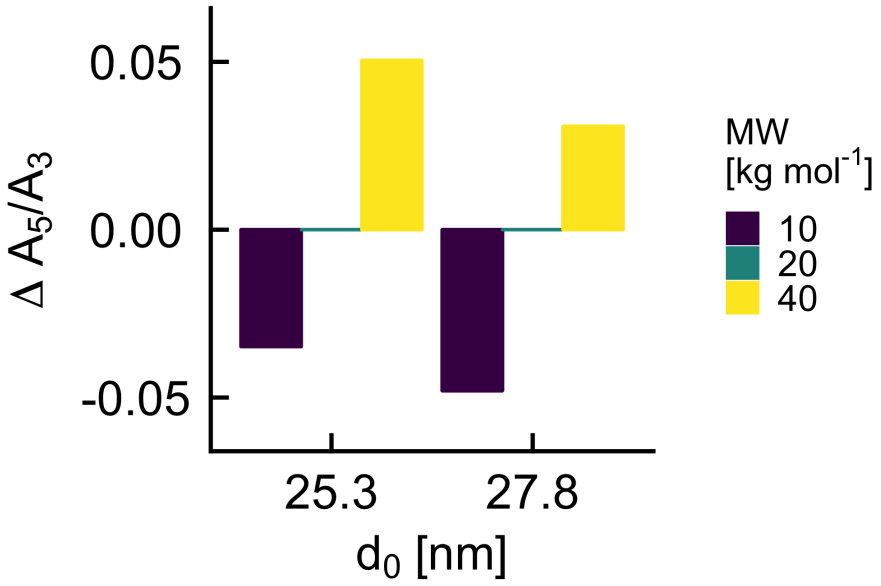

Figure 6.3: Δ A_5/A_3 after internalization in HT-1080 cells of two different batches of SPIONs (25.3 and 27.8 nm) and three different molecular weights of PEG (10, 20, and 40 kg mol^{-1}) normalized to A_5/A_3 for the 20 kg mol^{-1} samples.

more significant drop in A_5/A_3 when decreasing the PEG molecular weight of the larger core size.

Despite the non-constant improvement or reduction of performance *in vitro*, there remains a significant improvement for MPI optimized core sizes when increasing PEG molecular weight.

6.5 *Interparticle separation* in vitro

Image analysis of SPIONs internalized in cells was carried out to verify that SPIONs were being separated to a greater extent when coated with higher molecular weight amphiphilic polymer. This comparison included two core sizes, 25.3 and 27.8 nm, and two PEG molecular weights, 20 and 40 $\mathrm{kg\,mol^{-1}}$.

6.5.1 Methods

Samples were prepared as previously discussed in §4.4.1. The differences included the exclusion of heavy metal post-staining with lead and gadolinium. Scanning probe imaging was carried out using an FEI Tecnai G2 F20 Supertwin with a Gatan CCD camera and operated at 200 kV.

Image processing and interparticle separations were determined as described in §5.6.1. A minimum of 2000 particles and associated interparticle separations were counted for each sample over 10 to 20 images of internalized SPIONs in cells.

6.5.2 Results & discussion

SPIONs internalized in HT-1080 cells with variable core size and coatings show consistent results to those in §4 in regards to uptake and physical stability after 24 h. The SPIONs are only internalized in lysosomes and endosomes and continue to be absent from the nucleus, free-floating in the cytoplasm, or adhered to the exterior surface of the cell membrane. A qualitative examination of internalized SPIONs with two core sizes and two molecular weight

coatings, example images of which are shown in Fig. 6.4, do not immediately show differences in their interparticle separations. The SPIONs distribution in lysosomes and endosomes and the number of particles in each is variable from vesicle to vesicle and is not consistent over the collected images. As a result, quantitative image analysis is required before any information can be extracted.

Histograms of SPION interparticle separations are determined by placing a marker at the center of every internalized SPION in an image and using a script to extract the distance between each nearest neighbor particle. These histograms for two core sizes and coating molecular weights are shown in Fig. 6.5. Here, separations for 2000 SPIONs are compiled for each sample, and a notable shift to higher separation distances is observed. The images used to generate these histograms are two-dimensional projections of three-dimensional ultra-thin sections of cells and SPIONs. This means that there are SPIONs that appear to be overlapping or immediately adjacent that are separated by some vertical height not apparent in the images. A small shift in the two-dimensional separation is possibly much larger, but not accounted for in this analysis. This shift can only increase, however, as compared to the two-dimensional separation where is it not possible to observe less than zero vertical separation.

By extracting the mean and standard deviation of the interparticle separation histograms, we observed an approximate separation increase of 11 nm for the 25.3 nm cores and 3 nm. The exact values are included in Table 6.1. The standard deviations are on the same order of magnitude as the separations due to a large number of outliers with separations above 100 nm. It is difficult to attribute a true shift to the increase in mean values with increasing molecular weight coatings as these values assume a normal distribution of the separations, which is not necessarily the case and is not possible to determine without at least an order of magnitude higher number of observed internalized SPIONs.

Another approach to differentiating the interparticle separation distributions is to plot them, as shown in Fig. 6.6. Here a distribution is broken down to quartile regions of a distribution where the lower 25% and upper 75% quartiles both shift significantly to increased two-dimensional interparticle separations. The 25.3 nm sample shows a greater shift with

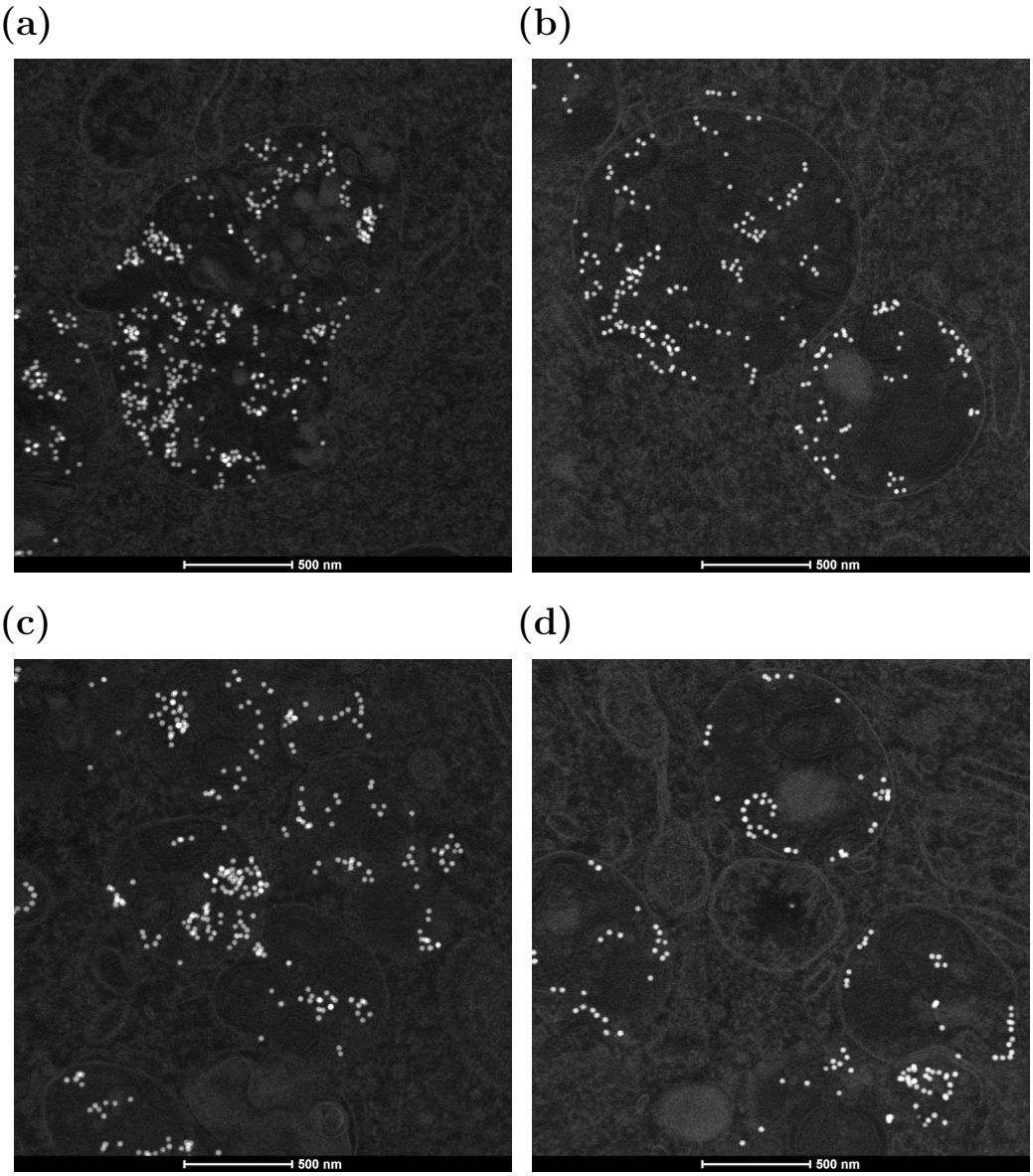

Figure 6.4: SPIONs internalization observed for 25.3 nm and 20 kg mol^{-1} (a), 25.3 nm and 40 kg mol^{-1} (b), 27.8 nm and 20 kg mol^{-1} (c), 27.8 nm and 40 kg mol^{-1} (d). Qualitatively it is difficult to discern if there are changes to the interparticle separation of SPIONs with variable molecular weight coatings.

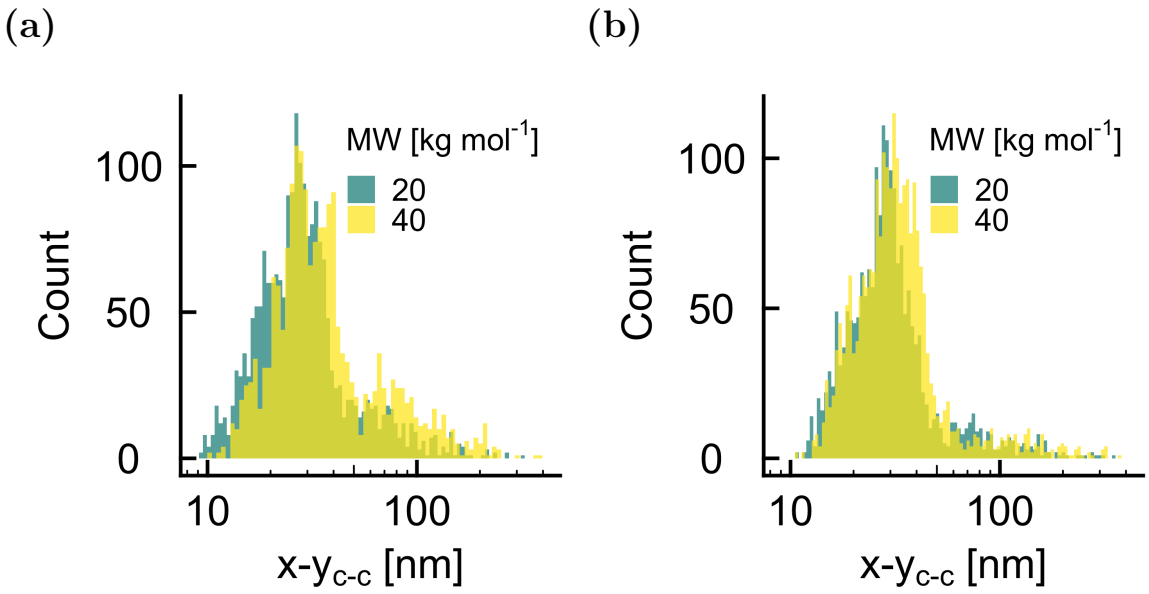

Figure 6.5: Histograms of two dimensional interparticle separations for two core sizes, 25.3 nm (a) and 27.8 nm (b), each with two PEG molecular weights, 20 and 40 kg mol^{-1}. Approximately 2000 separations are included for each sample with a clear shift to higher separations observed with increasing molecular weight coatings.

Table 6.1: Mean and standard deviation of two dimensional interparticle separations, x-$y_{c\text{-}c}$ [nm], of SPIONs with increasing molecular weight coatings coatings.

	MW [kg mol^{-1}]	
d_0 [nm]	20	40
25.3	34.31 ± 28.45	45.58 ± 39.10
27.8	36.22 ± 35.99	38.95 ± 35.55

increasing molecular weight coatings than the 27.8 nm sample. This is attributed to the lower overall magnetostatic interaction energy between the smaller SPION cores where, the larger cores are more likely to aggregate from the magnetic coupling between particles. This behavior of different core size SPIONs is often observed in the purification and phase transfer processes, and the coatings have previously been designed to alleviate aggregation where possible.

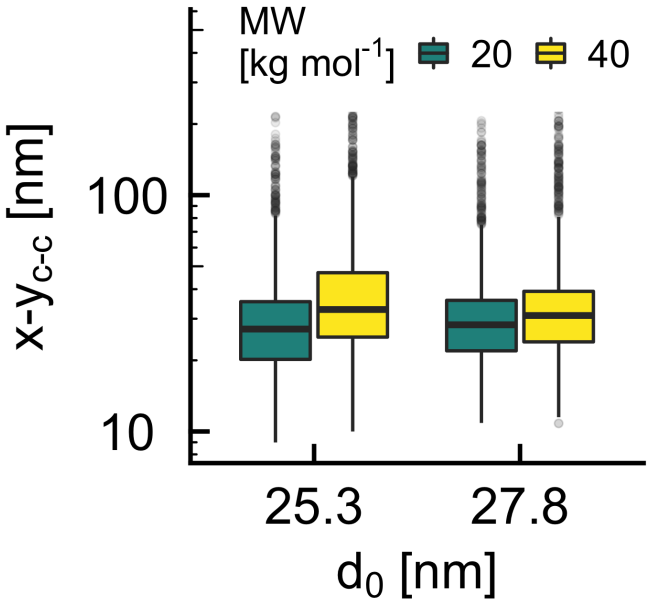

Figure 6.6: Increasing interparticle separation observed with increasing molecular weight of PEG in the amphiphilic coating of SPIONs. A larger increase is observed for 25.3 nm as compared to 27.8 nm SPIONs and is attributed to the difference in magnetostatic interaction energy between the sizes and its effect on aggregation promotion.

6.6 Effect of environmental conditions

Previously, it was shown that there was no change in magnetic performance when SPIONs are internalized in cells with respect to the viscosity of the environment. It is expected that this remains true for SPIONs with similar PMAO-PEG coatings with only a variation

in PEG molecular weight. However, the increase in molecular weight can increase the hydrodynamic diameter of the SPIONs or change the polymer conformation surrounding the SPIONs. This can cause variation in the hydrodynamic volume, V_h, which contributes to the Brownian component of SPION relaxation dynamics as shown in Eq. 5.3. While variation in hydrodynamic volume did not appear to cause variation in magnetic performance, it is important to confirm that this trend continues in addition to ensuring the viscosity also is not coming into play.

Table 6.2: Hydrodynamic sizes and polydispersity index, d_H [nm] (PDI), of SPIONs with variable coatings.

	MW [kg mol^{-1}]		
d_0 [nm]	10	20	40
25.3	81.3 (0.191)	87.1 (0.197)	78.5 (0.186)
27.8	77.0 (0.167)	77.5 (0.165)	82.6 (0.170)

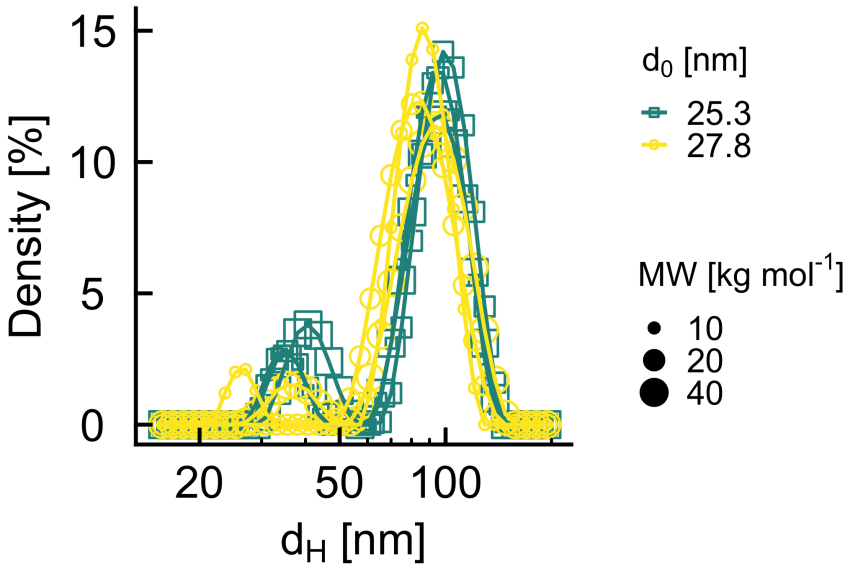

Figure 6.7: Hydrodynamic size with amphiphilic coatings containing variable PEG molecular weight. Peaks below 55 nm are negligible compared to the majority closer to the average d_H.

The hydrodynamic sizes of each SPION sample are characterized by DLS and are shown

in Table 6.2. It is observed that SPIONs show nearly constant hydrodynamic size and distributions. The hydrodynamic size distributions as a function of core diameter and PEG molecular weight are shown in Fig. 6.7.

SPION dispersions in mixtures of glycerol and deionized water have been prepared identically to those in Chap. 5 and characterized by MPS. The results, shown in Fig. 6.8 illustrate minimal to no change in performance for each core size and PEG molecular weight over one order of magnitude. Above this range, the largest of the three core sizes begin to show a small drop. This can either be classified as negligible or due to the increased effect of viscosity on larger coatings. As the largest core size with the largest coating appears to be in line with the lower viscosity measurements, the drop is most likely attributed to inconsistent mass or mixing for these samples.

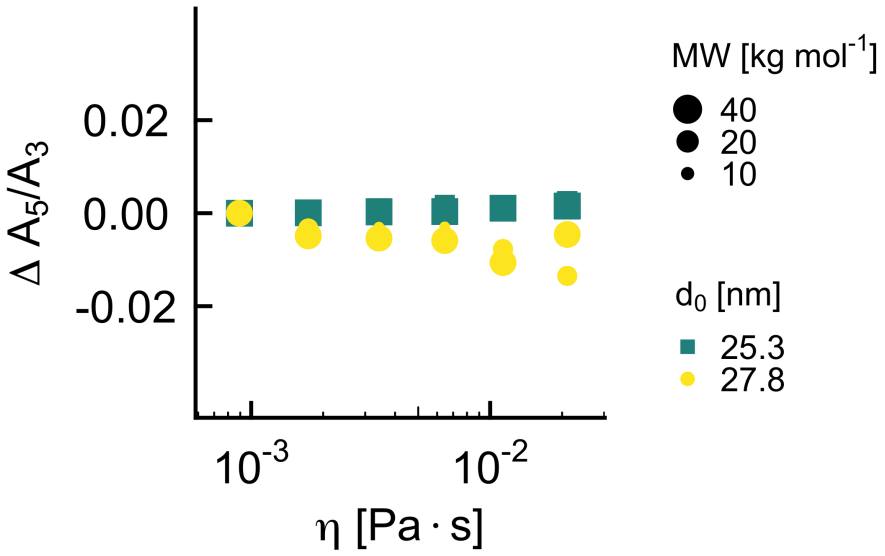

Figure 6.8: Δ A_5/A_3 as a function of solution viscosity of two different batches of SPIONs (25.3 and 27.8 nm) and three different molecular weights of PEG (10, 20, and 40 kg mol^{-1}) normalized to A_5/A_3 at the viscosity of water.

It is also important to note that the drop for the small percentage of samples at the high range of viscosities only accounts for 10-20% of the changes observed *in vitro*. Also, there was a noted increase in SPION magnetic performance after internalization and after entering the

expected higher viscosity environment of cytoplasmic vesicles, which is counter to the small decrease observed in controlled viscosity environments. It is possible that a small reduction has indeed occurred after internalization, but that it does not outweigh the improvements generated from decreasing the magnetostatic interaction energy.

To determine just how much magnetostatic energy has been varied after internalization, dispersions of SPIONs have been mixed with increasing quantities of mannitol and freeze-dried to remove the Brownian contribution altogether. These samples were prepared identically to those used in §5.7 and characterized by MPS after being thoroughly lyophilized.

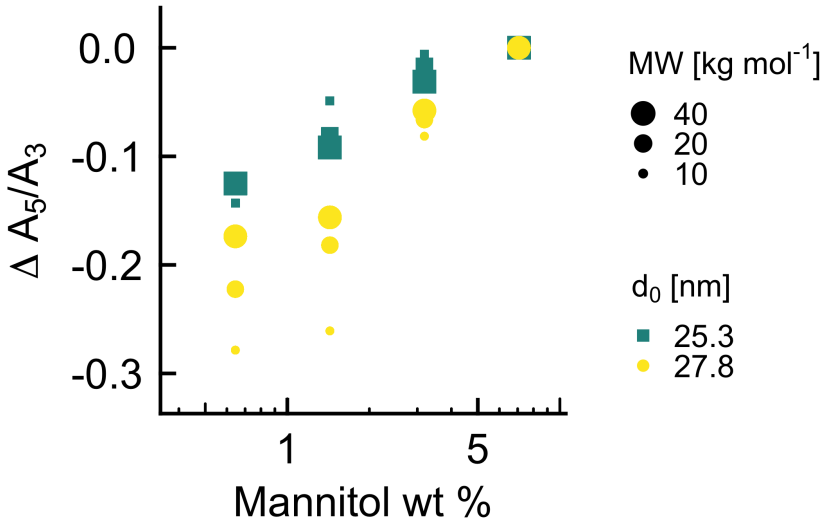

Figure 6.9: Δ A_5/A_3 as a function of mannitol w/w% of two different batches of SPIONs (25.3 and 27.8 nm) and three different molecular weights of PEG (10, 20, and 40 kg mol^{-1}) normalized to A_5/A_3 at the highest mannitol w/w%.

Fig. 6.9 illustrates the significant improvement of magnetic performance for the largest core size, 27.8 nm, with increasing PEG molecular weight. The other core size, 25.3 nm, appears to show inconsistent trends in magnetic performance, but this is expected as increasing the coating molecular weight should most strongly affect the largest core size. The largest core size shows significant increases with increasing PEG molecular weight, including an approximately equal increase as was observed *in vitro*.

These observations reinforce the proposed improvement to magnetic and imaging performance by increasing the steric bulk on the surface of SPIONs. The magnetostatic interaction energy has successfully been reduced to provide an improved signal for equal quantities of SPIONs after internalization and in controlled environments. While there is still a decrease in signal relative to freely dispersed SPIONs in aqueous solution, this is a crucial stepping stone on the way to ensuring SPION performance in biologically relevant environments and the continued development of SPIONs for biomedical applications, in particular, MPI.

6.7 Summary

Based on the results of the previous chapters and the conclusion that magnetostatic interactions dominate changes to SPION performance *in vitro*, a proposed method of improving interparticle separations has been shown here. This method included the increase of the molecular weight of the coatings used to make SPIONs aqueously dispersible. A clear increase in magnetic performance as compared to smaller coating molecular weights has been shown. The increase has been supported by TEM image analysis of interparticle separations after internalization in cells. These results inform the future preparation of SPIONs for biomedical applications such as cell loading and *in vivo* tumor targeting where the consistent performance of SPIONs across different environments is crucial.

Chapter 7

CONCLUSIONS & FUTURE WORK

This work addresses the various factors that contribute to the magnetic performance of SPIONs prepared for MPI after internalization in cells. To accomplish this, SPIONs of appropriate size, size distribution, and crystallographic phase were synthesized and made dispersible in aqueous media and thus biocompatible. They were then exposed to cells, and their resulting response to an alternating magnetic field was observed with noted changes in comparison to those dispersed in only water. Three potential explanations for these changes were examined, including physical changes to the SPION cores, increasing viscosity of the surrounding fluid, and increasing magnetostatic interactions between close-packed SPIONs. The first two of these were dismissed as contributors based on TEM image analysis and no changes observed in magnetic response for experimental and theoretical variation in viscosity. The third factor, magnetostatic interactions, was confirmed as the dominant effect on SPIONs in cells by TEM image analysis of interparticle separations in cells, comparison to the magnetostatic interaction energy and thermal energy, and changes observed in magnetic response for experimental and theoretical variation of interparticle separations. Based on this determination, it is concluded that magnetostatic interactions of SPIONs in cells cause observed changes in magnetic response.

To counter the effect of magnetostatic interactions, methods for improving or recovering the magnetic performance after internalization were explored. The only currently viable method was determined to be control of steric bulk in the coating, and comparison samples were prepared and characterized for magnetic performance. *In vitro* and controlled conditions both show improving magnetic performance with increasing the molecular weight of the polymer coating. These results are supported by TEM image analysis of interparticle separations of

internalized SPIONs. The improvement to MPS performance is accomplished with minimal change in hydrodynamic size, which is vital for continued use *in vivo*.

The work included in this thesis highlights the need to know the behavior of SPIONs in various biological environments to understand their usability as imaging tracers and quantifiability once entering those new environments. As these SPIONs are intended to be used in clinical settings, it is paramount to know if the obtained information is indeed what is expected and interpretable. SPIONs of tailored size with controlled coatings are ideal candidates for cell loading, targeting, and diagnostic applications, and this work informs each of those cases.

The scope of this thesis was limited to *in vitro* cases to limit the potential variability to only that of cells and the environment in which they are cultured. Future studies will be necessary to determine if the internalization and magnetic performance of SPIONs *in vitro* hold true after exposure to the *in vivo* environment. The higher complexity of the *in vivo* environment has the potential to introduce new factors such as non-specific adsorption of proteins and enzymes and a wide variety of cell types with different uptake and material processing behavior that may affect SPION magnetic performance that is not present outside of the body.

LIST OF PUBLICATIONS

E. Teeman, C. Shasha, J. E. Evans & K. M. Krishnan. Intracellular dynamics of superparamagnetic iron oxide nanoparticles for magnetic particle imaging. *Nanoscale* **11**, 7771-7780 (2019).

C. Shasha, **E. Teeman**, and K. M. Krishnan, Nanoparticle core size optimization for magnetic particle imaging, *Phys. Med. Biol.* (Submitted).

R. Hufschmid, **E. Teeman**, B. L. Mehdi, K. M. Krishnan, and N. D. Browning, Observing the Colloidal Stability of Iron Oxide Nanoparticles in situ, *Nanoscale.* (Submitted).

C. Shasha, **E. Teeman**, K. M. Krishnan, P. Szwargulski, T. Knopp & M. Mddel. Discriminating nanoparticle core size using multi-contrast MPI. *Phys. Med. Biol.* **64**, 074001 (2019).

U. M. Engelmann, C. Shasha, **E. Teeman**, I. Slabu & K. M. Krishnan. Predicting size-dependent heating efficiency of magnetic nanoparticles from experiment and stochastic Nel-Brown Langevin simulation. *J. Magn. Magn. Mater.* **471**, 450-456 (2019).

H. Arami, **E. Teeman**, A. Troksa, H. Bradshaw, K. Saatchi, A. Tomitaka, S. S. Gambhir, U. O. Hfeli, D. Liggitt & K. M. Krishnan. Tomographic magnetic particle imaging of cancer targeted nanoparticles. *Nanoscale* **9**, 18723-18730 (2017).

C. Shasha, **E. Teeman** & K. M. Krishnan. Harmonic Simulation Study of Simultaneous Nanoparticle Size and Viscosity Differentiation. *IEEE Magn. Lett.* **8**, 1-5 (2017).

R. Hufschmid, H. Arami, R. M. Ferguson, M. Gonzales, **E. Teeman**, L. N. Brush, N. D. Browning & K. M. Krishnan. Synthesis of phase-pure and monodisperse iron oxide nanoparticles by thermal decomposition. *Nanoscale* **7**, 11142-11154 (2015).

BIBLIOGRAPHY

[1] CDC. Deaths, percent of total deaths, and death rates for the 15 leading causes of death in 5-year age groups, by race and sex: United States. Technical report, 1999.

[2] CDC. Deaths, percent of total deaths, and death rates for the 15 leading causes of death in 5-year age groups, by race and sex: United States. Technical report, 2015.

[3] Tarik F. Massoud and Sanjiv S. Gambhir. Molecular imaging in living subjects: seeing fundamental biological processes in a new light. *Genes Dev.*, 17(5):545–580, mar 2003.

[4] Dokyoon Kim, Jonghoon Kim, Yong Il Park, Nohyun Lee, and Taeghwan Hyeon. Recent Development of Inorganic Nanoparticles for Biomedical Imaging. *ACS Cent. Sci.*, 4(3):324–336, mar 2018.

[5] Xiangjun Han, Ke Xu, Olena Taratula, and Khashayar Farsad. Applications of nanoparticles in biomedical imaging. *Nanoscale*, 11(3):799–819, 2019.

[6] Feng Yang, Chen Jin, Sabin Subedi, Chong Lek Lee, Qiang Wang, Yongjian Jiang, Ji Li, Yang Di, and Deliang Fu. Emerging inorganic nanomaterials for pancreatic cancer diagnosis and treatment. *Cancer Treat. Rev.*, 38(6):566–579, oct 2012.

[7] Lisa Brannon-Peppas and James O. Blanchette. Nanoparticle and targeted systems for cancer therapy. *Adv. Drug Deliv. Rev.*, 64(SUPPL.):206–212, dec 2012.

[8] Krzysztof Sztandera, Michał Gorzkiewicz, and Barbara Klajnert-Maculewicz. Gold Nanoparticles in Cancer Treatment. *Mol. Pharm.*, 16(1):1–23, jan 2019.

[9] Bernhard Gleich and Jürgen Weizenecker. Tomographic imaging using the nonlinear response of magnetic particles. *Nature*, 435(7046):1214–1217, jun 2005.

[10] J. Weizenecker, B. Gleich, J. Rahmer, H. Dahnke, and J. Borgert. Three-dimensional real-time in vivo magnetic particle imaging. *Phys. Med. Biol.*, 54(5):L1–L10, mar 2009.

[11] Patrick William Goodwill, Emine Ulku Saritas, Laura Rose Croft, Tyson N. Kim, Kannan M. Krishnan, David V. Schaffer, and Steven M. Conolly. X-Space MPI: Magnetic Nanoparticles for Safe Medical Imaging. *Adv. Mater.*, 24(28):3870–3877, jul 2012.

[12] A. P. Khandhar, P. Keselman, S. J. Kemp, R. M. Ferguson, P. W. Goodwill, S. M. Conolly, and K. M. Krishnan. Evaluation of PEG-coated iron oxide nanoparticles as blood pool tracers for preclinical magnetic particle imaging. *Nanoscale*, 9(3):1299–1306, 2017.

[13] Julian Haegele, Sarah Vaalma, Nikolaos Panagiotopoulos, Jörg Barkhausen, Florian M. Vogt, Jörn Borgert, and Jürgen Rahmer. Multi-color magnetic particle imaging for cardiovascular interventions. *Phys. Med. Biol.*, 61(16):N415–N426, aug 2016.

[14] Carolyn Shasha, Eric Teeman, Kannan M Krishnan, Patryk Szwargulski, Tobias Knopp, and Martin Möddel. Discriminating nanoparticle core size using multi-contrast MPI. *Phys. Med. Biol.*, 64(7):074001, mar 2019.

[15] Elaine Y. Yu, Prashant Chandrasekharan, Ran Berzon, Zhi Wei Tay, Xinyi Y. Zhou, Amit P. Khandhar, R. Matthew Ferguson, Scott J. Kemp, Bo Zheng, Patrick W. Goodwill, Michael F. Wendland, Kannan M. Krishnan, Spencer Behr, Jonathan Carter, and Steven M. Conolly. Magnetic Particle Imaging for Highly Sensitive, Quantitative, and Safe in Vivo Gut Bleed Detection in a Murine Model. *ACS Nano*, 11(12):12067–12076, dec 2017.

[16] Peter Ludewig, Nadine Gdaniec, Jan Sedlacik, Nils D. Forkert, Patryk Szwargulski, Matthias Graeser, Gerhard Adam, Michael G. Kaul, Kannan M. Krishnan, R. Matthew Ferguson, Amit P. Khandhar, Piotr Walczak, Jens Fiehler, Götz Thomalla, Christian

Gerloff, Tobias Knopp, and Tim Magnus. Magnetic Particle Imaging for Real-Time Perfusion Imaging in Acute Stroke. *ACS Nano*, 11(10):10480–10488, oct 2017.

[17] Ryan Orendorff, Austin J Peck, Bo Zheng, Shawn N Shirazi, R Matthew Ferguson, Amit P Khandhar, Scott J Kemp, Patrick Goodwill, Kannan M Krishnan, George A Brooks, Daniela Kaufer, and Steven Conolly. First in vivo traumatic brain injury imaging via magnetic particle imaging. *Phys. Med. Biol.*, 62(9):3501–3509, may 2017.

[18] Jan Sedlacik, Andreas Frölich, Johanna Spallek, Nils D. Forkert, Tobias D. Faizy, Franziska Werner, Tobias Knopp, Dieter Krause, Jens Fiehler, and Jan-Hendrik Buhk. Magnetic Particle Imaging for High Temporal Resolution Assessment of Aneurysm Hemodynamics. *PLoS One*, 11(8):e0160097, aug 2016.

[19] Elaine Y. Yu, Mindy Bishop, Bo Zheng, R. Matthew Ferguson, Amit P. Khandhar, Scott J. Kemp, Kannan M. Krishnan, Patrick W. Goodwill, and Steven M. Conolly. Magnetic Particle Imaging: A Novel in Vivo Imaging Platform for Cancer Detection. *Nano Lett.*, 17(3):1648–1654, mar 2017.

[20] Hamed Arami, Eric Teeman, Alyssa Troksa, Haydin Bradshaw, Katayoun Saatchi, Asahi Tomitaka, Sanjiv Sam Gambhir, Urs O. Häfeli, Denny Liggitt, and Kannan M. Krishnan. Tomographic magnetic particle imaging of cancer targeted nanoparticles. *Nanoscale*, 9(47):18723–18730, 2017.

[21] Bo Zheng, Tandis Vazin, Patrick W. Goodwill, Anthony Conway, Aradhana Verma, Emine Ulku Saritas, David Schaffer, and Steven M. Conolly. Magnetic Particle Imaging tracks the long-term fate of in vivo neural cell implants with high image contrast. *Sci. Rep.*, 5(1):14055, nov 2015.

[22] Jeff W. M. Bulte, Piotr Walczak, Miroslaw Janowski, Kannan M. Krishnan, Hamed Arami, Aleksi Halkola, Bernhard Gleich, and Jürgen Rahmer. Quantitative Hot-Spot

Imaging of Transplanted Stem Cells Using Superparamagnetic Tracers and Magnetic Particle Imaging. *Tomography*, 1(2):91–97, dec 2015.

[23] Kannan M. Krishnan. *Fundamentals and Applications of Magnetic Materials*. Oxford University Press, aug 2016.

[24] Saqlain A. Shah, Daniel B. Reeves, R. Matthew Ferguson, John B. Weaver, and Kannan M. Krishnan. Mixed Brownian alignment and Néel rotations in superparamagnetic iron oxide nanoparticle suspensions driven by an ac field. *Phys. Rev. B*, 92(9):094438, sep 2015.

[25] Bo Zheng, Kuan Lu, Justin J. Konkle, Daniel W. Hensley, Paul Keselman, Ryan D. Orendorff, Zhi Wei Tay, Elaine Yu, Xinyi Y. Zhou, Mindy Bishop, Beliz Gunel, Laura Taylor, R. Matthew Ferguson, Amit P. Khandhar, Scott J. Kemp, Kannan M. Krishnan, Patrick W. Goodwill, and Steven M. Conolly. Magnetic Particle Imaging. In *Des. Appl. Nanoparticles Biomed. Imaging*, pages 69–93. Springer International Publishing, Cham, 2017.

[26] Matthias Graeser, Tobias Knopp, Patryk Szwargulski, Thomas Friedrich, Anselm von Gladiss, Michael Kaul, Kannan M Krishnan, Harald Ittrich, Gerhard Adam, and Thorsten M. Buzug. Towards Picogram Detection of Superparamagnetic Iron-Oxide Particles Using a Gradiometric Receive Coil. *Sci. Rep.*, 7(1):6872, dec 2017.

[27] Julian Haegele, Kerstin Lüdtke-Buzug, Catharina Schaecke, Matthias Gräser, Robert L. Duschka, Nikolaos Panagiotopoulos, Thorsten M. Buzug, Florian Vogt, and Jörg Barkhausen. Magnetic particle imaging: kinetics of the intravascular signal in vivo. *Int. J. Nanomedicine*, 9:4203, sep 2014.

[28] R. Matthew Ferguson, Amit P. Khandhar, Scott J. Kemp, Hamed Arami, Emine U. Saritas, Laura R. Croft, Justin Konkle, Patrick W. Goodwill, Aleksi Halkola, Jurgen Rahmer, Jorn Borgert, Steven M. Conolly, and Kannan M. Krishnan. Magnetic particle

imaging with tailored iron oxide nanoparticle tracers. *IEEE Trans. Med. Imaging*, 34(5):1077–1084, 2015.

[29] Richard Mathew Ferguson, Amit P Khandhar, Hamed Arami, Loc Hua, Ondrej Hovorka, and Kannan M. Krishnan. Tailoring the magnetic and pharmacokinetic properties of iron oxide magnetic particle imaging tracers. *Biomed. Tech. Eng.*, 58(6):493–507, jan 2013.

[30] Hamed Arami, Amit Khandhar, Denny Liggitt, and Kannan M. Krishnan. In vivo delivery, pharmacokinetics, biodistribution and toxicity of iron oxide nanoparticles. *Chem. Soc. Rev.*, 44(23):8576–8607, 2015.

[31] Kannan M. Krishnan. Biomedical nanomagnetics: A spin through possibilities in imaging, diagnostics, and therapy. *IEEE Trans. Magn.*, 46(7):2523–2558, jul 2010.

[32] Shoji Ohkuma and Brian Poole. Fluorescence probe measurement of the intralysosomal pH in living cells and the perturbation of pH by various agents. *Proc. Natl. Acad. Sci. U. S. A.*, 75(7):3327–31, jul 1978.

[33] Katherine Luby-Phelps. Cytoarchitecture and Physical Properties of Cytoplasm: Volume, Viscosity, Diffusion, Intracellular Surface Area. volume 192, pages 189–221. 1999.

[34] Gorka Salas, Julio Camarero, David Cabrera, Hélène Takacs, María Varela, Robert Ludwig, Heidi Dähring, Ingrid Hilger, Rodolfo Miranda, María Del Puerto Morales, and Francisco José Teran. Modulation of Magnetic Heating via Dipolar Magnetic Interactions in Monodisperse and Crystalline Iron Oxide Nanoparticles. *J. Phys. Chem. C*, 118(34):19985–19994, aug 2014.

[35] J. G. Ovejero, D. Cabrera, J. Carrey, T. Valdivielso, G. Salas, and F. J. Teran. Effects of inter- and intra-aggregate magnetic dipolar interactions on the magnetic heating

efficiency of iron oxide nanoparticles. *Phys. Chem. Chem. Phys.*, 18(16):10954–10963, 2016.

[36] David Cabrera, Annelies Coene, Jonathan Leliaert, Emilio J. Artés-Ibáñez, Luc Dupré, Neil D. Telling, and Francisco J. Teran. Dynamical Magnetic Response of Iron Oxide Nanoparticles Inside Live Cells. *ACS Nano*, page acsnano.7b08995, mar 2018.

[37] Norbert Löwa, Maria Seidel, Patricia Radon, and Frank Wiekhorst. Magnetic nanoparticles in different biological environments analyzed by magnetic particle spectroscopy. *J. Magn. Magn. Mater.*, 427:133–138, apr 2017.

[38] José M. Rojas, Helena Gavilán, Vanesa del Dedo, Eduardo Lorente-Sorolla, Laura Sanz-Ortega, Gustavo B. da Silva, Rocío Costo, Sonia Perez-Yagüe, Marina Talelli, Marzia Marciello, M. Puerto Morales, Domingo F. Barber, and Lucía Gutiérrez. Time-course assessment of the aggregation and metabolization of magnetic nanoparticles. *Acta Biomater.*, 58:181–195, aug 2017.

[39] K. M. Krishnan, A. B. Pakhomov, Y. Bao, P. Blomqvist, Y. Chun, M. Gonzales, K. Griffin, X. Ji, and B. K. Roberts. Nanomagnetism and spin electronics: materials, microstructure and novel properties. *J. Mater. Sci.*, 41(3):793–815, feb 2006.

[40] R Weissleder, DD Stark, BL Engelstad, BR Bacon, CC Compton, DL White, P Jacobs, and J Lewis. Superparamagnetic iron oxide: pharmacokinetics and toxicity. *Am. J. Roentgenol.*, 152(1):167–173, jan 1989.

[41] Yi-Xiang J Wang. Current status of superparamagnetic iron oxide contrast agents for liver magnetic resonance imaging. *World J. Gastroenterol.*, 21(47):13400, nov 2015.

[42] Peter Reimer and Thomas Balzer. Ferucarbotran (Resovist): a new clinically approved RES-specific contrast agent for contrast-enhanced MRI of the liver: properties, clinical development, and applications. *Eur. Radiol.*, 13(6):1266–1276, 2003.

[43] Teresa Pellegrino, Liberato Manna, Stefan Kudera, Tim Liedl, Dmitry Koktysh, Andrey L. Rogach, Simon Keller, Joachim Rädler, Giovanni Natile, and Wolfgang J. Parak. Hydrophobic Nanocrystals Coated with an Amphiphilic Polymer Shell: A General Route to Water Soluble Nanocrystals. *Nano Lett.*, 4(4):703–707, apr 2004.

[44] William W. Yu, Emmanuel Chang, Christie M. Sayes, Rebekah Drezek, and Vicki L. Colvin. Aqueous dispersion of monodisperse magnetic iron oxide nanocrystals through phase transfer. *Nanotechnology*, 17(17):4483–4487, sep 2006.

[45] Marcela Gonzales and Kannan M. Krishnan. Phase transfer of highly monodisperse iron oxide nanocrystals with Pluronic F127 for biomedical applications. *J. Magn. Magn. Mater.*, 311(1):59–62, apr 2007.

[46] Amit P. Khandhar, R. Matthew Ferguson, Julian A. Simon, and Kannan M. Krishnan. Enhancing cancer therapeutics using size-optimized magnetic fluid hyperthermia. *J. Appl. Phys.*, 111(7):10–13, 2012.

[47] Amit P. Khandhar, Gregory J. Wilson, Michael G. Kaul, Johannes Salamon, Caroline Jung, and Kannan M. Krishnan. Evaluating size-dependent relaxivity of PEGylated-USPIOs to develop gadolinium-free T1 contrast agents for vascular imaging. *J. Biomed. Mater. Res. Part A*, 106(9):2440–2447, sep 2018.

[48] Chen Fang, Omid Veiseh, Forrest Kievit, Narayan Bhattarai, Freddy Wang, Zach Stephen, Chun Li, Donghoon Lee, Richard G Ellenbogen, and Miqin Zhang. Functionalization of iron oxide magnetic nanoparticles with targeting ligands: their physicochemical properties and ¡i¿in vivo¡/i¿ behavior. *Nanomedicine*, 5(9):1357–1369, 2010.

[49] Asahi Tomitaka, Hamed Arami, Sonu Gandhi, and Kannan M. Krishnan. Lactoferrin conjugated iron oxide nanoparticles for targeting brain glioma cells in magnetic particle imaging. *Nanoscale*, 7(40):16890–16898, 2015.

[50] U. Schwertmann and R. M. Cornell. *Iron Oxides in the Laboratary*. Wiley-VCH Verlag GmbH, Weinheim, Germany, apr 2000.

[51] Ryan Hufschmid, Hamed Arami, R. Matthew Ferguson, Marcela Gonzales, Eric Teeman, Lucien N. Brush, Nigel D. Browning, and Kannan M. Krishnan. Synthesis of phase-pure and monodisperse iron oxide nanoparticles by thermal decomposition. *Nanoscale*, 7(25):11142–11154, 2015.

[52] Scott J. Kemp, R. Matthew Ferguson, Amit P. Khandhar, and Kannan M. Krishnan. Monodisperse magnetite nanoparticles with nearly ideal saturation magnetization. *RSC Adv.*, 6(81):77452–77464, 2016.

[53] R.E. Rosensweig. Heating magnetic fluid with alternating magnetic field. *J. Magn. Magn. Mater.*, 252(0):370–374, nov 2002.

[54] William T. Coffey and Yuri P. Kalmykov. Thermal fluctuations of magnetic nanoparticles: Fifty years after Brown. *J. Appl. Phys.*, 112(12), 2012.

[55] Carolyn Shasha. *Nonequilibrium nanoparticle dynamics for the development of Magnetic Particle Imaging*. PhD thesis, University of Washington, 2019.

[56] Yuping Bao. *Synthesis, Self-Assembly and Potential Applications of Cobalt-based Nanoparticles with Tailored Magnetic Properties*. PhD thesis, University of Washington, 2006.

[57] Marcela Gonzales-Weyhmiller. *Synthesis, modeling and optimization of iron oxide nanoparticles for magnetic fluid hyperthermia*. Doctor of philosophy, University of Washington, 2007.

[58] Richard Matthew Ferguson. *Tracer design for Magnetic Particle Imaging: modeling, synthesis, and experimental optimization of biocompatible iron oxide nanoparticles*. PhD thesis, University of Washington, 2011.

[59] Amit Praful Khandhar. *Biomedical imaging and therapy with physically and physiologically tailored magnetic nanoparticles*. PhD thesis, University of Washington, 2013.

[60] Hamed Arami. *Magnetic Particle Imaging (MPI) Tracers for In Vivo Applications*. PhD thesis, University of Washington, 2015.

[61] Sonu Gandhi, Hamed Arami, and Kannan M. Krishnan. Detection of Cancer-Specific Proteases Using Magnetic Relaxation of Peptide-Conjugated Nanoparticles in Biological Environment. *Nano Lett.*, 16(6):3668–3674, jun 2016.

[62] A. Bee, R. Massart, and S. Neveu. Synthesis of very fine maghemite particles. *J. Magn. Magn. Mater.*, 149(1-2):6–9, aug 1995.

[63] Young Soo Kang, Subhash Risbud, John F. Rabolt, and Pieter Stroeve. Synthesis and Characterization of Nanometer-Size Fe 3 O 4 and γ-Fe 2 O 3 Particles. *Chem. Mater.*, 8(9):2209–2211, 1996.

[64] D. Eberbeck, F. Wiekhorst, S. Wagner, and L. Trahms. How the size distribution of magnetic nanoparticles determines their magnetic particle imaging performance. *Appl. Phys. Lett.*, 98(18):182502, may 2011.

[65] Taeghwan Hyeon, Su Seong Lee, Jongnam Park, Yunhee Chung, and Hyon Bin Na. Synthesis of Highly Crystalline and Monodisperse Maghemite Nanocrystallites without a Size-Selection Process. *J. Am. Chem. Soc.*, 123(51):12798–12801, dec 2001.

[66] Shouheng Sun and Hao Zeng. Size-Controlled Synthesis of Magnetite Nanoparticles. *J. Am. Chem. Soc.*, 124(28):8204–8205, jul 2002.

[67] William W. Yu, Joshua C. Falkner, Cafer T. Yavuz, and Vicki L. Colvin. Synthesis of monodisperse iron oxide nanocrystals by thermal decomposition of iron carboxylate salts. *Chem. Commun.*, (20):2306, 2004.

[68] Nikhil R. Jana, Yongfen Chen, and Xiaogang Peng. Size- and Shape-Controlled Magnetic (Cr, Mn, Fe, Co, Ni) Oxide Nanocrystals via a Simple and General Approach. *Chem. Mater.*, 16(20):3931–3935, oct 2004.

[69] Jongnam Park, Kwangjin An, Yosun Hwang, Je-Geun Park, Han-Jin Noh, Jae-Young Kim, Jae-Hoon Park, Nong-Moon Hwang, and Taeghwan Hyeon. Ultra-large-scale syntheses of monodisperse nanocrystals. *Nat. Mater.*, 3(12):891–895, dec 2004.

[70] Victor K. LaMer and Robert H. Dinegar. Theory, Production and Mechanism of Formation of Monodispersed Hydrosols. *J. Am. Chem. Soc.*, 72(11):4847–4854, nov 1950.

[71] Erika C. Vreeland, John Watt, Gretchen B. Schober, Bradley G. Hance, Mariah J. Austin, Andrew D. Price, Benjamin D. Fellows, Todd C. Monson, Nicholas S. Hudak, Lorena Maldonado-Camargo, Ana C. Bohorquez, Carlos Rinaldi, and Dale L. Huber. Enhanced Nanoparticle Size Control by Extending LaMer's Mechanism. *Chem. Mater.*, 27(17):6059–6066, sep 2015.

[72] Andrea R. Tao, Susan Habas, and Peidong Yang. Shape Control of Colloidal Metal Nanocrystals. *Small*, 4(3):310–325, mar 2008.

[73] R. A. Sperling and W. J. Parak. Surface modification, functionalization and bioconjugation of colloidal inorganic nanoparticles. *Philos. Trans. R. Soc. A Math. Phys. Eng. Sci.*, 368(1915):1333–1383, mar 2010.

[74] Evelyn L. Rosen, Raffaella Buonsanti, Anna Llordes, April M. Sawvel, Delia J. Milliron, and Brett A. Helms. Exceptionally Mild Reactive Stripping of Native Ligands from Nanocrystal Surfaces by Using Meerwein's Salt. *Angew. Chemie Int. Ed.*, 51(3):684–689, jan 2012.

[75] Michael J. Hostetler, Stephen J. Green, Jennifer J. Stokes, and Royce W. Murray. Monolayers in Three Dimensions: Synthesis and Electrochemistry of ω-Functionalized

Alkanethiolate-Stabilized Gold Cluster Compounds. *J. Am. Chem. Soc.*, 118(17):4212–4213, jan 1996.

[76] Roychelle S. Ingram, Michael J. Hostetler, and Royce W. Murray. Poly-hetero-ω-functionalized Alkanethiolate-Stabilized Gold Cluster Compounds. *J. Am. Chem. Soc.*, 119(39):9175–9178, oct 1997.

[77] J Christopher Love, Lara A Estroff, Jennah K Kriebel, Ralph G Nuzzo, and George M Whitesides. Self-Assembled Monolayers of Thiolates on Metals as a Form of Nanotechnology. *Chem. Rev.*, 105(4):1103–1170, apr 2005.

[78] Marco Lattuada and T. Alan Hatton. Functionalization of Monodisperse Magnetic Nanoparticles. *Langmuir*, 23(4):2158–2168, feb 2007.

[79] T. Sun, M.L.H Chan, C.H Quek, and H. Yu. Improving mechanical stability and density distribution of hepatocyte microcapsules by fibrin clot and gold nano-particles. *J. Biotechnol.*, 111(2):169–177, jul 2004.

[80] Kathleen Davis, Bin Qi, Michael Witmer, Christopher L. Kitchens, Brian A. Powell, and O. Thompson Mefford. Quantitative Measurement of Ligand Exchange on Iron Oxides via Radiolabeled Oleic Acid. *Langmuir*, 30(36):10918–10925, sep 2014.

[81] Hamed Arami and Kannan M. Krishnan. Highly Stable Amine Functionalized Iron Oxide Nanoparticles Designed for Magnetic Particle Imaging (MPI). *IEEE Trans. Magn.*, 49(7):3500–3503, jul 2013.

[82] John D. Gregory. The Stability of N-Ethylmaleimide and its Reaction with Sulfhydryl Groups. *J. Am. Chem. Soc.*, 77(14):3922–3923, jul 1955.

[83] Ryan Hufschmid, Eric Teeman, B. Layla Mehdi, Kannan M. Krishnan, and Nigel D. Browning. Observing the Colloidal Stability of Iron Oxide Nanoparticles in situ. *Nanoscale. (Submitted).*

[84] David B. Williams and C. Barry Carter. *Transmission electron microscopy: A textbook for materials science*. 2009.

[85] Caroline A Schneider, Wayne S Rasband, and Kevin W Eliceiri. NIH Image to ImageJ: 25 years of image analysis. *Nat. Methods*, 2012.

[86] Johannes Schindelin, Ignacio Arganda-Carreras, Erwin Frise, Verena Kaynig, Mark Longair, Tobias Pietzsch, Stephan Preibisch, Curtis Rueden, Stephan Saalfeld, Benjamin Schmid, Jean Yves Tinevez, Daniel James White, Volker Hartenstein, Kevin Eliceiri, Pavel Tomancak, and Albert Cardona. Fiji: An open-source platform for biological-image analysis, 2012.

[87] David Freedman and Persi Diaconis. On the histogram as a density estimator:L 2 theory. *Zeitschrift für Wahrscheinlichkeitstheorie und Verwandte Gebiete*, 57(4):453–476, dec 1981.

[88] R. Chantrell, J. Popplewell, and S. Charles. Measurements of particle size distribution parameters in ferrofluids. *IEEE Trans. Magn.*, 14(5):975–977, sep 1978.

[89] W H. Bragg and W L Bragg. The Reflection of X-rays by Crystals. *Proc. R. Soc. A Math. Phys. Eng. Sci.*, 88(605):428–438, jul 1913.

[90] HE Swanson and E Tatge. Standard X-ray diffraction patterns. *J. Res. Natl. Bur. Stand. (1934).*, 46(4):318, 1951.

[91] D Schulz and G McCarthy, editors. *North Dakota State University*. ICDD Grant-in-Aid, Fargo, North Dakota, USA, grant-in a edition, 1987.

[92] Byung Seok Kwon. *Multilayered magnetic nanoparticles fabricated by nanoimprint lithography for magnetomechanical treatment of cancer*. PhD thesis, University of Washington, 2017.

[93] Malvern Instruments Ltd. Dynamic Light Scattering: An Introduction in 30 Minutes.

[94] Robert Pecora, editor. *Dynamic Light Scattering*. Springer US, Boston, MA, 1985.

[95] D. O. Smith. Development of a VibratingCoil Magnetometer. *Rev. Sci. Instrum.*, 27(5):261–268, may 1956.

[96] Simon Foner. Versatile and Sensitive VibratingSample Magnetometer. *Rev. Sci. Instrum.*, 30(7):548–557, jul 1959.

[97] R. Matthew Ferguson. *Tracer design for Magnetic Particle Imaging: modeling, synthesis, and experimental optimization of biocompatible iron oxide nanoparticles*. PhD thesis, University of Washington, 2011.

[98] Ji Ho Park and Nuri Oh. Endocytosis and exocytosis of nanoparticles in mammalian cells. *Int. J. Nanomedicine*, 9(SUPPL.1):51, may 2014.

[99] Claire Wilhelm and Florence Gazeau. Universal cell labelling with anionic magnetic nanoparticles. *Biomaterials*, 29(22):3161–3174, aug 2008.

[100] R Weissleder, DD Stark, BL Engelstad, BR Bacon, CC Compton, DL White, P Jacobs, and J Lewis. Superparamagnetic iron oxide: pharmacokinetics and toxicity. *Am. J. Roentgenol.*, 152(1):167–173, jan 1989.

[101] Stefaan JH Soenen and Marcel De Cuyper. Assessing iron oxide nanoparticle toxicity in vitro : current status and future prospects. *Nanomedicine*, 5(8):1261–1275, oct 2010.

[102] Justin G. Teeguarden, Paul M. Hinderliter, Galya Orr, Brian D. Thrall, and Joel G. Pounds. Particokinetics in vitro: Dosimetry considerations for in vitro nanoparticle toxicity assessments. *Toxicol. Sci.*, 95(2):300–312, 2007.

[103] Amit Praful Khandhar. *Biomedical imaging and therapy with physically and physiologically tailored magnetic nanoparticles*. Doctor of philosophy, University of Washington, 2013.

[104] Joseph A. Mindell. Lysosomal Acidification Mechanisms. *Annu. Rev. Physiol.*, 74(1):69–86, mar 2012.

[105] Michael Levy, Nathalie Luciani, Damien Alloyeau, Dan Elgrabli, Vanessa Deveaux, Christine Pechoux, Sophie Chat, Guillaume Wang, Nidhi Vats, François Gendron, Cécile Factor, Sophie Lotersztajn, Alain Luciani, Claire Wilhelm, and Florence Gazeau. Long term in vivo biotransformation of iron oxide nanoparticles. *Biomaterials*, 32(16):3988–3999, jun 2011.

[106] Morris John Karnovsky. A formaldehyde-glutaraldehyde fixative of high osmolarity for use in electron microscopy. *J. Cell Biol.*, 1965.

[107] Hamed Arami and Kannan M. Krishnan. Intracellular performance of tailored nanoparticle tracers in magnetic particle imaging. *J. Appl. Phys.*, 115(17):17B306, may 2014.

[108] Carolyn Shasha, Eric Teeman, and Kannan M. Krishnan. Harmonic Simulation Study of Simultaneous Nanoparticle Size and Viscosity Differentiation. *IEEE Magn. Lett.*, 8:1–5, 2017.

[109] T.L. Gilbert. Classics in Magnetics A Phenomenological Theory of Damping in Ferromagnetic Materials. *IEEE Trans. Magn.*, 40(6):3443–3449, nov 2004.

[110] Gabriel T. Landi. Role of dipolar interaction in magnetic hyperthermia. *Phys. Rev. B*, 89(1):014403, jan 2014.

[111] N. A. Usov and B. Ya Liubimov. Dynamics of magnetic nanoparticle in a viscous liquid: Application to magnetic nanoparticle hyperthermia. *J. Appl. Phys.*, 112(2):023901, jul 2012.

[112] Daniel B. Reeves and John B. Weaver. Combined Néel and Brown rotational Langevin dynamics in magnetic particle imaging, sensing, and therapy. *Appl. Phys. Lett.*, 107(22):223106, nov 2015.

[113] L. W. Bosart and A. O. Snoddy. Specific Gravity of Glycerol. *Ind. Eng. Chem.*, 20(12):1377–1379, dec 1928.

[114] P. Linstrom and W. Mallard. NIST standard reference database, 2005.

[115] Nian-Sheng Cheng. Formula for the Viscosity of a GlycerolWater Mixture. *Ind. Eng. Chem. Res.*, 47(9):3285–3288, may 2008.

Appendix A

SYNTHESIS OF IRON OLEATE

A.1 Purpose

To prepare the organometallic precursor necessary in the thermal decomposition method of iron oxide nanoparticle synthesis.

A.2 Materials

A.2.1 Chemicals

Iron trichloride hexahydrate, sodium oleate, deionized water, hexanes, ethanol, sodium sulfate (anhydrous)

A.2.2 Equipment

DigiTrol II temperature controller, type-K thermocouple, erlenmeyer flask, 1 L three-neck round bottom flask, 1-1/2 × 5/8 inch Teflon coated magnetic stir bar, glass funnel, qualitative filter paper, 1 L separatory funnel, 1 L round bottom flask, rotary evaporator, vacuum pump, condenser column, 250 mL 24/40 bump bulb, and 250 mL erlenmeyer flask, stir plate

A.2.3 Reagents

Iron chloride solution

1. Weigh required mass of iron chloride
2. Transfer to 250 mL erlenmeyer flask
3. Add appropriate size stir bar

4. Add required volume of deionized water
5. Cover opening with aluminum foil
6. Stir at 150 rpm for 30 min or until fully dissolved

Sodium oleate solution

1. Place glass stopper in left neck of three-neck flask
2. Place 24/40 SubaSeal septum in right neck of three-neck flask
3. Add appropriate size stir bar
4. Add funnel to center neck of three-neck flask
5. Add required mass of sodium oleate to three-neck flask through funnel
6. Add required volume of hexanes
7. Add thermocouple through SubaSeal septum
8. Stir at 500 rpm to disperse sodium oleate
9. Add required volume of ethanol
10. Add required volume of deionized water dropwise over a minimum of two minutes

A.3 Reflux

1. Heat sodium oleate solution to 40 °C slowly
    - Set DigiTrol II to approximately 4.0% power initially and slowly increase until at desired temperature
2. Once sodium oleate is fully dissolved, transfer iron chloride solution to three-neck flask
3. Add condensor column to center neck of three-neck flask
4. Add water connections to top and bottom of condensor column

5. Start water flow through condensor column
6. Purge with argon from a needle through SubaSeal septum for at least 2 min
7. Remove purge needle and start argon flow through outlet adaptor
8. Heat to 57 °C and wait for reflux to be at a consistent rate
   - Set DigiTrol II to approximately 7.8% power to achieve desired temperature
   - Using temperature set point mode will unevenly heat and damage iron oleate
9. Allow reaction to reflux for 4 h from time reflux begins
10. After 4 h, turn off heating mantle and remove it from under reaction flask
11. Allow reaction to cool to at least 50 °C

A.4 Extraction

1. Transfer reaction product to 1 L separatory funnel with glass funnel
2. Allow phases to separate
3. Remove bottom (aqueous) layer
4. Add appropriate amount of deionized water
   - Approximately 75 mL for 40 mM scale
5. Shake vigorously for 10 s
6. Allow phases to separate
7. Remove bottom (aqueous) layer
8. Repeat previous four steps twice more

A.5 Drying

1. Collect organic ("red") layer in erlenmeyer flask
2. Add appropriate amount of sodium sulfate
   - Approximately 30 g for 40 mM scale
3. Swirl or stir with large stir bar for 10 min
4. Obtain tare weight of empty 1 L round bottom flask
5. Transfer to 1 L round bottom flask with glass funnel and collecting sodium sulfate with qualitative filter paper
6. Wash remaining iron oleate through filter paper with hexanes
   - Sodium sulfate should contain no "red" coloring after washing process

A.6 Rotatory Evaporation

1. Attach clean bump bulb to rotary evaporator
2. Attach flask with iron oleate and hexanes to bump bulb
3. Begin rotation at $\leq$ 100 rpm
4. Set bath temperature to 20 °C
5. Place under low vacuum with water aspiration system
   - Do not leave vacuum open or hexanes will evaporate too quickly and violently
   - "Swinging" through the open state while observing evaporation rate as noted by drop rate of hexanes from cold trap
6. Once evaporation slows, leave vacuum open for increasing amounts of time
7. Once vacuum can be left open continuously, increase bath temperature to 30 °C

8. Once evaporation appears to stop or recycling solvent through cold trap and collection flask occurs, vent and empty collection flask
9. Place under vacuum again with water aspiration system
10. Leave vacuum open for 10 to 15 min
11. Close vacuum opening and switch vacuum system to high vacuum line
12. Slowly open vacuum
    - Be careful to open slowly and watch for bubble formation from viscous iron oleate
    - Do not allow iron oleate to enter rotatory evaporator
13. Once able to fully leave under high vacuum, wait 10 to 15 min
14. Close vacuum lines and vent rotatory evaporator
15. Turn off vacuum pump and empty collection flask

A.7 Vacuum drying

1. Place round bottom flask containing iron oleate under high vacuum for at least 2 h
    - Overnight is preferred
    - Watch for large bubble formation and do not allow iron oleate to enter vacuum line
2. Remove from vacuum line and determine weight of 1 L round bottom flask with iron oleate
3. Calculate final iron oleate mass

Appendix B

PURIFICATION AND PHASE TRANSFER OF SPIONS

B.1 Purpose

To remove synthesis by-products and excess organic material from as-synthesized iron oxide nanoparticles and transfer purified hydrophobic nanoparticles from organic solvent to aqueous solution.

B.2 Materials

B.2.1 Chemicals

As-synthesized iron oxide nanoparticles, hexanes, ethyl acetate, acetone, chloroform, deionized water, buffer (1X PBS, 1X TAE, 0.005 M NaOH, etc)

B.2.2 Equipment/Supplies

Glass vial w/ rubber septum cap, pasteur pipet, ultrasonic bath, neodymium magnet, stir bar, rotary evaporator, vacuum pump, amicon filter, PD-10 column

B.3 Purification

1. Thaw as-synthesized nanoparticle stock solution at room temperature
   - As-synthesized nanoparticles are stored in the $-80\,^{\circ}\mathrm{C}$ freezer, $-20\,^{\circ}\mathrm{C}$ freezer, or $4\,^{\circ}\mathrm{C}$ fridge
2. Label and obtain the tare weight of a glass vial
3. Transfer as-synthesized nanoparticles to vial

   - About 1 mL per 10 mL of vial volume

4. Add ethyl acetate to vial
   - About 3 mL per 1 mL as-synthesized nanoparticles
5. Cap vial and sonicate for 30 to 60 s
6. Place vial adjacent to neodymium magnet until nanoparticles fully come out of solution
7. With vial still on magnet, remove supernatant as fully as possible
8. Add hexanes and ethyl acetate to vial
   - About 1 mL hexanes and 3 mL ethyl acetate per 1 mL as-synthesized nanoparticles
9. Cap vial and sonicate for 30 to 60 s
10. Place vial on neodymium magnet until nanoparticles fully come out of solution
11. With vial still on magnet, remove supernatant as fully as possible
12. Add hexanes and acetone to vial
    - About 1 mL hexanes and 1.5 mL acetone per 1 mL as-synthesized nanoparticles
13. Cap vial and sonicate for 1 min
14. Place vial on neodymium magnet until nanoparticles fully come out of solution
15. With vial still on magnet, remove supernatant as fully as possible
16. Repeat previous four steps three to four times
17. Dry nanoparticles under inert gas flow
18. Dry under high vacuum for a minimum of 2 h
    - Overnight is preferred

19. Get weight of glass vial and dried nanoparticles
20. Add chloroform to vial
    - About 1 mL chloroform per 1 mg nanoparticles
21. If more than 12 mg of nanoparticles, split solution into two vials
    - Label vials with letters after notebook-page identifier
    - Example: 3-033 A & 3-033 B

B.4 Phase Transfer

1. Select polymer for desired nanoparticle application
2. Weigh polymer
3. Add polymer to glass vial with dispersed nanoparticles
    - It is advised to use ratios chosen based on nanoparticle core size and molecular weight of the chosen polymer
    - As a fall back, use 8 to 10 mg polymer per 1 mg dried nanoparticles
4. Cap vial and sonicate thoroughly
    - Solution should have no aggregates and be a transparent brown-black color
    - Proceed to next step after maximum 10 to 15 min sonication, some polymers take longer to disperse
5. Add small stir bar to vial
6. Cap vial and stir at high speed (1200 rpm) for one to two days
    - Cover sample with aluminum foil if polymer is light sensitive

7. Remove stir bar by magnet
8. Rotovap sample until chloroform fully evaporates
    - Typical parameters for $\leq$ 10 mL of chloroform are 30 °C at 280 rpm for 45 to 60 min
9. Dry under high vacuum for a minimum of 2 h
    - Overnight is preferred
10. Add deionized water/buffer to vial
    - About 1 mL per 1 mg nanoparticles
11. Sonicate for 1 to 2 h
    - Check quality of dispersed nanoparticles by DLS
    - Some phase transfers may require longer sonication times
12. Place vial on neodymium magnet for 30 min
13. Collect supernatant
14. Measure DLS, VSM, and MPS for sample
    - DLS Z-avg size should at least be <90 nm
    - DLS volume distribution should only show one peak with minimal "shoulder" at higher sizes
    - VSM hysteresis loop should be closed loop (superparamagnetic)
15. Nanoparticles can be concentrated by high speed centrifugation and re-dispersion in smaller volume water/buffer or with centrifugal filters
16. Sample should be purified by PD-10 column and 0.2 µm filtered before use in biological studies

B.5 Example Table

Vial	Tare [g]	Vial w/ NP [g]	NP [mg]	Polymer [mg]	Chloroform [mL]
A	16.8956	16.9046	9.0	93.7	9
B	16.7681	16.7769	8.8	88.7	9
...					

Appendix C

CHEMICAL FIXATION, OSMIUM FIXATION, AND RESIN EMBEDDING OF CELLS

C.1 Purpose

To embed and preserve cellular material in resin for electron microscopy. This protocol is based on the Mollenhauer Embedding Method and Luft Technique.

C.2 Materials

C.2.1 Chemicals

Deionized water, Acetone, Paraformaldehyde powder, 0.2 M Cacodylate buffer, 50% glutaraldehyde solution, 10X PBS, 1 M NaOH, 4% Osmium Tetroxide solution, Poly/Bed 812, Araldite 502, Dodecenylsuccinic anhydride (DDSA), DMP-30

C.2.2 Equipment

Stir/hot plate, vortex w/ and w/o centrifuge tube adaptor, vacuum pump

C.2.3 Reagents

8% Paraformaldehyde Solution

1. Add 8 g of paraformaldehyde resin to 70 mL of distilled water
2. Heat to 60 °C (no higher)
3. Add 1 M NaOH until the solution clears, usually a couple of drops
4. Cool to room temperature

5. Add 9 mL of 10X PBS or 30 mL of 0.3 M PBS
6. Adjust pH to 7.4
7. Filter
8. Store at 4 °C

Karnovsky's Fixative

1. Add 12.5 mL of 8% paraformaldehyde solution to a 100 mL bottle
2. Add 2.5 mL of 50% glutaraldehyde solution
3. Add 25 mL of 0.2 M cacodylate buffer
4. Add 10 mL of deionized water
5. Stir well
6. Adjust pH to 7.4
7. Filter
8. Store at 4 °C

Dehydration Dilutions

1. Add desired mass deionized water 20 mL scintillation vial
2. Add desired acetone mass
3. Mix water and acetone with vortex at 3000 rpm

	mass [g]			
Component	50%	70%	90%	100%
DI Water	10.00	6.00	2.00	0.00
Acetone	10.00	14.00	18.00	20.00

Resin Dilutions

1. Add desired mass of Poly/Bed, Araldite, DDSA, and DMP-30 20 mL scintillation vial
2. Add desired acetone mass
3. Mix resin and acetone with vortex at 3000 rpm
4. Degas mixture with vacuum, if necessary

		mass [g]			
Resin %	Component	33%	50%	67%	100%
29.41	PolyBed	1.76	2.65	3.53	5.29
16.18	Araldite	0.97	1.46	1.94	2.91
52.94	DDSA	3.18	4.76	6.35	9.53
1.47	DMP-30	0.09	0.13	0.18	0.26
	Acetone	12.00	9.00	6.00	0.00

C.3 Cell Collection & Agarose Embedding

1. Add 100 µL 0.25% Trypsin-EDTA per 1 mL well volume
2. Collect cells in 1.5 mL centrifuge tube
3. Centrifuge at 500 rcf for 5 min to pellet
4. Remove supernatant
5. Add 100 µL 1% low-melting-point agarose
6. Centrifuge at 1500 rcf for 5 min to pellet
7. Cool at 4 °C for 30 min to solidify agarose

C.4 Chemical Fixation & Agarose Block Trimming

1. Add 1 mL Karnovsky's fixative
2. Shake overnight at 100 rpm
3. Remove supernatant
4. Add 1 mL deionized water
5. Remove agarose block from tube
6. Cut to contain only cell pellet
7. Place agarose and cell pellet into new centrifuge tube

C.5 Osmium Fixation & Dehydration

– Centrifuge at 1500 rcf for 1 min to pellet whenever necessary

1. Add 500 µL 1% OsO_4
2. Shake for 3 h at 100 rpm
3. Remove supernatant
4. Add 500 µL of 50% acetone/50% deionized water
5. Shake overnight at 100 rpm
6. Remove supernatant
7. Add 500 µL of 70% acetone/30% deionized water
8. Shake for 2 h at 100 rpm
9. Remove supernatant
10. Add 500 µL of 90% acetone/10% deionized water
11. Shake for 2 h at 100 rpm

12. Remove supernatant
13. Add 500 µL of 100% acetone
14. Shake for 2 h at 100 rpm
15. Remove supernatant
16. Add 500 µL of 100% acetone
17. Shake for 2 h at 100 rpm

C.6 Resin Infiltration

– Centrifuge at 1500 rcf for 1 min to pellet whenever necessary

1. Remove supernatant
2. Add 1 mL of 33% resin/67% acetone
3. Shake for 1 h at 100 rpm
4. Remove supernatant
5. Add 1 mL of 50% resin/50% acetone
6. Shake for 1 h at 100 rpm
7. Remove supernatant
8. Add 1 mL of 67% resin/33% acetone
9. Shake for 1 h at 100 rpm
10. Remove supernatant
11. Add 1 mL of 100% resin
12. Shake for 4 h at 100 rpm

C.7 Curing

- Transfer sample to an appropriate plastic capsule/tube, if necessary
- Centrifuge at 1500 rcf for 1 min to pellet whenever necessary

1. Incubate sample in an oven at 35 °C overnight
2. Incubate sample in an oven at 45 °C for 24 h
3. Incubate sample in an oven at 60 °C for 24 h
    - Incubation times longer than 24 h at 60 °C are acceptable

Appendix D

IMAGEJ MACRO FOR PARTICLE SIZE ANALYSIS

```
macro_name   = "ParticleSizeAnalyzer, PSA_dev.txt (trunk).
    http://code.google.com/p/psa-macro/" ;
macro_info   = "2010-01-17 Ralph Sperling <ralph.sperling.icn@uab.es>, Institut
    Catal de Nanotecnologia (ICN), Barcelona, Spain. http://www.nanocat.org";
macro_license = "GNU General Public License v3,
    http://www.gnu.org/licenses/gpl.html"
macro_comment = "Little corrections, as removing the scale bar after auto finder
    in preprocessed image instead of in original image";

requires("1.43n");  //  not really, but let's get a recent version..
// 1.43n was the last version in 2009. It got rid of the the message asking to
    save changes, even if image has been saved by macro before.
// See ImageJ News about updated versions: http://rsbweb.nih.gov/ij/notes.html

FULL_AUTO_MODE = false; // set true to skip configuration dialogues

// =======================================================

// ---------------------- Get options from preferences, or set to default values

// Apparently, there is no "parseBoolean()" in the macro language..
function parseBoolean(boolstring){
    if (boolstring == "true" || boolstring == true || boolstring == "1" ||
        boolstring == 1){
        return(true);
    }
    else return(false);
}

choose_scale = newArray("NONE", "Position from last run", "Bottom left", "Bottom
    right", "TEM at UAB", "TEM at PCB", "TEM at PCB (large bar)", "TEM at PCB
    (auto find)");
oScalehelp = call("ij.Prefs.get", "PSA.scalehelp", "Position from last run");
```

```
choose_background=newArray("NONE", "Inverted Gaussian (10% image size)","Rolling
    Ball (10% image size)","Rolling Ball (r = 50 px)");
oRemoveBG  = call("ij.Prefs.get", "PSA.removeBG", "NONE");

choose_smoothing = newArray("NONE", "Median r = 1 (3x3)", "Median r = 2 (5x5)",
    "Median r = 3 (7x7)", "Gaussian r = 1", "Gaussian r = 2", "Gaussian r = 3");
// removed mean (Gaussian neither recommended): "Mean r = 1 (3x3)", "Mean r = 2
    (5x5)", "Mean r = 3 (7x7)"
oSmooth = call("ij.Prefs.get", "PSA.smooth", "Median r = 1 (3x3)");

choose_thresh = newArray("Manual (interactive)", "Automatic (ImageJ)",
    "Hysteresis (connectionthresholding*)", "Triangle (auto_threshold*)");
oThresh = call("ij.Prefs.get", "PSA.thresh", "Manual (interactive)");

choose_watershed = newArray("NONE", "Watershed filter");
oWatershed = call("ij.Prefs.get", "PSA.watershed", "Watershed filter");

oDiamMin = parseFloat(call("ij.Prefs.get", "PSA.diamMin", "2"));
oDiamMax = parseFloat(call("ij.Prefs.get", "PSA.diamMax", "999"));
oCircMin = parseFloat(call("ij.Prefs.get", "PSA.circMin", "0.8"));
oCircMax = parseFloat(call("ij.Prefs.get", "PSA.circMax", "1.0"));

oOutlineExcluded = parseBoolean(call("ij.Prefs.get", "PSA.outlineExcluded",
    "true"));

oTableExcluded = parseBoolean(call("ij.Prefs.get", "PSA.tableExcluded", "true"));

oShowOtherParameters = false; // do not save this setting, i.e. the choice to
    configure more options


// ---------------------- Second window
oScaleunit = call("ij.Prefs.get", "PSA.scaleUnit", "nm");

oDarkBG = parseBoolean(call("ij.Prefs.get", "PSA.darkBG", "false"));

oSavePrepro = parseBoolean(call("ij.Prefs.get", "PSA.savePreprocessed",
    "false"));

//  Minimum size even for for excluded particles, everything smaller is assumed
    as noise
oSizeNoise = parseFloat(call("ij.Prefs.get", "PSA.sizeNoise", "1.0"));
```

```
oSaveResults   = parseBoolean(call("ij.Prefs.get", "PSA.saveResultsTable",
    "true"));

choose_histo   = newArray("0 - 50 nm / 0.5", "0 - 50 nm / 1.0", "0 - 100 nm /
    0.5", "0 - 100 nm / 1.0", "Automatic Binning", "NONE");
oHistShow      = call("ij.Prefs.get", "PSA.histoShow", "0 - 50 nm / 0.5");

oHistSavePNG   = parseBoolean(call("ij.Prefs.get", "PSA.histoSavePNG", "true"));

oHistSaveTXT   = parseBoolean(call("ij.Prefs.get", "PSA.histoSaveTXT", "false"));

oCalcCubes     = parseBoolean(call("ij.Prefs.get", "PSA.calculateCubes",
    "false"));

choose_merge   = newArray("Original image", "Preprocessed image");
oMergeOutlines = call("ij.Prefs.get", "PSA.outlinedMergeWith", "Original image");

oSaveOutlines  = parseBoolean(call("ij.Prefs.get", "PSA.saveOutlined", "true"));

oLogfile       = parseBoolean(call("ij.Prefs.get", "PSA.saveLogfile", "true"));

oSaveOver      = parseBoolean(call("ij.Prefs.get", "PSA.saveOverExisting",
    "true"));


// ---------------------- Here, configure some HIDDEN OPTIONS not appearing in
    the dialog:
oStepwiseMode = false; // for debugging, pops up a waiting message after each
    step (somewhat annoying feature..)
oWritesetfile = false;  // write settings from dialog to file

// Now all parameters should be preset



// =====================================================

if (FULL_AUTO_MODE == true){ // set some key parameters to automatic behaviour,
    another if clause below will close all windows
    oScalehelp = "NONE";
    oThresh = "Automatic (ImageJ)";
}
else {  // START WITH DIALOG
```

```
// ---------------------- Dialog asking user for options

Dialog.create("ParticleSizeAnalyzer");
//Dialog.addMessage(macro_name);
Dialog.addMessage("Designed for TEM images of nanoparticles\nCalculates the
    area-equivalent diameter of particles.");

Dialog.addChoice("Help with scaling (interactive)", choose_scale, oScalehelp);

Dialog.addChoice("Background removal", choose_background, oRemoveBG);
Dialog.addChoice("Smoothing filter", choose_smoothing, oSmooth);

Dialog.addMessage("..:: Segmentation and Analysis (* needs plugin installed)
    ::..");
Dialog.addChoice("Thresholding mode", choose_thresh, oThresh);
Dialog.addChoice("Separation of touching particles", choose_watershed,
    oWatershed);
Dialog.addNumber("Minimum diameter", oDiamMin);
Dialog.addNumber("Maximum diameter", oDiamMax);
Dialog.addNumber("Minimum circularity", oCircMin);
Dialog.addNumber("Maximum circularity", oCircMax);

Dialog.addCheckbox("Outline excluded particles, too", oOutlineExcluded);
Dialog.addCheckbox("Add excluded particles to results table (without saving
    these)", oTableExcluded);
Dialog.addCheckbox("Configure less used options...", oShowOtherParameters);

Dialog.show();


// Now, get options and immediately write back to preferences
oScalehelp = Dialog.getChoice(); call("ij.Prefs.set", "PSA.scalehelp",
    oScalehelp);
oRemoveBG  = Dialog.getChoice(); call("ij.Prefs.set", "PSA.removeBG",
    oRemoveBG);
oSmooth    = Dialog.getChoice(); call("ij.Prefs.set", "PSA.smooth", oSmooth);

oThresh    = Dialog.getChoice(); call("ij.Prefs.set", "PSA.thresh", oThresh);
oWatershed = Dialog.getChoice(); call("ij.Prefs.set", "PSA.watershed",
    oWatershed);
oDiamMin   = Dialog.getNumber(); call("ij.Prefs.set", "PSA.diamMin",
    oDiamMin);
oDiamMax   = Dialog.getNumber(); call("ij.Prefs.set", "PSA.diamMax",
    oDiamMax);
```

```
oCircMin   = Dialog.getNumber(); call("ij.Prefs.set", "PSA.circMin",
    oCircMin);
oCircMax   = Dialog.getNumber(); call("ij.Prefs.set", "PSA.circMax",
    oCircMax);

oOutlineExcluded   = Dialog.getCheckbox(); call("ij.Prefs.set",
    "PSA.outlineExcluded", oOutlineExcluded);
oTableExcluded     = Dialog.getCheckbox(); call("ij.Prefs.set",
    "PSA.tableExcluded", oTableExcluded);
oShowOtherParameters = Dialog.getCheckbox(); call("ij.Prefs.set",
    "PSA.showOtherParameters", oShowOtherParameters);


// ---------------------- Second screen with less-used options:
if (oShowOtherParameters){
    Dialog.create("ParticleSizeAnalyzer (more options)");

    Dialog.addString("Scale unit (e.g. nm)", oScaleunit);
    Dialog.addMessage("When outlining particles smaller than minimum
        diameter:");
    Dialog.addNumber("Maximum size considered noise", oSizeNoise);


    Dialog.addCheckbox("Light particles on dark background", oDarkBG);
    Dialog.addCheckbox("Save image after preprocessing", oSavePrepro);

    Dialog.addCheckbox("Calculations and histogram for cubic particles",
        oCalcCubes);


    Dialog.addCheckbox("Save results table as text file", oSaveResults);
    Dialog.addCheckbox("Save histogram image as PNG", oHistSavePNG);
    Dialog.addCheckbox("Save histogram data as TXT", oHistSaveTXT);
    Dialog.addChoice("Show diameter histogram", choose_histo, oHistShow);


    Dialog.addChoice("Merge outlined particles with", choose_merge,
        oMergeOutlines);
    Dialog.addCheckbox("Save image with outlined particles", oSaveOutlines);
    Dialog.addCheckbox("Save parameters in logfile", oLogfile);
    Dialog.addCheckbox("Save over existing macro output files (no
        timestamping)", oSaveOver);

    Dialog.show();
```

```
        oScaleunit     = Dialog.getString;   call("ij.Prefs.set", "PSA.scaleUnit",
            oScaleunit);
        //  Minimum size even for for excluded particles, everything smaller is
            assumed as noise
        oSizeNoise     = Dialog.getNumber;   call("ij.Prefs.set", "PSA.sizeNoise",
            oSizeNoise);


        oDarkBG        = Dialog.getCheckbox; call("ij.Prefs.set", "PSA.darkBG",
            oDarkBG);
        oSavePrepro    = Dialog.getCheckbox; call("ij.Prefs.set",
            "PSA.savePreprocessed", oSavePrepro);

        oCalcCubes     = Dialog.getCheckbox; call("ij.Prefs.set",
            "PSA.calculateCubes", oCalcCubes);


        oSaveResults   = Dialog.getCheckbox; call("ij.Prefs.set",
            "PSA.saveResultsTable", oSaveResults);
        oHistSavePNG   = Dialog.getCheckbox; call("ij.Prefs.set",
            "PSA.histoSavePNG", oHistSavePNG);
        oHistSaveTXT   = Dialog.getCheckbox; call("ij.Prefs.set",
            "PSA.histoSaveTXT", oHistSaveTXT);
        oHistShow      = Dialog.getChoice;   call("ij.Prefs.set", "PSA.histoShow",
            oHistShow);

        oMergeOutlines = Dialog.getChoice;  call("ij.Prefs.set",
            "PSA.outlinedMergeWith", oMergeOutlines);
        oSaveOutlines  = Dialog.getCheckbox; call("ij.Prefs.set",
            "PSA.saveOutlined", oSaveOutlines);
        oLogfile       = Dialog.getCheckbox; call("ij.Prefs.set",
            "PSA.saveLogfile", oLogfile);
        oSaveOver      = Dialog.getCheckbox; call("ij.Prefs.set",
            "PSA.saveOverExisting", oSaveOver);
    }

} // close != FULL_AUTO_MODE block for interactive behaviour

// =====================================================
// ---------------------- Housekeeping
```

```
run("Appearance...", " antialiased menu=12"); // Turn off interpolation to see
    only real pixels when zooming
removeScalebar = false; // default value, scale bar can bee set up to be
    automatically found and removed after scaling the image


imgtitle   = getTitle();
index = lastIndexOf(imgtitle, ".");
if (index!=-1) imgtitle = substring(imgtitle, 0, index); // remove suffix
titlebase = imgtitle;

imgID      = getImageID();
filedir    = split(getDirectory("image"),"\n");
imgdir     = filedir[0];
imgwidth   = getWidth(); // this is in pixels
imgheight  = getHeight();


// make timestamp string, taken from macro GetDateAndTime.txt
getDateAndTime(year, month, dayOfWeek, dayOfMonth, hour, minute, second, msec);
    TimeString=""+year+"-";
  if ((month+1)<10){TimeString=TimeString+"0";}
    TimeString = TimeString+(month+1)+"-";  //  don't know why, always get one
        month less :-/ a bug?
  if (dayOfMonth<10) {TimeString = TimeString+"0";}
    TimeString = TimeString+dayOfMonth+"_";
  if (hour<10) {TimeString = TimeString+"0";}
    TimeString = TimeString+hour+"h";
  if (minute<10) {TimeString = TimeString+"0";}
    TimeString = TimeString+minute+"m";
  if (second<10) {TimeString = TimeString+"0";}
    TimeString = TimeString+second+"s";


if (! oSaveOver){     // do not put timestamp, i.e. overwrite files if already
    there from precedent run
    titlebase = titlebase+"_"+TimeString;
}

if (oMergeOutlines == "Preprocessed image"){
    oSavePrepro = true; // image has to be reloaded because proprocessed image
        will be further used as mask
}
```

```
if (oSavePrepro){
    preprofile = imgdir+titlebase+"_preprocessed.png";
}

// ---------------------- Write settings to file, may help to debug input from
    GUI

if (oWritesetfile){
    setfile = File.open(imgdir+titlebase+"_settings.txt");
    if (FULL_AUTO_MODE == true){ print(setfile, "FULL_AUTO_MODE = True");}
    print(setfile, "oScalehelp = " + oScalehelp);
    print(setfile, "oRemoveBG = " + oRemoveBG);
    print(setfile, "oSmooth = " + oSmooth);
    print(setfile, "oThresh = " + oThresh);
    print(setfile, "oWatershed = " + oWatershed);
    print(setfile, "oDiamMin = " + oDiamMin);
    print(setfile, "oDiamMax = " + oDiamMax);
    print(setfile, "oCircMin = " + oCircMin);
    print(setfile, "oCircMax = " + oCircMax);
    print(setfile, "oOutlineExcluded = " + oOutlineExcluded);
    print(setfile, "oTableExcluded = " + oTableExcluded);
    print(setfile, "oShowOtherParameters = " + oShowOtherParameters);

    print(setfile, "oScaleunit = " + oScaleunit);
    print(setfile, "oDarkBG = " + oDarkBG);
    print(setfile, "oStepwiseMode = " + oStepwiseMode);
    print(setfile, "oSavePrepro = " + oSavePrepro);
    print(setfile, "oSizeNoise = " + oSizeNoise);
    print(setfile, "oSaveResults = " + oSaveResults);
    print(setfile, "oHistShow = " + oHistShow);
    print(setfile, "oHistSavePNG = " + oHistSavePNG);
    print(setfile, "oHistSaveTXT = " + oHistSaveTXT);
    print(setfile, "oMergeOutlines = " + oMergeOutlines);
    print(setfile, "oSaveOutlines = " + oSaveOutlines);
    print(setfile, "oLogfile = " + oLogfile);
    print(setfile, "oSaveOver = " + oSaveOver);

    File.close(setfile);
}

// ========================================================

// ---------------------- Set scale
```

```
getPixelSize(unit, pWidth, pHeight, pDepth); // These are the values if scale
    etc is not set otherwise later
// print("unit: ", unit);    // log
// print("pWidth: ", pWidth);
// print("pHeight: ", pHeight);
// print("pDepth: ", pDepth);


if (unit=="microns"){    // change scale to nm if found in microns, e.g. in
    Gatan .dm3 format
  run("Set Scale...", "known=1000 pixel=1 unit=nm");
}

if (oScalehelp == "Position from last run"){  // get saved values and draw line
    for scale bar
    scalelineX1 = call("ij.Prefs.get", "PSA.scalelineX1", 10); // fall-back: long
        line
    scalelineY1 = call("ij.Prefs.get", "PSA.scalelineY1", imgheight-10); // at
        bottom
    scalelineX2 = call("ij.Prefs.get", "PSA.scalelineX2", imgwidth-10);
    scalelineY2 = call("ij.Prefs.get", "PSA.scalelineY2", imgheight-10);
    makeLine(scalelineX1, scalelineY1, scalelineX2, scalelineY2);
}


// Here favorite coordinates for the guess can be added,
// then also a label to the choose_scale array above in the prefernces
else if (oScalehelp == "Bottom left") makeLine(20, imgheight-30, 300,
    imgheight-30);
else if (oScalehelp == "Bottom right") makeLine(imgwidth-300, imgheight-30,
    imgwidth-20, imgheight-30);
else if (oScalehelp == "TEM at UAB") makeLine(32, imgheight-40, 264,
    imgheight-40); // for 140kV TEM from science building UAB (bottom left scale
    bar)
else if (oScalehelp == "TEM at PCB") makeLine(1083, imgheight-26, 1364,
    imgheight-26); // for Elisenda's TEM, 250k mag (bottom right scale bar)
else if (oScalehelp == "TEM at PCB (large bar)") makeLine(845, 1000, 1365,
    1000); // for Elisenda's TEM, new thin long scale bar

// this one tries to outline the scale bar with the WAND TOOL, starting
    coordinate = one pixel of the scale bar needed
else if (oScalehelp == "TEM at PCB (auto find)"){
    scaleX = 1355; // x coordinate of starting point for wand tool to outline
        the scale bar <-----<< CHANGE FOR YOUR SYSTEM
```

```
    scaleY = 999;  // y coordinate "
    removeScalebar = true;

    run("Set Scale...", "distance=NaN known=0 pixel=1 unit=pixel"); // unset scale

    doWand(scaleX, scaleY); // outline scale bar with wand tool and known
        starting point

    run("Set Measurements...", "area bounding redirect=None decimal=3");
    run("Measure");

    // remove scale bar after having user entered scale
    // setBackgroundColor(255, 255, 255);
    // run("Clear", "slice"); // clear scale bar = fill with white

    lastindex = nResults-1;
    // print(lastindex);

    barX = getResult("BX", lastindex); // TODO: How to get last measurement, or
        delete Results table first??
    barY = getResult("BY", lastindex);
    barW = getResult("Width", lastindex);
    // print("barX = ", barX);
    // print("barY = ", barY);
    // print("barW = ", barW);

    makeLine(barX, barY, barX+barW, barY);
}

if (oScalehelp != "NONE"){   // all interactive cases
    run("To Selection");
    setTool(4);
    scalemessage = "Please set yellow line to scale bar, then press OK to enter
        values.\n(Use + and - to zoom in and out)";
    waitForUser("USER INPUT: Manual adjustment", scalemessage);

    scaleStr = "unit="+oScaleunit+" global"; // the global option helps to have
        the same scale in next run
    run("Set Scale...", scaleStr);

    // open the dialog and let user enter the known distance
    run("Set Scale...");
```

```
    getLine(scalelineX1, scalelineY1, scalelineX2, scalelineY2, linewidth); //
        get coordinates from line selection
    call("ij.Prefs.set", "PSA.scalelineX1", scalelineX1); // save values for next
        run
    call("ij.Prefs.set", "PSA.scalelineY1", scalelineY1);
    call("ij.Prefs.set", "PSA.scalelineX2", scalelineX2);
    call("ij.Prefs.set", "PSA.scalelineY2", scalelineY2);
}


// get scale, i.e. length corresponding to one pixel, after (interactive) scaling
getPixelSize(unit, pWidth, pHeight, pDepth);

// print("unit: ", unit);    // log
// print("pWidth: ", pWidth);
// print("pHeight: ", pHeight);
// print("pDepth: ",pDepth);




// zoom out
run("Original Scale");


// ---------------------- Preprocessing
if (! oStepwiseMode) setBatchMode(true);

run("Duplicate...", "title="+imgtitle+"_preprocessed");
processingID = getImageID();
selectImage(processingID);

//  convert image to 8-bit gray by default, TODO: is 8 bit necessary?
run("8-bit"); // bitDepth()
run("Grays");

if (oDarkBG) run("Invert");

if (removeScalebar){   // fill scale bar with background color
    setBackgroundColor(255, 255, 255); // set to white
    doWand(scaleX, scaleY);  // outline again as defined in auto find option
    run("Clear", "slice");   // clear scale bar = fill with background color
    run("Select None");
```

```
}

if (oRemoveBG == "Rolling Ball (10% image size)"){ // RollingBall0.1  TODO: test!
    rollingradius = 0.1*(imgwidth); // somewhat arbitrary, r = 100 for a 1000 x
        1000 px image, r = 50 seemed too small
    run("Subtract Background...", "rolling="+rollingradius+" light");
    log_removeBG = "background_removal = rolling_ball_radius_"+rollingradius;
}
else if (oRemoveBG == "Rolling Ball (r = 50 px)"){ // TODO: test!
    run("Subtract Background...", "rolling=50 light");
    log_removeBG = "background_removal = rolling_ball_radius_50";
}
else if (oRemoveBG == "Inverted Gaussian (10% image size)"){ // probably works
    best for little coverage
    selectImage(processingID);
    run("Invert");
    run("Duplicate...", "title=blurred"); blurredID = getImageID();
    blurradius = 0.05*(imgwidth + imgheight); // somewhat arbitrary, r = 100 for
        a 1000 x 1000 px image
    run("Gaussian Blur...", "sigma="+blurradius);
    imageCalculator("Subtract", processingID, blurredID );
    selectImage(blurredID);
    close();
    selectImage(processingID);
    run("Invert");
    log_removeBG = "background_removal =
        inverted_gaussian_blur_radius_"+blurradius;
}
else{      // no background removal
    log_removeBG = "background_removal = NONE";
}

// choose_smoothing = newArray("Median r = 1 (3x3)", "Median r = 2 (5x5)",
    "Median r = 3 (7x7)", "Mean r = 1 (3x3)", "Mean r = 2 (5x5)", "Mean r = 3
    (7x7)", "Gaussian r = 1", "Gaussian r = 2", "Gaussian r = 3", "NONE");

if (oSmooth == "Median r = 1 (3x3)") run("Median...", "radius=1");
else if (oSmooth == "Median r = 2 (5x5)") run("Median...", "radius=2");
else if (oSmooth == "Median r = 3 (7x7)") run("Median...", "radius=3");
// removing mean.. better use Gaussian or median
// else if (oSmooth == "Mean r = 1 (3x3)") run("Mean...", "radius=1");
// else if (oSmooth == "Mean r = 2 (5x5)") run("Mean...", "radius=2");
// else if (oSmooth == "Mean r = 3 (7x7)") run("Mean...", "radius=3");
else if (oSmooth == "Gaussian r = 1") run("Gaussian Blur...", "sigma=1");
```

```
else if (oSmooth == "Gaussian r = 2") run("Gaussian Blur...", "sigma=2");
else if (oSmooth == "Gaussian r = 3") run("Gaussian Blur...", "sigma=3");

if (oSavePrepro) saveAs("PNG", preprofile);

if (oStepwiseMode) waitForUser("Preprocessing done.");

processingID = getImageID(); // just for the case..
selectImage(processingID);

// setBatchMode(false);

//  ---------------------- Segmentation
// choose_thresh = newArray("def", "ImageJ default (manual)", "Hysteresis
    (connectionthresholding*)", "Triangle (auto_threshold*)");

if (oThresh == "Manual (interactive)"){ // manual interactive thresholding
    // setAutoThreshold(); // give a guess? However, this will overwrite previous
        settings..
    setBatchMode("exit & display");  // Display all windows
    run("Threshold...");
    setTool(4);  // select zooming tool
    waitForUser("USER INPUT: Manual adjustment","THRESHOLDING of preprocessed
        image:\n\nIf necessary adjust threshold with sliders, then press
        OK.\n(Use + and - to zoom in and out)");

}

if (oThresh == "Hysteresis (connectionthresholding*)"){
    // Automatic threshold by hysteriesis (needs "connectionthresholding_" plugin
        installed!)
    //
        http://imagejdocu.tudor.lu/doku.php?id=plugin:segmentation:thresholding_by_connection:s
    run("connectionthresholding ");
    waitForUser("USER INPUT: Manual adjustment","THRESHOLDING of preprocessed
        image:\n\nIf necessary adjust threshold with sliders, then press
        OK.\n(Use + and - to zoom in and out)");
}

if (oThresh == "Triangle (auto_threshold*)"){
    // Automatic threshold, triangle method (needs Auto_Threshold plugin
        installed!)
    // http://pacific.mpi-cbg.de/wiki/index.php/Auto_Threshold
    run("Auto Threshold", "method=Triangle");
```

```
}

starttime = getTime(); // after all interactive things, start time for
    benchmarking (preprosssing is not included)

if (oThresh == "Automatic (ImageJ)"){
    setAutoThreshold();
}


if (! oStepwiseMode) setBatchMode(true);

getThreshold(lowerthreshold, upperthreshold);
run("Convert to Mask");

if (oWatershed == "Watershed filter"){
    run("Watershed");
}

if (oStepwiseMode) waitForUser("Segmentation done.");



// ---------------------- particle analyzer

// set Results window to display area and shape descriptors
run("Set Measurements...", "area shape redirect=None decimal=3");


// Convert size min and max to area, as expected from particle analyzer:
SizeMin = round(PI*pow(oDiamMin/2, 2));
SizeMax = round(PI*pow(oDiamMax/2, 2));
SizeNoise = round(PI*pow(oSizeNoise/2, 2));

panalyzerStr = "size="+SizeMin+"-"+SizeMax ;
panalyzerStr = panalyzerStr+" circularity="+oCircMin+"-"+oCircMax ;
panalyzerStr = panalyzerStr+" show=Outlines display exclude clear summarize";
run("Analyze Particles...", panalyzerStr);

outlinesID = getImageID();

if (oStepwiseMode) waitForUser("Particle Analyzer done.");

if (oOutlineExcluded == 0){     // not needed any more
```

```
    selectImage(processingID);
    close();
}

// ---------------------- Calculations in Results table
selectWindow("Results");

particles_found = nResults;
diam   = newArray(nResults);
area   = newArray(nResults);
volume = newArray(nResults);
totalvol = 0.0;  // initialize as float - really necessary?

for (i=0; i<nResults; i++){
  area[i] = getResult('Area', i);          // read "Area" column into array, used
     later for stats for logfile
  diam[i] = 2.0*sqrt(area[i]/PI);
  volume[i] = 4.0/3.0*PI*pow(diam[i]/2.0, 3.0);
  setResult("Diameter", i, diam[i]);       // add diameters to results table
  setResult("Volume", i, volume[i]);
  totalvol += volume[i];
}

if (oCalcCubes){                 //  calculate edge length of cubic particles,
    from projected square
    selectWindow("Results");
    cubeedge = newArray(nResults);
    cubevol = newArray(nResults);
    for (i=0; i<nResults; i++){
        // area[i] = getResult('Area', i);
        cubeedge[i] = sqrt(area[i]);
        cubevol[i] = pow(cubeedge[i], 3.0);
        setResult("CubeEdge", i, cubeedge[i]);
        setResult("CubeVolume", i, cubevol[i]);
    }
}

updateResults();

if (oSaveResults) saveAs("Measurements", imgdir+titlebase+"_resultstable.txt");
if (oStepwiseMode) waitForUser("Results table done.");


// ---------------------- Histogram
```

```
// choose_histo = newArray("0 - 50 nm / 0.5", "0 - 50 nm / 1.0", "0 - 100 nm /
    0.5", "0 - 100 nm / 1.0", "Automatic Binning", "NONE");


if (oHistShow != "NONE"){
    if (oCalcCubes){  // Make histogram of cube edge length
        if (oHistShow == "Automatic Binning"){
            run("Distribution...", "parameter=CubeEdge automatic");
        }
        else if (oHistShow == "0 - 50 nm / 0.5"){
            run("Distribution...", "parameter=CubeEdge or=100 and=0-50");
        }
        else if (oHistShow == "0 - 50 nm / 1.0"){
            run("Distribution...", "parameter=CubeEdge or=50 and=0-50");
        }
        else if (oHistShow == "0 - 100 nm / 0.5"){
            run("Distribution...", "parameter=CubeEdge or=200 and=0-100");
        }
        else if (oHistShow == "0 - 100 nm / 1.0"){
            run("Distribution...", "parameter=CubeEdge or=100 and=0-100");
        }
        histogramfilename=imgdir+titlebase+"_histogram_cubeedge";
    }
    else {     // make histogram of area-equivalent diameter assuming spherical
        particles
        if (oHistShow == "Automatic Binning"){
            run("Distribution...", "parameter=Diameter automatic");
        }
        else if (oHistShow == "0 - 50 nm / 0.5"){
            run("Distribution...", "parameter=Diameter or=100 and=0-50");
        }
        else if (oHistShow == "0 - 50 nm / 1.0"){
            run("Distribution...", "parameter=Diameter or=50 and=0-50");
        }
        else if (oHistShow == "0 - 100 nm / 0.5"){
            run("Distribution...", "parameter=Diameter or=200 and=0-100");
        }
        else if (oHistShow == "0 - 100 nm / 1.0"){
            run("Distribution...", "parameter=Diameter or=100 and=0-100");
        }
        histogramfilename=imgdir+titlebase+"_histogram_CEdiam";
    }
    histogramID = getImageID();
```

```
    if (oHistSavePNG){
        //selectWindow("Diameter Distribution");
        histofilenamePNG = histogramfilename + ".png";
        saveAs("PNG", histofilenamePNG);
    }
    if(oHistSaveTXT){
        Plot.getValues(histobin, histocount);
        histofilenameTXT = File.open(histogramfilename+".txt");
        for (i=0; i<histobin.length; i++){
            print(histofilenameTXT, histobin[i]+"\t"+histocount[i]);
        }
        File.close(histofilenameTXT);
    }
}


// ---------------------- Image with outlined particles

//  Place legend for outline colors below scalebar, bottom left or right

if ((scalelineX1+scalelineX2)/2 > imgwidth/2){   // then scale bar is on the right
    outlineLegendX = imgwidth-365;
    // rare case of "too circular" particles
    if (oCircMax < 1.0) outlineLegendX = imgwidth-440;
}
else outlineLegendX = 5; // (scale bar and) Legend on left hand side
outlineLegendY = imgheight-5; // Legend always at bottom of image


selectImage(outlinesID);
//run("Convert to Mask");
run("Invert");
run("8-bit");

if (oMergeOutlines == "Original image"){
    selectImage(imgID);
    run("Duplicate...", "title="+imgtitle+"_outlined.png");
    run("8-bit"); // bitDepth()
    outlinedID = getImageID();
}
else if (oMergeOutlines == "Preprocessed image"){
    open(preprofile);
    rename(imgtitle+"_outlined.png");
```

```
    run("8-bit"); // bitDepth()
    outlinedID = getImageID();
}

imageCalculator("Subtract", outlinedID, outlinesID);
run("RGB Color");

selectImage(outlinesID);
run("Green");
run("RGB Color");
imageCalculator("add", outlinedID, outlinesID);

selectImage(outlinedID);
setFont("SansSerif", 10); // , "antiliased");
setColor(0, 255, 0);
drawString("Matching all criteria", outlineLegendX, outlineLegendY);
if (oStepwiseMode) waitForUser("Particles matching size and circularity criteria
    outlined.");
selectImage(outlinesID);
close();


// ---------------------- Outline excluded particles as well
// todo: what about putting exclusion criterium as label, e.g. size or
    circularity?
// what about making (optional, additional) results table for exclude particles?

if (oOutlineExcluded){
    setFont("SansSerif", 10);

        // TOO SMALL PARTICLES ("just too small" - circularity criteria have to
            be met)
    selectImage(processingID);
    analyzeStr = "size="+oSizeNoise+"-"+SizeMin+"
        circularity="+oCircMin+"-"+oCircMax+" show=Outlines exclude";
    if (oTableExcluded) analyzeStr = analyzeStr + " display";
    run("Analyze Particles...", analyzeStr);
    exSmall = getImageID();
    run("Rename...","Too small particles");
    run("Invert");
    imageCalculator("Subtract", outlinedID, exSmall ); // first subtract the
        white outlines, then add the colored ones
    run("Magenta");
    run("RGB Color");
```

```
imageCalculator("Add", outlinedID, exSmall);

selectImage(outlinedID);
setColor(255, 0, 255);
drawString("Too small size", outlineLegendX+110, outlineLegendY);
selectImage(exSmall);
if (oStepwiseMode) waitForUser("Too small particles outlined (excluded from
    analysis).");
close();

    // TOO LARGE PARTICLES ("just too large" - circularity criteria have to
       be met)
selectImage(processingID);
analyzeStr = "size="+SizeMax+"-infinity circularity="+oCircMin+"-"+oCircMax+"
    show=Outlines exclude";
if (oTableExcluded) analyzeStr = analyzeStr + " display";
run("Analyze Particles...", analyzeStr);
exLarge = getImageID();
run("Rename...","Too large particles");
run("Invert");
imageCalculator("Subtract", outlinedID, exLarge);
run("Red");
run("RGB Color");
imageCalculator("Add", outlinedID, exLarge);

selectImage(outlinedID);
setColor(255, 0, 0);
drawString("Too large size", outlineLegendX+195, outlineLegendY);
selectImage(exLarge);
if (oStepwiseMode) waitForUser("Too large particles outlined (excluded from
    analysis).");
close();

     // NON-CIRCULAR PARTICLES (regardless of size but above oSizeNoise)
selectImage(processingID);
analyzeStr = "size="+oSizeNoise+"-infinity circularity=0.0-"+oCircMin+"
    show=Outlines exclude";
if (oTableExcluded) analyzeStr = analyzeStr + " display";
run("Analyze Particles...", analyzeStr);
exNonCirc = getImageID();
run("Rename...","Too non-circular particles");
run("Invert");
imageCalculator("Subtract", outlinedID, exNonCirc);
run("Yellow");
```

```
run("RGB Color");
imageCalculator("Add", outlinedID, exNonCirc);

selectImage(outlinedID);
setColor(255, 255, 0);
drawString("Non-circular", outlineLegendX+275, outlineLegendY);
selectImage(exNonCirc);
if (oStepwiseMode) waitForUser("Particles with too small circularity outlined
    (excluded from analysis).");
close();

    // TOO-CIRCULAR PARTICLES: for the analysis of spherical particles, this
       is not appropriate..
if (oCircMax < 1.0){
    selectImage(processingID);
    analyzeStr = "size=0-infinity circularity="+oCircMax+"-1.0 show=Outlines
       exclude";
    if (oTableExcluded) analyzeStr = analyzeStr + " display";
    run("Analyze Particles...", analyzeStr);
    exTooCirc = getImageID();
    run("Rename...","Too circular particles (!?)");
    run("Invert");
    imageCalculator("Subtract", outlinedID, exTooCirc);
    // no color, leave white
    run("RGB Color");
    imageCalculator("Add", outlinedID, exTooCirc);

    selectImage(outlinedID);
    setColor(255, 255, 255);
    drawString("Too circular", outlineLegendX+350, outlineLegendY);
    selectImage(exTooCirc);
    if (oStepwiseMode) waitForUser("Particles with too large circularity
       outlined (excluded from analysis). (Do you want that?)");
    close();
}
selectImage(processingID);
close();

particles_excluded = nResults - particles_found;

if (oTableExcluded){  // calculate diameter (and cube edge length), but not
    volume for excluded particles.
    for (i=0; i<nResults; i++){
```

```
            setResult("Diameter", i, 2.0*sqrt(getResult('Area', i)/PI)); // add
                diameters to results table
        }
        if (oCalcCubes){ // separate loop so condition will only get checked once
            for (i=0; i<nResults; i++){
                setResult("CubeEdge", i, sqrt(getResult('Area', i)));  // add cube
                    edge length to results table
            }
        }
        updateResults();
    }
}

// TODO: see which way and which order is best -
// Maybe display outlined particles before closing to have a quick check?
if (FULL_AUTO_MODE){ // close remaining windows

    selectImage(outlinedID); // save image of outlined particles before closing
    setTool(11);
    if (oSaveOutlines) saveAs("PNG", imgdir+titlebase+"_outlined.png");

    selectImage(outlinedID);
    close();
    selectImage(histogramID);
    close();
    selectImage(imgID);
    close();   // close original image as well
}


if (FULL_AUTO_MODE == false){
    setBatchMode("exit & display");  // Display all remaining windows = outlined
        and histogram

    selectImage(outlinedID); // save *after* displaying remaining windows, this
        should make the macro appear more responsive
    setTool(11);
    if (oSaveOutlines) saveAs("PNG", imgdir+titlebase+"_outlined.png");

    if (oHistShow != "NONE"){
        selectImage(histogramID);   // bring small histogram window to front
    }

}
```

```
// ---------------------- Logfile
stoptime = getTime();
processing_time += (stoptime-starttime)/1000;

if (oLogfile){
    logfile = File.open(imgdir+titlebase+"_logfile.txt");
        // Image information
    print(logfile, "macro_name = \""+macro_name+"\"");  // with double quotes
    print(logfile, "image_dir = \""+imgdir+"\"");
    print(logfile, "image_title = \""+imgtitle+"\"");
    print(logfile, "analysis_timestamp = \""+TimeString+"\"");
    print(logfile, "width = "+imgwidth);
    print(logfile, "height = "+imgheight);
    print(logfile, "px_width = "+pWidth);
    print(logfile, "px_height = "+pHeight);
    print(logfile, "length_unit = \""+unit+"\"");
    if (oScalehelp != "NONE"){   // all interactive cases
        print(logfile, "scale_line_x1 = "+scalelineX1);
        print(logfile, "scale_line_y1 = "+scalelineY1);
        print(logfile, "scale_line_x2 = "+scalelineX2);
        print(logfile, "scale_line_y2 = "+scalelineY2);
    }
    else print(logfile, "scaling = non-interactive");

    print(logfile, "");

        // options
    print(logfile, "smoothing_filter = "+oSmooth);
    print(logfile, "background_removal = "+oRemoveBG);
    print(logfile, log_removeBG);
    print(logfile, "threshold_mode = "+oThresh);
    print(logfile, "threshold_lower = "+lowerthreshold);
    print(logfile, "threshold_upper = "+upperthreshold);
    print(logfile, "watershed_filter = "+oWatershed);
    print(logfile, "min_diameter = "+oDiamMin);
    print(logfile, "max_diameter = "+oDiamMax);
    print(logfile, "min_size_area = "+SizeMin);
    print(logfile, "max_size_area = "+SizeMax);
    print(logfile, "min_circularity = "+oCircMin);
    print(logfile, "max_circularity = "+oCircMax);
    print(logfile, "max_noise_diam = "+oSizeNoise);
    print(logfile, "max_noise_area = "+SizeNoise);
```

```
print(logfile, "analyzer_string = \""+panalyzerStr+"\"");
print(logfile, "");



    // Analysis results
print(logfile, "particles_found = "+particles_found);
//print(logfile, "particles_excluded = "+particles_excluded);
Array.getStatistics(area, min, max, mean, std);
print(logfile, "area_mean = "+mean);
print(logfile, "area_std = "+std);
print(logfile, "area_min = "+min);
print(logfile, "area_max = "+max);
print(logfile, "");

print(logfile, "Area-equivalent diameter for spherical particles
    (circle-equivalent, CEdiameter)");
Array.getStatistics(diam, min, max, mean, std);
print(logfile, "diameter_mean = "+mean);
print(logfile, "diameter_std = "+std);
print(logfile, "diameter_min = "+min);
print(logfile, "diameter_max = "+max);
print(logfile, "");
meandiam = mean;   // store for volume-averaged volume

Array.getStatistics(volume, min, max, mean, std);
print(logfile, "volume_mean = "+mean); // number-average
print(logfile, "volume_std = "+std);
print(logfile, "volume_min = "+min);
print(logfile, "volume_max = "+max);

print(logfile, "volume_total = "+totalvol);
print(logfile, "volume_Vavg = "+ (4.0/3.0*PI*pow(meandiam/2.0,3.0)) ); //
    volume-average
print(logfile, "");

if (oCalcCubes){
    print(logfile, "Cube edge length (from projected area), USED FOR
        HISTOGRAM");
    Array.getStatistics(cubeedge, min, max, mean, std);
    print(logfile, "cubeedge_mean = "+mean);
    print(logfile, "cubeedge_std = "+std);
    print(logfile, "cubeedge_min = "+min);
    print(logfile, "cubeedge_max = "+max);
```

```
        print(logfile, "");

        Array.getStatistics(cubevol, min, max, mean, std);
        print(logfile, "cubevol_mean = "+mean);
        print(logfile, "cubevol_std = "+std);
        print(logfile, "cubevol_min = "+min);
        print(logfile, "cubevol_max = "+max);
        print(logfile, "");
    }

    print(logfile, "processing_time = "+processing_time+" s");
    print(logfile, "logfile_status = \"done\""); print(logfile, "");

    File.close(logfile); // only one file can be opened at a time

    if (oStepwiseMode) waitForUser("Logfile done.");
}

// ---------------------- that's it.
```

Appendix E

R SCRIPT FOR VSM SIZE ANALYSIS

```
# Options ---------------------------------------------------------------

display.mh = "no"
export.data = "yes"
export.plots = "no"
export.grid = "yes"


# Import packages -------------------------------------------------------

my.packages <- c("rChoiceDialogs", "purrr", "dplyr", "ggplot2", "ggpubr",
    "scales", "sfsmisc", "signal")
lapply(my.packages, require, character.only = TRUE)


# Functions -------------------------------------------------------------

shift.data <- function(data) {
  moment.max = max(data)
  moment.min = min(data)
  moment.diff = abs(moment.max) - abs(moment.min)
  if ((moment.max < 0) |
      (moment.min > 0)) {
    stop("Data shift not possible, bad data")
  }
  shifted.data = data - (moment.diff / 2)
  return(shifted.data)
}


read.dat <- function(flnm) {
  read.csv(flnm, skip = 12, sep = "\t", header = F, col.names = c("field",
      "moment", "blank")) %>%
    mutate(filename = flnm) %>%
```

```
    select(field, moment, filename) %>%
    na.omit() %>%
    group_by(filename) %>%
    mutate(range = round((max(field)-min(field))/2,0)) %>%
    ungroup() %>%
    select(range, field, moment)
}

read.conc <- function(flnm) { read.csv(flnm, header = FALSE, skip = 0) }


find.fit <- function (data, type){
  tolerance <- 0.9999
  tolerance.drop <- 0.0001

  if (type == "middle"){
    frac <- 0.2
    data <- data %>%
      dplyr::filter(between(moment, frac * min(moment), frac * max(moment))) %>%
      arrange(field)
    # plot(data$field,data$moment)
  }

  if (type == "negative.reciprocal") {
    frac <- 0.8
    data <- data %>%
      dplyr::filter(between(moment, min(moment), frac * min(moment))) %>%
      arrange(field)
  }

  if (type == "positive.reciprocal") {
    frac <- 0.8
    data <- data %>%
      dplyr::filter(between(moment, frac * max(moment), max(moment))) %>%
      arrange(field)
  }

  fits = data.frame()

  while (tolerance > 0.75) {
    i = k = 1
    j = nrow(data)

    while (i < j & j - i > 20) {
```

```
if (nrow(fits) < k){
  if (type == "middle") {
    fit = lm(data$moment[i:j] ~ data$field[i:j])
    summary(fit)$coefficients[2]
    fits[k, 1] = type
    fits[k, 2] = data$field[i]
    fits[k, 3] = data$field[j]
  }

  if (type == "negative.reciprocal") {
    fit = lm(data$moment[i:j] ~ data$reciprocal[i:j])
    fits[k, 1] = type
    fits[k, 2] = data$reciprocal[i]
    fits[k, 3] = data$reciprocal[j]
  }

  if (type == "positive.reciprocal") {
    fit = lm(data$moment[i:j] ~ data$reciprocal[i:j])
    fits[k, 1] = type
    fits[k, 2] = data$reciprocal[i]
    fits[k, 3] = data$reciprocal[j]
  }

  fits[k, 4] = j - i + 1
  fits[k, 5] = summary(fit)$coefficients[2]
  fits[k, 6] = summary(fit)$coefficients[1]
  fits[k, 7] = summary(fit)$r.squared
}

if (fits[k, 7] > tolerance) {
  colnames(fits) = c("source" ,"lower.bound", "upper.bound", "num.points",
      "slope","intercept", "r.2")
  return(fits[k,])
}

if (type == "middle") {
  i = i + 1
  j = j - 1
}

if (type == "negative.reciprocal") {
  j = j - 1
}
```

```
      if (type == "positive.reciprocal") {
        i = i + 1
      }
      k = k + 1
    }

    tolerance = tolerance - tolerance.drop
    # print(tolerance)
  }
  stop("Failed to meet fit tolerance")
}

# Function to calculate the nanoparticle size based on Chantrell fitting
calc.d <- function(kB, temperature, Xi, Ho, moment, magnetization) {
  diameter = ((((18 * ( kB ) * temperature) / (pi * magnetization)) * sqrt(Xi /
      (3 * moment * Ho))) ^ (1 / 3)) * (10 ^ 9)
  return(diameter)
}


# Function to calculate the nanoparticle size distribution based on Chantrell
    fitting
calc.sigma <- function(Xi, Ho, moment) {
  sigma = ((log(3 * Xi / (moment / Ho))) ^ (1 / 2)) / 3
  return(sigma)
}


# Function to calculate 1st standard deviation
calc.std.dev <- function(diameter, sigma) {
  std.dev.low = diameter / exp(sigma)
  std.dev.high = diameter * exp(sigma)
  std.dev = c(std.dev.low, std.dev.high)
  return(std.dev)
}


# Function to calculate the real saturation magnetization of the sample
calc.Ms <- function(moment, concentration.fe, volume, density) {
  concentration.fe3o4 = concentration.fe / 0.72
  Am2 = moment
  Am2mg = Am2 / (concentration.fe3o4 * volume / 1000)
  Am = Am2mg * density
  kAm = Am / 1000
```

```
  return(kAm)
}

# Function to plot log normal distribution on exportable plot
log.normal = function(x, size, sigma) {
  (1 / ((x / size) * sigma * sqrt(2 * pi))) * exp((-log(x / size) ^ 2) / (2 *
     sigma ^ 2))
}


# Import data ------------------------------------------------------------

setwd(rchoose.dir(caption = "Select Directory")) # Asks user to choose directory
    containing data files

dat <- list.files(pattern = "*\\d.txt", full.names = T, recursive = F) %>%
    map_df(~ read.dat(.))


# Spectrometer information -----------------------------------------------

# Set physical values and constants
vol <- 100 #uL
density <- 5180 # kg/m^3
kB <- 1.38e-23 # J/K
temperature <- 298 # K


if (file.exists("conc.txt")) {
  conc <- list.files(pattern = "conc.txt", full.names = T, recursive = F) %>%
    map_df(~ read.conc(.))
  conc <- conc[, 1] #mgFe/mL
  conc.new = conc / 1000 #gFe/mL
  vol.new = vol / 1000 #mL
  mass = conc.new * vol.new #gFe
  mh.label = expression(paste("M [kA m" ^ "-1", "]"))
} else {
  conc <- 0 #mgFe/mL
  mass <- 1 #filler value to prevent conversion without known conc
  mh.label = expression(paste("m [Am" ^ "2", "]"))
}

# Data correction to account for instrument error
dat = dat %>%
```

```
  group_by(range) %>%
  mutate(moment = shift.data(moment)) %>% #center moment around zero
  ungroup() %>%
  mutate(range = range * (10 ^ -1)) %>% #convert gauss to mT
  mutate(field = field * (10 ^ -1)) %>% #convert gauss to mT
  mutate(reciprocal = 1 / field) %>%
  mutate(moment = moment * (10 ^ 3)) %>% #convert emu to Am2
  mutate(norm = 2 * ((moment - min(moment)) / (max(moment) - min(moment))) - 1)
      %>%
  mutate(magnetization = ((moment / ((conc / 0.72) * vol / 1000)) * density) /
      1000) #calculate magnetization

fits = find.fit(dat, "middle") %>%
  dplyr::bind_rows(., find.fit(dat, "negative.reciprocal")) %>%
  dplyr::bind_rows(., find.fit(dat, "positive.reciprocal")) %>%
  group_by(source) %>%
  mutate(Xi = abs(slope)) %>%
  mutate(Ho = abs(1 / (-intercept/slope))) %>%
  mutate(moment = abs(intercept)) %>%
  mutate(Ms = case_when(conc == 0 ~ 446,
                        conc != 0 ~ abs(calc.Ms(moment, conc, vol, density))))

# View(fits)

info = data.frame(
  conc,
  round(mean(c(fits$Ms[2], fits$Ms[3])), 2),
  round(calc.d(kB, temperature, fits$Xi[1],
         mean(c(fits$Ho[2],fits$Ho[3])),
         mean(c(fits$moment[2], fits$moment[3])),
         mean(c(fits$Ms[2], fits$Ms[3]))), 2),
  round(calc.sigma(fits$Xi[1], mean(fits$Ho[2],fits$Ho[3]),
      mean(fits$moment[2],fits$moment[3])), 2))
colnames(info) = c("Conc [mgFe/mL]", "Ms [kA/m]", "Size [nm]", "Sigma")


# Plots ------------------------------------------------------------------

theme_new <- function (base_size=24, base_line_size=1) {
  theme_bw(base_size=base_size,
           base_family="") %+replace%
    theme(
      axis.text.x = element_text(size=base_size, margin =
          margin(t=0.75*base_size,b=0.25*base_size), color="black"),
```

```
      axis.text.y = element_text(size=base_size, margin =
         margin(r=0.75*base_size,l=0.25*base_size), color="black"),
      axis.title=element_text(size=base_size, color="black"),
      axis.line=element_line(size=base_line_size, lineend="square",
         color="black"),
      axis.ticks=element_line(size=base_line_size, lineend="square",
         color="black"),
      axis.ticks.length=unit(-8, "pt"),
      panel.border=element_blank(),
      panel.grid=element_blank(),
      aspect.ratio = 1,
      legend.background=element_rect(fill="transparent", colour=NA),
      legend.position=c(1, 1),
      legend.justification=c("right", "top"),
      legend.direction="vertical",
      legend.title=element_text(size=0.75*base_size),
      legend.title.align=0.5,
      legend.text=element_text(size=0.75*base_size),
      legend.text.align=0
    )
}

xlab = expression(paste(mu[0],"H [mT]"))
ylab = mh.label
ylab = "Norm. [a.u.]"

data.set <- dat %>% dplyr::filter(range == min(range))

p1 = ggplot(data.set, aes(x = field, y = magnetization)) +
  geom_point(size = 3, shape = 1, stroke = 1) +
  geom_path(size = 1) +
  scale_x_continuous(breaks = pretty_breaks(3)) +
  scale_y_continuous(breaks = c(min(pretty(min(data.set$magnetization))), 0,
     max(pretty(max(data.set$magnetization)))),
                     limits = c(min(pretty(min(data.set$magnetization))),
                        max(pretty(max(data.set$magnetization))))) +
  theme_new() +
  guides(col = guide_legend(ncol = 1)) +
  labs(x = xlab, y = ylab)

data.set <- dat %>% dplyr::filter(range == median(range))

p2 = ggplot(data.set, aes(x = field, y = magnetization)) +
  geom_point(size = 3, shape = 1, stroke = 1) +
```

```
  geom_path(size = 1) +
  scale_x_continuous(breaks = pretty_breaks(3)) +
  scale_y_continuous(breaks = c(min(pretty(min(data.set$magnetization))), 0,
      max(pretty(max(data.set$magnetization)))),
                     limits = c(min(pretty(min(data.set$magnetization))),
                        max(pretty(max(data.set$magnetization))))) +
  theme_new() +
  guides(col = guide_legend(ncol = 1)) +
  labs(x = xlab, y = ylab)

data.set <- dat %>% dplyr::filter(range == max(range))

p3 = ggplot(data.set, aes(x = field, y = magnetization)) +
  geom_point(size = 3, shape = 1, stroke = 1) +
  geom_path(size = 1) +
  scale_x_continuous(breaks = pretty_breaks(3)) +
  scale_y_continuous(breaks = c(min(pretty(min(data.set$magnetization))), 0,
      max(pretty(max(data.set$magnetization)))),
                     limits = c(min(pretty(min(data.set$magnetization))),
                        max(pretty(max(data.set$magnetization))))) +
  theme_new() +
  guides(col = guide_legend(ncol = 1)) +
  labs(x = xlab, y = ylab)


data.set = data.frame(x = 0)
xmin = 0.5*info$`Size [nm]`
xmax = 1.5*info$`Size [nm]`
xlab = expression(paste(d[0]," [nm]"))
ylab = "Density [%]"

p4 = ggplot(data.set) +
  stat_function(fun = log.normal, args = list(info$`Size [nm]`, info$Sigma),
      geom="line", size = 1) +
  scale_x_continuous(breaks = pretty_breaks(3), limits = c(xmin, xmax)) +
  scale_y_continuous(breaks = pretty_breaks(3)) +
  theme_new() +
  guides(col = guide_legend(ncol = 1)) +
  labs(x = xlab, y = ylab)


# Set export directory whether or not saving images is selected

if (export.data == "yes" || export.plots == "yes" || export.grid == "yes") {
```

```
  main.directory = getwd()
  export.directory = "export"
  dir.create(file.path(main.directory, export.directory), showWarnings = FALSE)
  setwd(file.path(main.directory, export.directory))
}

if(export.data == "yes"){
  write.csv(info, "info.csv", row.names = FALSE)
  write.csv(dat, "dat.csv", row.names = FALSE)
}

if(export.plots == "yes"){
  ggsave("mh.png", p2, width = 4.5, height = 4.5, dpi = "retina")
  ggsave("histogram.png", p4, width = 4.5, height = 4.5, dpi = "retina")
}

if(export.grid == "yes"){
  grid <- ggarrange(p1, p2, p3, p4, hjust = -0.25, heights = c(1,1), widths =
      c(1,1),
                    labels = c("(a)", "(b)","(c)","(d)"), font.label =
                        list(size = 24),
                    ncol = 2, nrow = 2)
  ggsave("grid.png", grid, width = 9, height = 9, dpi = "retina")
}

if (display.mh == "yes"){
  p1
}

info
```

Appendix F

R SCRIPT FOR MPS DATA PROCESSING

```
# Options ---------------------------------------------------------------

display.psf = "no"
display.har = "no"
export.data = "yes"
export.plots = "no"
export.grid = "yes"

# Import packages -------------------------------------------------------

my.packages <- c("rChoiceDialogs", "purrr", "dplyr", "ggplot2", "ggpubr",
    "scales", "sfsmisc", "signal")
lapply(my.packages, require, character.only = TRUE)


# Functions -------------------------------------------------------------

scientific_10_full <- function(x) {
  ifelse (x %% 1 == 0,
         parse(text = gsub("e+00", "", scientific_format()(x))),
         ifelse (x > 1 & x < 0.11, as.numeric(as.character(x)),
                parse(text = gsub("e", " %*% 10^", scientific_format()(x)))))
}

scientific_10 <- function(x) {
  ifelse (x %% 1 == 0, parse(text = gsub("e+00", "", scientific_format()(x))),
         ifelse (x > 1 & x < 0.11, as.numeric(as.character(x)), parse(text =
            gsub(".*e", "10^", scientific_format()(x)))))
}

read.lvm <- function(flnm) {
  read.csv(flnm, skip = 35, sep = "\t", header = F,
    col.names = c("background.time","background.data", "sample.time",
        "sample.data", "psf.time","psf.data",
```

```
                "field.time","field.data","na","peakToPeak",
                   "sample.time.full","sample.data.full", "comment"
    )
  ) %>%
    mutate(filename = flnm) %>%
    select(background.time, field.data, background.data, sample.data, psf.data)
        %>%
    group_by(background.time) %>%
    summarise_all(funs(mean)) %>%
    rename(time = background.time) %>%
    na.omit()
}

read.lvm.full <- function(flnm) {
  read.csv(flnm, skip = 35, sep = "\t", header = F,
    col.names = c("background.time","background.data", "sample.time",
        "sample.data", "psf.time","psf.data",
                "field.time","field.data","na","peakToPeak",
                   "sample.time.full","sample.data.full", "comment"
    )
  ) %>%
    mutate(filename = flnm) %>%
    group_by(filename) %>%
    mutate(position = 1:n()) %>%
    ungroup() %>%
    select(sample.time.full, sample.data.full, position)
    # rename(time = sample.time.full) %>%
}

read.lvm.field <- function(flnm) { read.csv( flnm, skip = 35, nrow = 1, sep =
    "\t", header = F) }

read.lvm.param <- function(flnm) { read.csv(flnm, skip = 24, nrow = 1, sep =
    "\t", header = F) }

read.conc <- function(flnm) { read.csv(flnm, header = FALSE, skip = 0) }

# Import data ------------------------------------------------------------

setwd(rchoose.dir(caption = "Select Directory")) # Asks user to choose directory
    containing data files

nfiles <- length(list.files(pattern = "*\\d.lvm", full.names = T, recursive = F))
```

```
dat <- list.files(pattern = "*\\d.lvm", full.names = T, recursive = F) %>%
    map_df(~ read.lvm(.))
full <- list.files(pattern = "*\\d.lvm", full.names = T, recursive = F) %>%
    map_df(~ read.lvm.full(.))
field <- list.files(pattern = "*\\d.lvm", full.names = T, recursive = F) %>%
    map_df(~ read.lvm.field(.))
param <- list.files(pattern = "*\\d.lvm", full.names = T, recursive = F) %>%
    map_df(~ read.lvm.param(.))


# Spectrometer information ------------------------------------------------
# Sensitivity is receive coil sensitivity in [1/m] from [A/m/A].
# Spectrometer v2, built by Jack-Howell Clark in Fall 2013, S = 1989.44 1/m
    (0.0025 T/A).
# Frequency, sample rate, and field amplitude are all obtained from .lvm data
    files.

sensitivity = 1989.44 # 1/m
mu0 = 4 * pi * 1e-7
frequency = mean(param$V2) # Hz
omega = 2 * pi * frequency # Hz
sample.rate = mean(param$V4)
periods = mean(param$V14)
field.amplitude = mean(field$V10) / 2 # mT
vol <- 150 #uL

if (file.exists("conc.txt")) {
  conc <- list.files(pattern = "conc.txt", full.names = T, recursive = F) %>%
    map_df(~ read.conc(.))
  conc <- conc[, 1] #mgFe/mL
  conc.new = conc / 1000 #gFe/mL
  vol.new = vol / 1000 #mL
  mass = conc.new * vol.new #gFe
  psf.label = expression(paste(chi, " [m" ^ "3", "gFe" ^ "-1", "]"))
  har.label = expression(paste("Amp. [Am" ^ "2", "gFe" ^ "-1", "]"))
} else {
  conc <- 0 #mgFe/mL
  mass <- 1 #filler value to prevent conversion without known conc
  psf.label = expression(paste(chi, " [x10"^"-9","m" ^ "3", "]"))
  har.label = expression(paste("Amp. [Am" ^ "2", "]"))
}


# Interpolate data points in primary data set
```

```
int = 7000

dat = dat %>%
  dplyr::filter(row_number() <= (n() / nfiles)) %>%
  add_row(., time = approx(.$time,n = int - nrow(.))$y) %>%
  arrange(time) %>%
  mutate(., field.data = approx(.$field.data, n = nrow(.))$y) %>%
  mutate(., background.data = approx(.$background.data, n = nrow(.))$y) %>%
  mutate(., sample.data = approx(.$sample.data, n = nrow(.))$y) %>%
  mutate(., psf.data = approx(.$psf.data, n = nrow(.))$y)

# Find fit coefficient of field to determine appropriate shift (phi)
model = nls(
  dat$field.data ~ -field.amplitude * cos(omega * (dat$time + phi)),
  data = dat,
  control = list(
    maxiter = 100000,
    minFactor = 1e-3,
    printEval = TRUE
  ),
  start = list(phi = 1),
  algorithm = "port"
)

dat = dat %>%
  mutate(field.fitted = predict(model)) %>%
  mutate(psf.m3 = psf.data / -(sensitivity * field.amplitude * omega * sin(omega
      * (
    time + coef(model)
  )))) %>%
  mutate(psf.m3 = psf.m3 / mass) %>%
  dplyr::filter(row_number() <= (n() / 2)) %>%
  dplyr::filter(field.data >= 0.95 * min(field.data) &
                  field.data <= 0.95 * max(field.data)) %>%
  mutate(field.data = round(field.data * 1000, 4)) %>%
  mutate(field.fitted = round(field.fitted * 1000, 4)) %>%
  mutate(psf.norm = psf.m3/max(psf.m3)) %>%
  mutate(direction = case_when(row_number() <= (n() / 2) ~ "forward",
                               row_number() > (n() / 2) ~ "reverse")) %>%
  group_by(direction) %>%
  mutate(fwhm = case_when( length(field.fitted[field.fitted > field.fitted[psf.m3
      == max(psf.m3)]][which.min(abs(psf.m3[field.fitted > field.fitted[psf.m3 ==
      max(psf.m3)]] - max(psf.m3) / 2))] - field.fitted[field.fitted <
      field.fitted[psf.m3 == max(psf.m3)]][which.min(abs(psf.m3[field.fitted <
```

```
    field.fitted[psf.m3 == max(psf.m3)]] - max(psf.m3) / 2))]) == 0 ~ 1,
                        length(field.fitted[field.fitted > field.fitted[psf.m3
                           == max(psf.m3)]][which.min(abs(psf.m3[field.fitted >
                           field.fitted[psf.m3 == max(psf.m3)]] - max(psf.m3) /
                           2))] - field.fitted[field.fitted <
                           field.fitted[psf.m3 ==
                           max(psf.m3)]][which.min(abs(psf.m3[field.fitted <
                           field.fitted[psf.m3 == max(psf.m3)]] - max(psf.m3) /
                           2))]) >= 1 ~ field.fitted[field.fitted >
                           field.fitted[psf.m3 ==
                           max(psf.m3)]][which.min(abs(psf.m3[field.fitted >
                           field.fitted[psf.m3 == max(psf.m3)]] - max(psf.m3) /
                           2))] - field.fitted[field.fitted <
                           field.fitted[psf.m3 ==
                           max(psf.m3)]][which.min(abs(psf.m3[field.fitted <
                           field.fitted[psf.m3 == max(psf.m3)]] - max(psf.m3) /
                           2))])) %>%
  # mutate(fwhm = 1) %>%
  mutate(mh.norm = cumsum(psf.m3)) %>%
  mutate(mh.norm = case_when(direction == "reverse" ~ max(mh.norm) - mh.norm,
                         direction == "forward" ~ mh.norm)) %>%
  mutate(mh.norm = 2 * ((mh.norm-min(mh.norm))/(max(mh.norm)-min(mh.norm))) - 1)
      %>%
  ungroup() %>%
  mutate(har = seq.int(n()) - 1) %>%    #shift to correct index
  mutate(amp = abs(fft(mh.norm)) ) %>%  #fft
  # mutate(amp = amp / n()) %>%
  # mutate(amp = amp * har) %>%           #adjusts harmonic intensities to be
      consistent with exp data
  mutate(fifthThird = amp[har == 5] / amp[har == 3])


full = full %>%
  group_by(position) %>%
  summarise_each(funs(mean,sd,se=sd(.)/sqrt(n())))
  # summarise_all(mean)

delf = sample.rate / nrow(full)

full = full %>%
  mutate(fft_mean = fft(sample.data.full_mean)) %>%
  mutate(fft_sd = fft(sample.data.full_sd)) %>%
  mutate(amp_mean = sqrt(((Re(fft_mean)^2) + (Im(fft_mean)^2)) / n())) %>%
  mutate(amp_sd = sqrt(((Re(fft_sd)^2) + (Im(fft_sd)^2)) / n())) %>%
```

```
  slice(1:(n()/2)) %>%
  mutate(frequencies = row_number() * delf) %>%
  mutate(amp_mean = (amp_mean * 2) / (sensitivity * mu0 * row_number() * delf * 2
      * pi)) %>%
  mutate(amp_sd = (amp_sd * 2) / (sensitivity * mu0 * row_number() * delf * 2 *
      pi)) %>%
  slice(periods*row_number()+1) %>%
  mutate(har = seq.int(n())) %>%
  mutate(oddeven = case_when(har %% 2 != 0 ~ "odd",
                             har %% 2 == 0 ~ "even"))

dat <- dat %>%
  mutate(fifthThird = full$amp_mean[full$har == 5] / full$amp_mean[full$har == 3])


# Plots ----------------------------------------------------------------

theme_new <- function (base_size=24, base_line_size=1) {
  theme_bw(base_size=base_size,
           base_family="") %+replace%
    theme(
      axis.text.x = element_text(size=base_size, margin =
         margin(t=0.75*base_size,b=0.25*base_size), color="black"),
      axis.text.y = element_text(size=base_size,
         margin=margin(r=0.75*base_size,l=0.25*base_size), color="black"),
      axis.title=element_text(size=base_size, color="black"),
      axis.line=element_line(size=base_line_size, lineend="square",
         color="black"),
      axis.ticks=element_line(size=base_line_size, lineend="square",
         color="black"),
      axis.ticks.length=unit(-8, "pt"),
      panel.border=element_blank(),
      panel.grid=element_blank(),
      aspect.ratio = 1,
      legend.background=element_rect(fill="transparent", colour=NA),
      legend.position=c(0, 1),
      legend.justification=c("left", "top"),
      legend.direction="vertical",
      legend.title=element_blank(),
      legend.title.align=0.5,
      legend.text=element_text(size=0.75*base_size),
      legend.text.align=0
    )
}
```

```
data.set <- dat

xlab = expression(paste("t [",mu,"s]"))
ylab = expression(paste(mu[0],"H [mT]"))
xmin = 1e6*(min(data.set$time) - 0.1*max(data.set$time))
xmax = 1e6*(max(data.set$time) + 0.1*max(data.set$time))
ymin = min(data.set$field.data) - 0.1*max(data.set$field.data)
ymax = max(data.set$field.data) + 0.1*max(data.set$field.data)

p1 = ggplot(data.set) +
  geom_line(aes(x = 1e6*time, y = field.data), size = 1, color = "black") +
  # geom_line(aes(x = 1e6*time, y = field.fitted), size = 1, color = "red") +
  scale_x_continuous(breaks = pretty_breaks(n=3), limits = c(xmin,xmax)) +
  scale_y_continuous(breaks = pretty_breaks(n=3)) +
  theme_new() +
  guides(col = guide_legend(ncol = 1)) +
  labs(x = xlab, y = ylab)

ylab = "Amp. [mV]"
ymin = 1e3*(min(data.set$background.data,data.set$sample.data,
    data.set$psf.data) - 0.1*max(data.set$background.data,data.set$sample.data,
    data.set$psf.data))
ymax = 1e3*(max(data.set$background.data,data.set$sample.data,
    data.set$psf.data) + 0.1*max(data.set$background.data,data.set$sample.data,
    data.set$psf.data))

p2 = ggplot(data.set) +
  theme_new() +
  # geom_point(aes(x = 10e5*time, y = background.data), size = 3, stroke = 1,
      color = "blue") +
  geom_line(aes(x = 1e6*time, y = 1e3*background.data, color = "black"), size =
      1) +
  geom_line(aes(x = 1e6*time, y = 1e3*sample.data, color = "blue"), size = 1) +
  geom_line(aes(x = 1e6*time, y = 1e3*psf.data, color = "red"), size = 1) +
  scale_x_continuous(breaks = pretty_breaks(n=3), limits = c(xmin,xmax)) +
  scale_y_continuous(limits = c(ymin,ymax)) +
  scale_color_manual(values = c("black", "blue", "red"), labels = c("bkg", "spl",
      "dif")) +
  guides(col = guide_legend(ncol = 1)) +
  labs(x = xlab, y = ylab)

data.set <- dat #%>% dplyr::filter(field.fitted < 0.95*max(field.fitted) &
    field.fitted > 0.95*min(field.fitted))
```

```
xlab = expression(paste(mu[0],"H [mT]"))
ylab = psf.label
xmin = min(data.set$field.fitted) - 0.1*max(data.set$field.fitted)
xmax = max(data.set$field.fitted) + 0.1*max(data.set$field.fitted)
ymin = 1e9*(min(data.set$psf.m3) - 0.1*max(data.set$psf.m3))
ymax = 1e9*(max(data.set$psf.m3) + 0.1*max(data.set$psf.m3))

p3 = ggplot(data.set) +
  geom_line(aes(x = field.fitted, y = 1e9*psf.m3, group = direction), size = 1) +
  # geom_point(aes(x = field.fitted, y = psf.m3, group = direction, color =
      direction), size = 3) +
  scale_x_continuous(breaks = pretty_breaks(n=3), limits = c(xmin,xmax)) +
  scale_y_continuous(breaks = pretty_breaks(n=3), limits = c(ymin,ymax)) +
  theme_new() +
  guides(col = guide_legend(ncol = 1)) +
  labs(x = xlab, y = ylab)


ylab = "Amp. [a.u.]"
ymin = min(data.set$psf.norm) - 0.1*max(data.set$psf.norm)
ymax = max(data.set$psf.norm) + 0.1*max(data.set$psf.norm)

p4 = ggplot(data.set) +
  geom_line(aes(x = field.fitted, y = psf.norm, group = direction), size = 1) +
  # geom_point(aes(x = field.fitted, y = psf.norm, group = direction, color =
      direction), size = 2) +
  scale_x_continuous(breaks = pretty_breaks(n=3), limits = c(xmin,xmax)) +
  scale_y_continuous(breaks = pretty_breaks(n=3), limits = c(ymin,ymax)) +
  theme_new() +
  guides(col = guide_legend(ncol = 1)) +
  labs(x = xlab, y = ylab)

ymin = min(data.set$mh.norm) - 0.1*max(data.set$mh.norm)
ymax = max(data.set$mh.norm) + 0.1*max(data.set$mh.norm)

p5 = ggplot(data.set) +
  geom_line(aes(x = field.fitted, y = mh.norm, group = direction), size = 1) +
  scale_x_continuous(breaks = pretty_breaks(n=3), limits = c(xmin,xmax)) +
  scale_y_continuous(breaks = pretty_breaks(n=3), limits = c(ymin,ymax)) +
  theme_new() +
  guides(col = guide_legend(ncol = 1)) +
  labs(x = xlab, y = ylab)

har.subset = seq(1, 37, 2)
```

```
data.set <- full %>% dplyr::filter(har %in% har.subset)

xlab = "Harmonic"
ylab = har.label
xmin = min(data.set$har) - 0.1*max(data.set$har)
xmax = max(data.set$har) + 0.1*max(data.set$har)
ymin = min(data.set$amp_mean) - 0.1*max(data.set$amp_mean)
ymax = max(data.set$amp_mean) + 0.1*max(data.set$amp_mean)

p6 = ggplot(data.set) +
  geom_point(aes(x = har, y = amp_mean), shape = 1, size = 3) +
  geom_errorbar(aes(x = har, ymin=amp_mean-amp_sd, ymax=amp_mean+amp_sd),
      width=.5, position=position_dodge(.9)) +
  scale_x_continuous(breaks = pretty_breaks(n=3), limits = c(xmin,xmax)) +
  scale_y_log10(labels = scales::trans_format("log10",
      scales::math_format(10^.x)), limits = c(ymin,ymax)) +
  annotation_logticks(sides = "l", size = 0.75) +
  theme_new() +
  guides(col = guide_legend(ncol = 3)) +
  labs(x = xlab, y = ylab)

# Set export directory whether or not saving images is selected
main.directory = getwd()
export.directory = "export"
dir.create(file.path(main.directory, export.directory), showWarnings = FALSE)
setwd(file.path(main.directory, export.directory))

if(export.data == "yes"){
  processed.data <- dat %>% select(field.fitted, psf.m3, psf.norm, mh.norm,
      direction, fwhm, fifthThird)
  write.csv(processed.data, "processed.csv", row.names = FALSE)
  processed.har <- full %>% select(har,amp_mean,amp_sd) %>% dplyr::filter(har
      %in% har.subset)
  write.csv(processed.har,"odd harmonics.csv", row.names = FALSE)
}

if(export.plots == "yes"){
  # ggsave("field-data.png", p1, width = 4.5, height = 4.5, dpi = "retina")
  # ggsave("raw-data.png", p2, width = 4.5, height = 4.5, dpi = "retina")
  ggsave("psf-m3.png", p3, width = 4.5, height = 4.5, dpi = "retina")
  ggsave("psf-norm.png", p4, width = 4.5, height = 4.5, dpi = "retina")
  ggsave("mh-norm.png", p5, width = 4.5, height = 4.5, dpi = "retina")
  ggsave("harmonics.png", p6, width = 4.5, height = 4.5, dpi = "retina")
```

```
}

if(export.grid == "yes"){
  combined <- ggarrange(p2, p3, p5, p6, hjust = -0.25,
                        labels = c("(a)", "(b)", "(c)", "(d)"), font.label =
                            list(size = 24),
                        ncol = 2, nrow = 2)
  ggsave("combined.png", combined, width = 9, height = 9, dpi = "retina")
}

if (display.psf == "yes"){
  p3
}

if (display.har == "yes"){
  p6
}
```

Appendix G

PYTHON SCRIPT FOR NEAREST NEIGHBOR DETERMINATION

```
#@ImagePlus imp
#@Integer(label="Number of Neighbors") k
#@Boolean(label="Give Each Neighbor's Distance") is_show_each

'''
Simple 2D KNN script
Olivier Burri, BioImaging & Optics Platform
Ecole Polytechnique  Fdrale  de Lausanne
July 12th 2016

Code provided as-is in reply to an ImageJ mailing list question
http://imagej.1557.x6.nabble.com/distance-between-adjacent-
particles-td3699485.html#a5016864
'''

from ij.gui import Overlay, Line, OvalRoi, Roi
from ij import IJ
from ij.measure import ResultsTable
from ij.measure import Calibration
from java.awt import Color
from ij.plugin.frame import RoiManager
import math

### Some functions ###

# Brute-Force KNN
def knn(data, k):
  # Just take the data, find the K nearest neighbors to each point

  the_knn=[]

  for i in range(len(data)):
    d = []
```

```
    for j in range(len(data)):
      d.append([j, dist(data[i], data[j])])

    # Sort
    d_sort = sorted(d, key=lambda thed: thed[1])
    # Keep only the k nearest
    the_knn.append(d_sort[1:(k+1)])
  return the_knn

# Euclidean Distance 2D
def dist(p0, p1):
    return math.sqrt((p0[0] - p1[0])**2 + (p0[1] - p1[1])**2)

# Convenience function to go from a ROI to points
def roiToPointList(roi):
  p = [roi.getFloatPolygon().xpoints, roi.getFloatPolygon().ypoints]
  points = map(list, zip(*p))
  return points

def showKNNResults(frt, the_knn, label):

  # Overlay
  ov = Overlay()
  the_avg = []

  # Draw each neighbor as a line and draw the average as a circle
  for i in range(len(the_knn)):
    avg = sum([d[1] for d in the_knn[i]]) / k
    the_avg.append(avg)

    o = OvalRoi(points[i][0] - avg, points[i][1] - avg, 2*avg, 2*avg)
    o.setStrokeColor(Color.decode("#00FFFF"))
    ov.add(o)

    for j in range(k):
      # XY Coordinates of current point
      a = points[i];
      b = points[the_knn[i][j][0]]
      # XY Coordinates of neighbor k
      l = Line(a[0], a[1], b[0], b[1])
      l.setStrokeColor(Color.decode("#FF00FF"))
      ov.add(l)
```

```
  # Build Results Table
  cal = imp.getCalibration()

  for i in range(len(the_knn)):
    frt.incrementCounter()
    frt.addValue("Label", label);
    frt.addValue("Point", i)
    frt.addValue("Average distance [px]", the_avg[i])
    if( cal.scaled() ):
      frt.addValue("Average distance ["+cal.getXUnit()+"]", cal.getX(the_avg[i]))
    if is_show_each:
      for j in range(k):
        if( cal.scaled() ):
          frt.addValue("Distance Neighbor "+str(j+1)+" ["+cal.getXUnit()+"]",
              cal.getX(the_knn[i][j][1]))
        else:
          frt.addValue("Distance Neighbor "+str(j+1)+" [px]", the_knn[i][j][1])

  frt.show(str(k)+" Nearest Neightbors Average Distances")
  imp.setOverlay(ov)



### Starting the script ###

# Get a new Results Table
rt = ResultsTable()

# Get the ROI manager
rm = RoiManager().getInstance2();

n_rois = rm.getCount();

# Work either on the image alone
if n_rois == 0:
  roi = imp.getRoi()
  label = imp.getTitle()
  # Get Coordinates
  points = roiToPointList(imp.getRoi())


  # Compute K Nearest Neighbors
  the_knn = knn(points,k)
```

```
  # Display the result table and an overlay
  showKNNResults(rt,the_knn,label)

# Or on each ROI of the ROI manager
else:
  for i in range(n_rois):
    roi = rm.getRoi(i)
    label = roi.getName()
    # Get Coordinates
    points = roiToPointList(roi)

    # Compute K Nearest Neighbors
    the_knn = knn(points,k)

    # Display the result table and an overlay
    showKNNResults(rt,the_knn,label)
```